GEOLOGY, GEOCHEMISTRY, HYDROTHERMAL ALTERATION, AND MINERALIZATION AT THE RONALDO EPITHERMAL PROSPECT, PERU

M.Sc. Thesis

Jaakko Georgi

September 2019

UNIVERSITY OF HELSINKI

FACULTY OF SCIENCE

DEPARTMENT OF GEOSCIENCES AND GEOGRAPHY

HELSINGIN YLIOPISTO
HELSINGFORS UNIVERSITET
UNIVERSITY OF HELSINKI

Tiedekunta/Osasto Fakultet/Sektion ï Faculty		Laitos/Institutionï Department
Faculty of Science		Department of Geosciences and Geography
Tekijä/Författare ï Author Jaakko Georgi		
Työn nimi / Arbetets titel ï Title Geology, geochemistry, hydrothermal alteration, and mineralization at the Ronaldo epithermal prospect, Peru		
Oppiaine /Läroämne ï Subject Geology (petrology and economic geology)		
Työn laji/Arbetets art ï Level M.Sc. thesis	**Aika/Datum ï Month and year** 09/2019	**Sivumäärä/ Sidoantal ï Number of pages** 132

Tiivistelmä/Referat – Abstract

This study consists of a comprehensive characterization of the geology, geochemistry, alteration, and mineralization at the Ronaldo prospect as well as an evaluation of its ore potential. Previous mapping campaigns of the prospect, which lies in the Central Andes in Peru at an elevation of 4300 metres, have identified intrusions overlain by a volcanic package. The intrusions are crosscut by silicified ridges that host epithermal mineralization. Satellite imagery reveals that the topographically elevated areas exhibit strongly altered rocks identified as an advanced argillic-altered lithocap. The methods used to define and better understand the geology and the evolution of the hydrothermal system included reconnaissance field mapping, whole-rock geochemistry, short-wave infrared spectroscopy, petrography, and geochronology. Previous studies have shown that only high-sulfidation epithermal mineralization can be spatially and temporally linked to porphyry Cu mineralization, and therefore this study investigates – among other aspects – what type of epithermal mineralization is present at Ronaldo in order to evaluate the potential for concealed at-depth porphyry Cu mineralization.

Two separate lower Miocene intrusive units were identified, a porphyritic diorite and a porphyritic granodiorite, whose average age difference is 1.79 Ma. The intrusive units display intermediate argillic alteration. The overlying extrusive units are Sacsaquero Formation basaltic andesites and ignimbrites that are either unaltered or display propylitic alteration. The basaltic andesite roof pendants observed at Ronaldo indicate that the tops of the intrusions are preserved.

At high elevations, advanced argillic alteration composed of pyrophyllite, kaolinite, and dumortierite was observed. This area is the remnant, deeper zone of a larger lithocap. The steeply dipping silicified ridges that display sericitic alteration were inferred to be the root zone of this lithocap. Elevated values of trace elements such as Te, Bi, As, and Sb suggest that the Ronaldo prospect is mostly situated in a sericitic alteration zone related to a porphyry-like magmatic-hydrothermal source located at greater depth. Isolated magnetite aggregates were observed in magmatic-hydrothermal breccia, which indicates that the sericitic alteration may have overprinted potassic alteration.

A few intermediate-sulfidation epithermal veins and porphyry-related veins, including a banded molybdenite quartz vein, were observed in the creek near the major fault. At Ronaldo, high silica content and sericitic alteration correlate well with elevated concentrations of Ag, Au, and Mo, whereas Cu concentration does not correlate well with any alteration type or with silica content. Quartz veinlets in the silicified ridges that host abundant Ag and Au mineralization were interpreted to have formed at a slightly later stage and to be unrelated to the magmatic-

hydrothermal system. This mineralization was interpreted to be low-sulfidation epithermal in origin due to features such as abundant adularia, lattice-textured bladed calcite replaced by quartz, crustiform banding, banded quartz-chalcedony veins, druse-lined cavities, and high Ag/Au ratios.

In conclusion, the Ronaldo prospect comprises a hydrothermal system in which the deep, root zone of an advanced argillic lithocap is exposed. The exploration potential for low-sulfidation epithermal mineralization in the silicified ridges is rather significant, whereas the potential for porphyry Cu mineralization is minor due to the lack of appreciable Cu and Mo mineralization, typically shallow-depth porphyry-related hydrothermal alteration, and the lack of high-sulfidation epithermal mineralization.

Avainsanat ï Nyckelord ï Keywords
Low-sulfidation epithermal mineralization, drusy quartz, adularia, silver sulfosalts, lattice-textured bladed calcite, advanced argillic lithocap root zone, silicified ridges, pyrophyllite, dumortierite, whole-rock geochemistry, short-wave infrared (SWIR) spectroscopy, porphyry Cu exploration, Miocene magmatism, the Andes, Huancavelica, Peru

Säilytyspaikka ï Förvaringställe ï Where deposited
Helsinki University Library

Muita tietoja ï Övriga uppgifter ï Additional information
The research presented in this thesis was done in collaboration with the University of Helsinki and First Quantum Minerals Ltd.

HELSINGIN YLIOPISTO
HELSINGFORS UNIVERSITET
UNIVERSITY OF HELSINKI

Tiedekunta/Osasto Fakultet/Sektion ï Faculty	**Laitos/Institutionï Department**
Matemaattis-luonnontieteellinen tiedekunta	Geotieteiden ja maantieteen laitos

Tekijä/Författare ï Author
Jaakko Georgi

Työn nimi / Arbetets titel ‑ Title
Epitermisen Ronaldo-esiintymän geologia, geokemia, hydroterminen muuttuminen ja mineralisaatio Perussa

Oppiaine /Läroämne ï Subject
Geologia (petrologia ja taloudellinen geologia)

Työn laji/Arbetets art ï Level	**Aika/Datum ï Month and year**	**Sivumäärä/ Sidoantal ï Number of pages**
Pro gradu	09/2019	132

Tiivistelmä/Referat – Abstract

Tämän tutkimuksen tavoitteena on karakterisoida Ronaldon malminetsintäalueen geologia, geokemia, hydroterminen muuttuminen ja mineralisaatio sekä arvioida alueen malmipotentiaali. Ronaldon malminetsintäalue sijaitsee Keski-Andeilla Perussa, 4300 metrin korkeudessa. Aikaisemmin alueella toteutetut kartoitusprojektit ovat havainneet alueelta intruusioita, joita peittävät vulkaaniset kivilajiyksiköt, sekä silisifioituneita harjanteita (silicified ridges), jotka leikkaavat edellä mainittuja intruusioita. Näistä silisifioituneista harjanteista löytyy epitermistä mineralisaatiota. Satelliittikuvien perusteella Ronaldon korkeimmista kohdista löytyy voimakkaasti muuttunutta kiveä, joka todettiin osaksi laajaa kehittyneen argillisen muuttumisen aluetta (advanced argillic lithocap). Tällainen alue muodostuu, kun happamat magmaattis-hydrotermiset fluidit reagoivat sivukiven kanssa. Tutkimuksen menetelmiin kuuluivat kokokivigeokemia, lyhyen aallonpituusalueen infrapunasäteily-spektroskopia (short-wave infrared spectroscopy), petrografia ja geokronologia. Aikaisemmat

tutkimukset ovat todenneet, että vain *high-sulfidation*-tyypin epitermiset malmit voivat spatiaalisesti ja ajallisesti liittyä porfyyrityypin mineralisaatioon. Näin ollen tässä tutkimuksessa perehdytään malminetsintäalueen muiden piirteiden ohella epitermisen malmin karakterisointiin, jotta malminetsintäalueen porfyyrityypin malmipotentiaali voidaan arvioida.

Alueelta kartoitettiin kaksi varhaismioseenin aikana muodostunutta intruusiota, porfyyrinen dioriitti ja porfyyrinen granodioriitti, joiden ikäero on keskiarvoltaan 1.79 miljoonaa vuotta. Nämä intrusiiviset kivilajiyksiköt ovat altistuneet intermediääriselle argilliselle muuttumiselle (intermediate argillic alteration). Intruusioita peittää Sacsaquero-muodostuman basalttiset andesiitit ja ignimbriitit. Alueella, jolla esiintyi lähinnä intrusiviisiä kiviä, havaittiin basalttisen andesiitin jäämiä (roof pendants), jotka indikoivat, että intruusioiden huiput ovat paljastuneina.

Ronaldon korkeimmissa kohdissa havaittiin muuttumismineraaleja, kuten pyrofylliittiä, kaoliniittia sekä dumortieriittiä, jotka kaikki viittaavat kehittyneeseen argilliseen muuttumiseen. Alue tulkittiin lithocapin syvien osien jäämiksi. Serisiittiselle muuttumiselle (sericitic alteration) altistuneet silisifioituneet harjanteet tulkittiin tämän lithocapin juurirakenteiksi. Kokokivigeokemiaan perustuen alueen on tulkittu olevan pääosin osa serisiittistä muuttumisvyöhykettä, sillä etenkin Te-, Bi-, As- ja Sb-pitoisuudet ovat koholla. Magmaattis-hydrotermisessä breksiassa havaitut suuret magnetiittirakeet (magnetite aggregates) mahdollisesti indikoivat, että aiempi kali-muuttuminen (potassic alteration) on korvautunut serisiittisellä muuttumisella.

Malminetsintäaluetta leikkaa jokilaakso, josta havaittiin muutamia *intermediate-sulfidation*-tyypin epitermisiä juonia sekä muutamia porfyyrityypin juonia. Korkea silikapitoisuus sekä serisiittinen muuttuminen korreloivat korkeiden Ag-, Au- ja Mo-pitoisuuksien kanssa Ronaldossa, kun taas Cu-pitoisuus ei korreloi silikapitoisuuden tai minkään muuttumistyypin kanssa. Silisifioituneissa harjanteissa havaittiin kvartsijuonia, joiden tulkittiin muodostuneen myöhemmässä, magmaattis-hydrotermiseen systeemiin liittymättömässä vaiheessa. Juonissa esiintyy ajoittain runsasta hopea- ja kultamineralisaatiota, joka karakterisoitiin *low-sulfidation*-tyypin epitermiseksi mineralisaatioksi useiden teksturaalisten havaintojen, korkean Ag/Au-suhdeluvun sekä ohuthiessä havaitun adularian perusteella.

Ronaldon malminetsintäaluetta karakterisoi laaja hydroterminen systeemi, josta lithocapin syvät juurirakenteet ovat paljastuneina. *Low-sulfidation*-tyypin epitermisen mineralisaation malminetsintäpotentiaali on alueella huomattava, kun taas porfyyrityypin mineralisaation malminetsintäpotentiaali alueella ei ole lupaava. Tätä puoltavat alhaiset Cu- ja Mo-pitoisuudet, harvakseltaan havaitut porfyyrityypin juonet, tyypillisesti matalan hydrotermisen muuttumisvyöhykkeen muuttumismineraalit sekä *high-sulfidation*-tyypin epitermisen mineralisaation puute.

Avainsanat ï Nyckelord ï Keywords
Low-sulfidation-tyypin epiterminen mineralisaatio, adularia, kehittynyt argillinen muuttuminen, lithocap, silisifioituneet harjanteet, pyrofylliitti, dumortieriitti, kokokivigeokemia, lyhyen aallonpituusalueen infrapunasäteily-spektroskopia, porfyyrityypin malmipotentiaali, Andit, Huancavelica, Peru

Säilytyspaikka ï Förvaringställe ï Where deposited
Helsingin yliopiston kirjasto

Muita tietoja ï Övriga uppgifter ï Additional information
Tämä työ on toteutettu yhteistyössä Helsingin yliopiston ja yhtiön First Quantum Minerals Ltd. kanssa.

TABLE OF CONTENTS

1. INTRODUCTION

1.1. Porphyry copper systems

Deposits related to porphyry Cu systems host an array of globally significant precious and base metals (Seedorf 2005), including three quarters of the global supply of Cu, half of Mo, one fifth of Au, most of Re, and minor amounts of other metals (Ag, Pd, Te, Se, Bi, Zn, and Pb) (Sillitoe 2010). Porphyry Cu systems form mostly in subduction zones, at convergent plate boundaries associated with calc-alkaline and sometimes alkaline magmatism (Figure 1) (Sillitoe 1972).

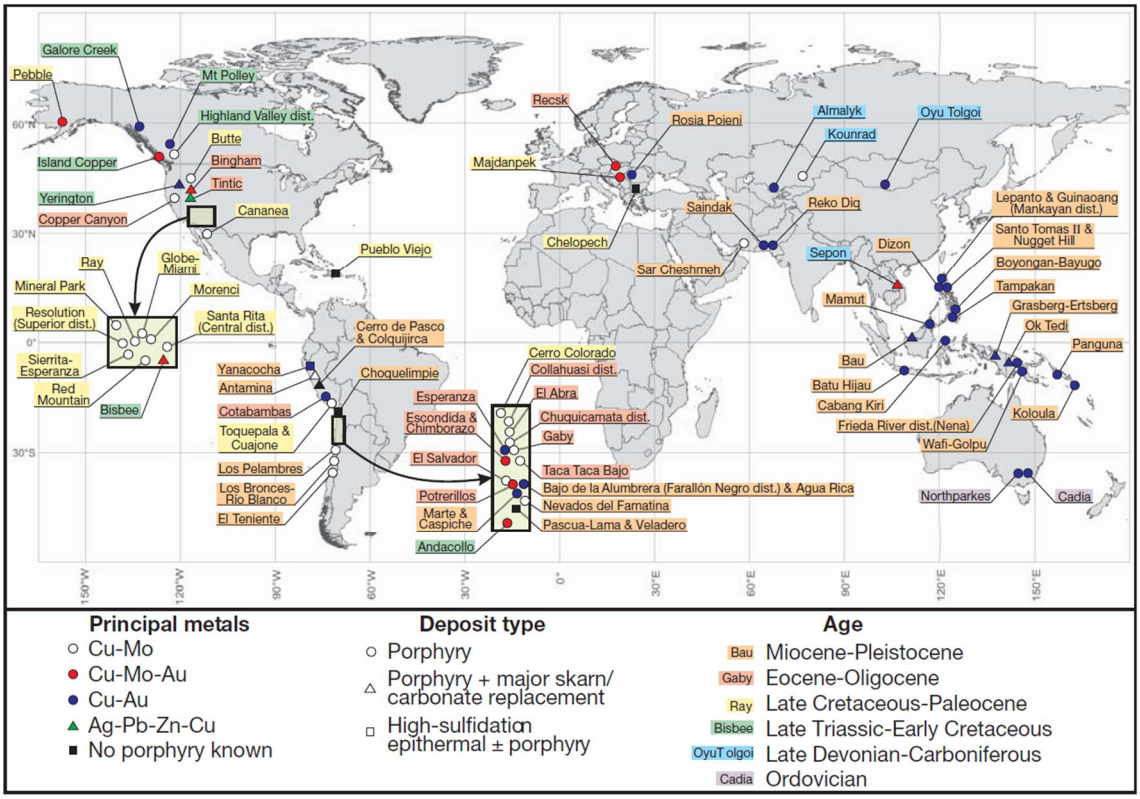

Figure 1: Worldwide locations of significant porphyry Cu systems, after (Sillitoe 2010).

Porphyry Cu systems are defined as large volumes of hydrothermally altered rock that are centred on a porphyritic stock or a group of dikes that are typically intermediate in

composition (Sillitoe 2010). Such systems may contain porphyry Cu±Mo±Au mineralization and associated high- to intermediate-sulfidation epithermal precious and base metal mineralization (Figure 2) (Sillitoe 2010). Other base and precious metal mineralization types such as skarn, carbonate-replacement, and sediment hosted are also associated with porphyry Cu systems. The term “porphyry Cu system" is used in this article to describe broad hydrothermal systems containing porphyry Cu and epithermal-style mineralization.

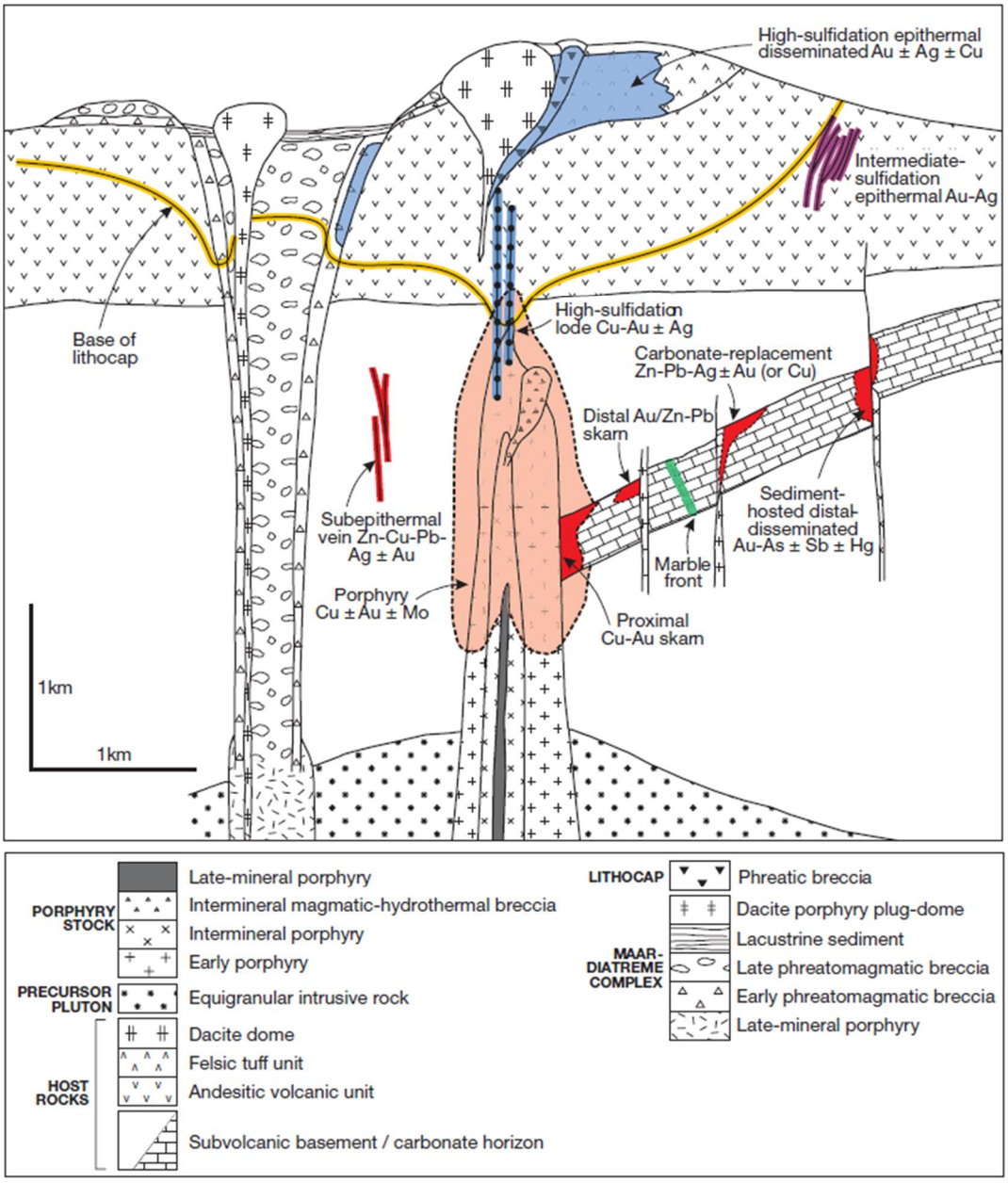

Figure 2: Schematic porphyry Cu system and related hydrothermal deposit model, after Sillitoe 2010.

A porphyry Cu system is formed when a hydrous magma crystallizes in the shallow crust and exolves an acidic magmatic-hydrothermal fluid. This fluid may accumulate in cupolas on top of the intrusion, and when the pressure of the fluids surpasses the lithostatic load, the fluid may be released through hydrofracturing of the roof-wall rock of the intrusion. Small volumes of magma are also released at this stage and result in the emplacement of porphyritic stocks or dike swarms, which act as conduits for the magmatic fluids exolving from the parental magma chamber. The acidic nature of the magmatic hydrothermal fluid and its relatively high temperature results in widespread metasomatism of the wall rock. The fluid may split into two phases depending on the depth of emplacement: small volumes of saline brines and large volumes of vapour (Henley et al. 1978). The brine is thought to produce porphyry Cu mineralization around the apex of the intrusive porphyry stock whereas the ascending vapor can produce extensive, broadly strata-bound subsurface alteration domains called lithocaps (Cooke et al. 2017). Lithocaps are lithologically controlled zones of pervasive advanced argillic alteration, and they are typically much more extensive than their underlying porphyry copper deposits (PCD), and they can host high-sulfidation Cu-Au mineralization (Sillitoe 2010).

Porphyry Cu mineralization occurs around intrusive porphyry stocks and dikes, which originate from underlying multiphase batholiths emplaced in the shallow crust (Sillitoe 2010). The mineralization is formed above and around the porphyry stocks by magmatic-hydrothermal aqueous solutions that precipitate sulfide and oxide ore minerals at elevated temperatures (>700 to >350 °C) (Seedorf 2005).

In contrast, epithermal deposits form at shallow levels in the crust (<1km) due to shallow level activity of magma-related hydrothermal systems, which commonly form in subaerial volcanic arcs (Simmons et al. 2005). Epidermal deposits are an important source of gold and silver but also host Pb, Zn, Hg, and Sb (Hedenquist et al. 2000). Epithermal deposits can be divided into three main deposit types: high, intermediate and low sulfidation. High- and low-sulfidation deposits can be distinguished due to the presence of diagnostic minerals and textures as well as the degree of sulfidation and oxidation (Simmons et al. 2005). These features vary according to the composition and the degree of mixing of the related fluids (Hedenquist et al. 2000).

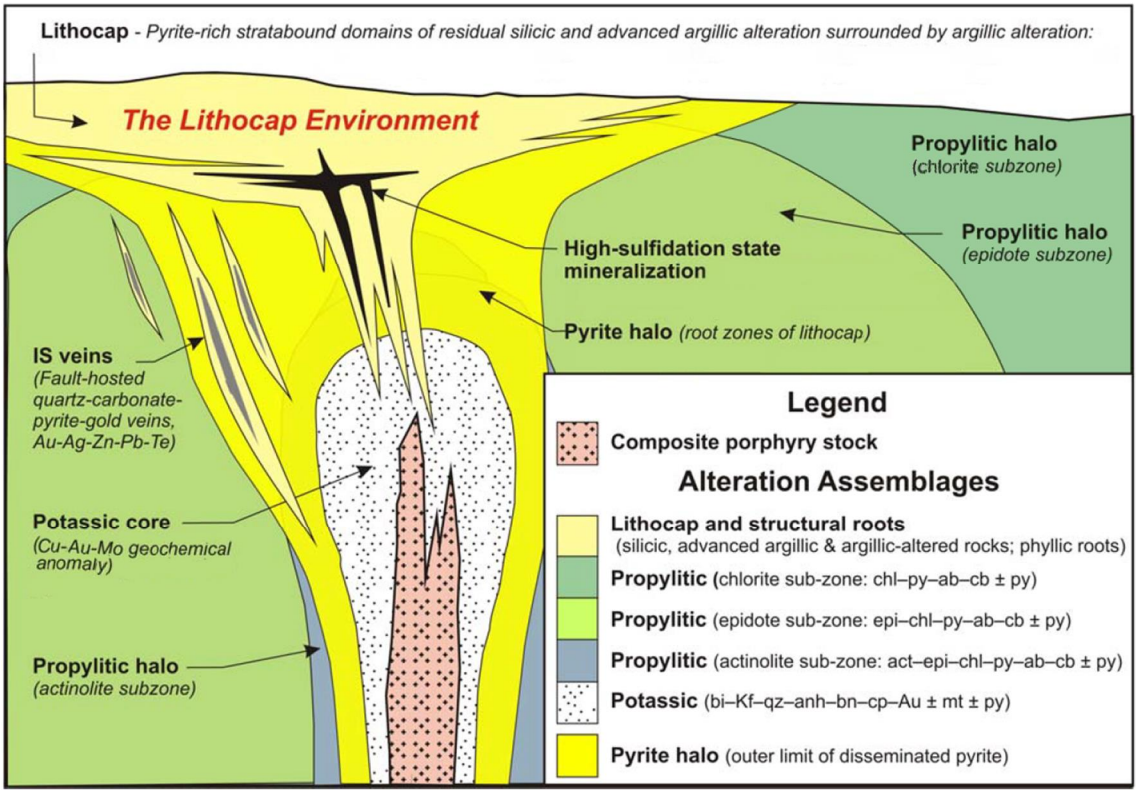

Figure 3: Schematic illustration of lithocap-related alteration and overprinting relationships in a porphyry Cu system, after Holliday et al. 2007.

High- and intermediate-sulfidation epithermal deposits form at shallow depths in porphyry Cu systems, at temperatures ranging from <150°C to ~300°C (White et al. 1995). Typically, high-sulfidation epithermal deposits (Au±Ag±Cu) form in the lithocap environment at shallower levels above or at the near periphery of porphyry Cu systems, whereas intermediate-sulfidation epithermal deposits (Zn-Pb-Ag±Cu±Au) typically occur alongside lithocaps (Figure 3) (Sillitoe 2010). Intermediate-sulfidation epithermal deposits typically occur separate from high-sulfidation orebodies (Sillitoe 2010) but may be considered to be potentially transitional due to evidence of a spatial and possibly even genetic relationship between the two deposit types (Sillitoe 2000; Hedenquist et al. 2000; Einaudi et al. 2003).

Low-sulfidation epithermal deposits differ substantially from the aforementioned epithermal deposit types in that the hydrothermal fluids are dominantly meteoric water, in contrast to the magmatic-hydrothermal derived fluid in the high- and intermediate-sulfidation environment (White et al. 1995). No clear genetic link has been established

between low-sulfidation epithermal deposits and PCDs, although heat from the emplaced intrusive body can surely contribute to the endowment of metals in fluids and the circulation of meteoric water.

PCDs centred on intrusions and suprajacent high- and intermediate-sulfidation epithermal mineralization are all formed in porphyry Cu systems and have been shown to exhibit close genetic relationships in numerous ore districts, including Lepanto Far South East, Chuquicamata, Agua Rica and others (Arribas et al. 1995; Hedenquist et al. 1998; Ossandón et al. 2001; Heinrich 2005; Cooke et al. 2011; Franchini et al. 2011). Even if a clear genetic relationship between a porphyry Cu mineralization and a high- or intermediate-sulfidation epithermal mineralization were apparent, detailed investigation of the evolution of the hydrothermal system would be required to understand the relationship because the transition from porphyry to epithermal environments is often complicated (Muntean et al. 2001; Sillitoe et al. 2003).

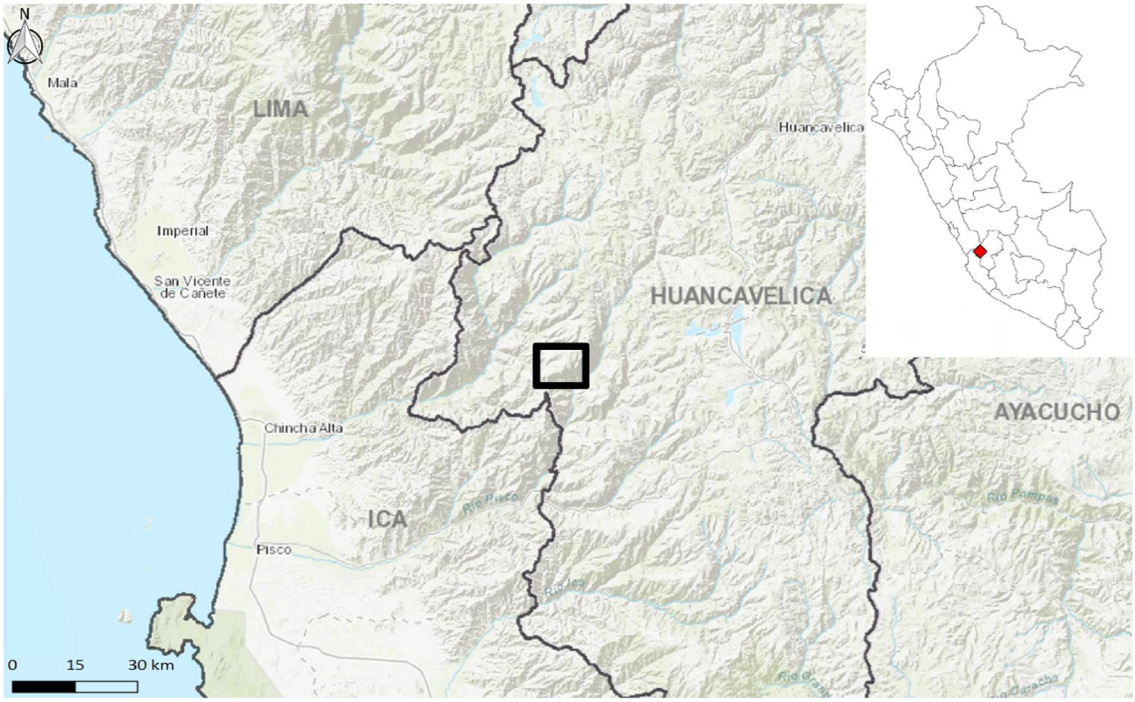

Figure 4: The Ronaldo prospect is situated 210 km southeast of Lima, in the Department of Huancavelica in Peru. It is situated in the Western Cordillera of the Andes, at roughly 4300 metres. Modification of map provided by Ingemmet.

1.2. Study area and the aims of the study

The study area of this paper is located in the Department of Huancavelica, in central Peru (Figure 4), at an elevation of 4300 metres above sea level. The Panteria project was first discovered and staked by Peruvian Metals (formerly Duran Ventures) in 2007 (Peruvian Metals…2018), which entered into an option agreement in 2016 with Minera Antares Peru SAC, a wholly owned subsidiary of TSX-listed First Quantum Minerals Ltd. (FQM). The Panteria project is divided into two distinct target areas called the Panteria and Ronaldo zones. The aim of FQM is to explore the PCD potential at Panteria and evaluate probability of the existence of a concealed at-depth PCD at Ronaldo.

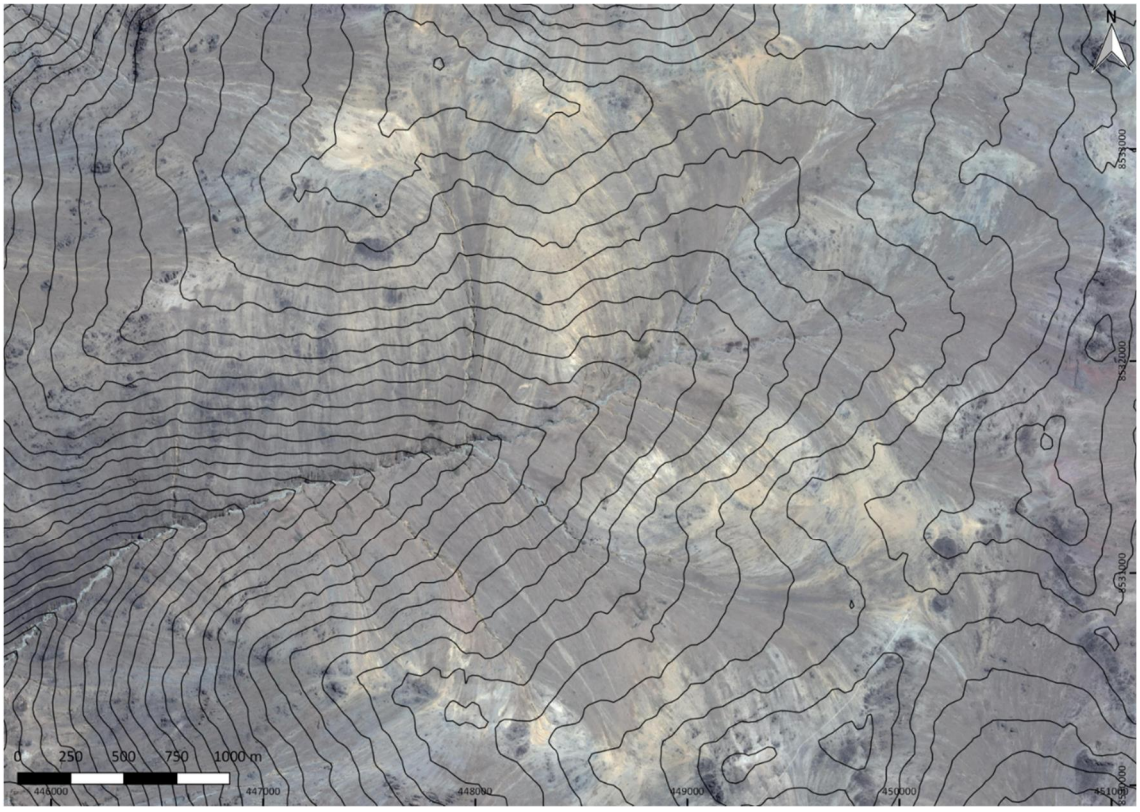

Figure 5: Satellite image of the Ronaldo prospect clearly showing the intensely hydrothermally altered rock at high elevations as yellow-brown colour anomalies, with the ENE-WSW-oriented creek running through the area. The contour lines are spaced at 25 metres.

This study is centred on Ronaldo, which comprises advanced argillic- and intermediate argillic-altered intrusive rocks interpreted to be part of a high-sulfidation epithermal

mineralization bearing lithocap hosted in gently dipping volcanic rocks. Previous mapping and sampling at Ronaldo identified Au- and Ag-bearing veins in silicified ridges and breccias that are related to and sometimes crosscut the advanced argillic alteration. An ENE-WSW-oriented creek, which reveals deeper parts of the system, cuts through the Ronaldo zone. The creek is surrounded by two topographically elevated hills, which exhibit evident altered rock, as observed in satellite imagery (Figure 5).

The aims of this study are to characterize the geology in addition to understand and define the hydrothermal system responsible for the formation of the lithocap and related Au and Ag mineralization at Ronaldo, while also investigating the possible existence of an underlying, concealed at-depth PCD.

The Au and Ag mineralization at Ronaldo is found in silicified ridges which are possibly part of the deep root zone of a lithocap, which are commonly at least partly structurally controlled (Sillitoe 2010). Geochemical assays and thin sections were prepared from the silicified ridges to determine the type of epithermal mineralization present. Each type of epithermal mineralization has distinct characteristics, which were searched for in analyses and in the thin sections. As previously stated, only high-sulfidation epithermal mineralization has previously been proven to be spatially and temporally linked to porphyry Cu mineralization, and therefore investigating the type of epithermal mineralization present is central to this study to enable evaluation of concealed at-depth PCD potential. Determination of the hydrothermal alteration type present at Ronaldo is crucial for understanding the hydrothermal system, and therefore rock samples were collected for short-wave infrared (SWIR) spectroscopy analyses. To further investigate the possible existence of a concealed at-depth PCD, whole-rock geochemical assays were paired with SWIR analyses of rock samples. The combination of these two methods provides information on the depth of the hydrothermal system, which is crucial for efficient exploration of concealed at-depth PCDs.

Based on previous mapping campaigns, it is evident that an intrusive unit occupies parts of Ronaldo. Whole-rock geochemical analyses and geochronological analyses were carried out in order to understand the nature of the intrusive unit. Whole-rock geochemical analysis results and thin sections were used to identify if all intrusive rocks belong to the same lithological unit.

2. REGIONAL TECTONIC AND GEOLOGIC SETTING

The best-known example of a mountain chain formed during subduction of an oceanic slab under a continental plate are the Andes. The present-day mountain chain is largely the result of an orogenic process that started in the late Oligocene, when large-scale reorganizing of oceanic plates in the eastern Pacific occurred (Tebbens et al. 1997), causing intense tectonic uplifting in the continental plate due to intense subduction activity of the oceanic Nazca Plate. The ongoing processes of subduction and magma generation have uplifted rocks above the collision zone since the late Oligocene.

PCD formation is closely linked with these processes since the subduction of an oceanic plate along a convergent zone creates potentially fluid-rich and oxidized magmas below the continental plate. These hydrous magmas are essential to the formation of PCDs deposits. Under these favourable conditions, the sulfide deposition in the ascending magma is inhibited, enabling the availability of metals for later partitioning into magmatic fluids. Upon release, these fluids may later deposit the metals in the upper crust, thus forming PCDs (Gustafson et al. 1975). This is the reason why PCDs are commonly associated – as exemplified in the Andes – with extensive mountain ranges related to subduction or paleo subduction zones. A simple progressive subduction system does not correspond with the spatial and temporal distribution of PCDs in the Andes: instead, a unique combination of geologic factors resulted in pulses of intense metallogenic activity, which formed ore deposits that are concentrated in distinct bands parallel to the orogeny (Stern 2004).

The subduction geometry of the Nazca Plate beneath the Andes is a direct product of the along-strike variation in the dip of the subducting Nazca Plate. The volcanoes of the cordillera reveal crucial information about tectonic, magmatic, and ore-forming processes and the angle of subduction, all of which greatly impact the probability of economic PCD formation. The Andes encompass four zones of active volcanoes, where the angle of subduction is relatively steep (>25˚), which alternate with four flat-slab segments with shallow subduction angles of 10˚ at depths greater than 100 km. The decrease in subduction angle in these flat-slab segments may be caused by a variety of buoyant topographic features in the subducting oceanic slab such as aseismic ridges,

seamount chains, and oceanic plateaus (Stern 2004; Sillitoe 2005). The suppression of volcanism and crustal thickening that occur in the very compressional flat-slab segments may lead to magma being trapped in large, shallow magma chambers and to the accumulation of metals and volatiles due to the inhibition of volcanism. As a result of these processes, economic PCDs may form (Sillitoe 2005).

The Peruvian volcanic gap extends from 2˚ S to 15˚ S, under which the Peruvian flat-slab zone extends. This exceptionally large flat-slab subduction zone formed due to the presence of both the Nazca Ridge and the completely subducted Inca Plateau (Gutscher et al. 1999). Several smaller porphyry and epithermal deposits are spatially and temporally associated with the currently subducting Nazca Ridge in the Peruvian flat-slab zone, although no giant deposits have been found to this day (Cooke et al. 2005).

The Central Andes (15°-34°S) are – as the name implies – the central part and a continental-scale segment of the Andean convergent system. The Central Andes can be further divided – based on subduction conditions, tectonic style, volcanism, and along-strike variations of topography – into three second-order segments: Altiplano (15°-23°S), Puna (23°-28°S), and the Frontal Cordillera (28°-34°S) (Tassara 2005). The Ronaldo prospect is situated near the Altiplano boundary at 13°S, 75°W. Thus, the study area is not situated in the Central Andes but lies in very close proximity to the segment and will therefore be henceforth treated as belonging to the Central Andes.

During the late Eocene-Oligocene, abundant effusive magmatic activity bore the thick volcanic-sedimentary sequences of the Tantará and the Sacsaquero Formation, which are widely spread out in the Western Cordillera (Salazar Díaz et al. 1983; Instituto Geológico…2003). These volcanic-sedimentary sequences lie in discordance over the Coastal Batholith and older Mesozoic rock units (Figure 6).

The Ronaldo prospect lies within a thick volcanic-sedimentary sequence called the Sacsaquero Formation. The formation is characterized by porphyritic andesite lava flows, welded ignimbrites, redeposited tuffs and breccias, as well as sedimentary rocks. The Sacsaquero Formation lies in discordance over the Tantará Formation, and the Castrovirreyna Formation in turn lies in discordance over the Sacsaquero Formation. Both the Tantará and the Castrovirreyna Formations are distinct volcanic-sedimentary

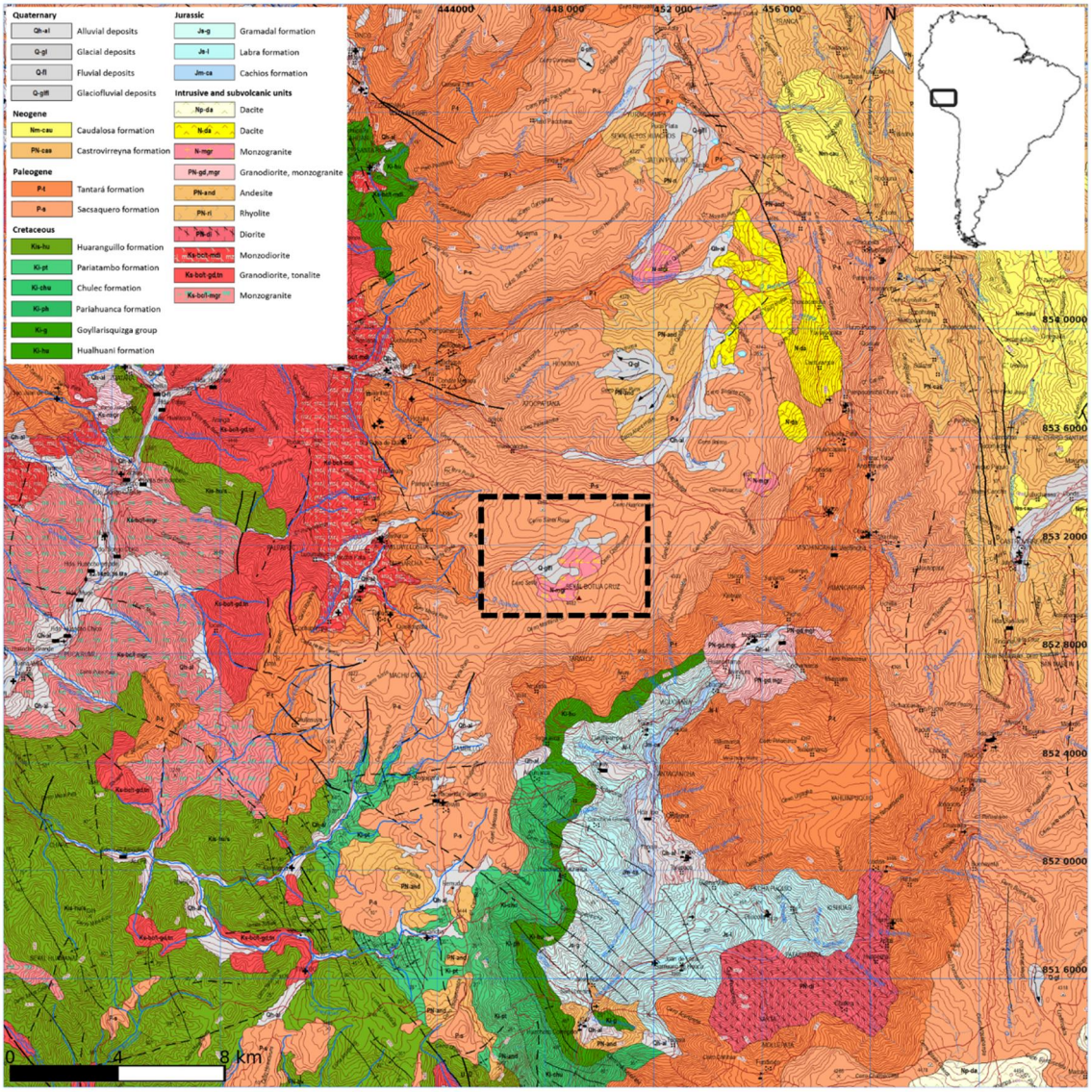

Figure 6: Map of the regional geology of the Ronaldo prospect, which is centred around the monzogranite intrusion, overlain by glaciofluvial quaternary deposits, located in the centre of the map. Map compiled from geological maps obtained from Ingemmet.

sequences. The Tantará Formation – which underlies the Sacsaquero Formation – is dated to be late Eocene (Salazar Díaz and Landa Tovar 1983; Instituto Geológico…2003), as is the Sacsaquero Formation.

The overlying volcanic-sedimentary sequences are intruded by intrusive bodies of different compositions and ages, some related to the Coastal Batholith (Mesozoic) and other younger intrusions (Paleogene and Neogene) (Salazar Díaz and Landa Tovar 1983; Instituto Geológico…2003). The Ronaldo prospect is characterized by Sacsaquero volcanic sequences intruded by lower Miocene intrusions unrelated to the Coastal

Batholith. Both the intrusive and extrusive sequences are overlain by glaciofluvial quaternary deposits (Figure 6). The lower Miocene intrusive units were formed as a direct result of the orogenic process that started in the late Oligocene. There are two intrusive units of similar age, composition, and size (on the surface) less than 10 km away from Ronaldo (Figure 6), which suggests that there was small scale active magmatism in the area during the time when the intrusive bodies at Ronaldo were formed. This magmatic activity may have been enabled by either weak extensive regimes or flat-slab subduction similar to the current geological activity. In the circum-Pacific region, PCD formation during the last 20 Ma has been closely related to subducting aseismic ridges and seamount chains as well as to oceanic plateaus beneath continental arcs (Cooke et al. 2005). Therefore, it is likely that a flat-slab regime is related to the early Miocene magmatism at Ronaldo.

3. MATERIALS AND METHODS

3.1. Field mapping

Reconnaissance geologic mapping was conducted during which traditional outcrop mapping, vein mapping, and structural observations were made. While mapping the outcrops, the lithology, alteration, and veins were closely studied; and in the veins, possible base and precious metal mineralization and alteration selvages were observed. Anaconda-style mapping at a 1/1000 scale was carried out simultaneously. The Anaconda mapping method is a specific mapping method used to map alteration and mineralization in magmatic-hydrothermal ore systems. It was developed from mapping schemes devised during the 1960s by Anaconda geologists at El Salvador, Chile, and Yerington, Nevada (Einaudi 1997). Anaconda maps are composed during field work and are colour-coded quantitative representations of field observations (lithology, veins, vein selvages, alteration, and structural measurements). The style of mapping is used to

complement quantitative analysis methods used in exploration for PCDs and other ore types, and it was therefore considered an acceptable system for mapping Ronaldo.

3.2. Petrography

Vein samples were collected, of which 18 standard 27x46 mm rectangular polished thin sections of mineralized and unmineralized veins were selected for detailed ore mineralogy study. The polished thin sections were prepared by Spectrum Petrographics, Inc. 20 standard 27x46 mm rectangular unpolished thin sections of the main lithological units were prepared by Van Petro (Vancouver Petrographics Ltd.). The most representative thin sections were later polished at the Department of Geosciences and Geography of the University of Helsinki to obtain higher quality microphotographs. Standard transmitted and reflected light microscopy in addition to petrographic techniques were used to describe the textures and mineralogy of the rocks and veins.

3.3. Lithogeochemistry

A total of 47 samples were subjected to a four-acid leach and analysed by ALS Geochemistry in Lima, Peru, for whole-rock geochemistry in addition to precious and base metals. Major and minor elements, Ag, Pb, and Zn were analysed using inductively coupled plasma-atomic emission spectroscopy (ICP-AES), while 48 trace elements, 12 rare earth elements, and Hg were analysed by inductively coupled plasma-mass spectroscopy (ICP-MS). Gold (Au) was analysed by fire assay. The codes for the analytical methods used by the ALS laboratory to obtain whole-rock geochemical assay results were ME-MS61r, ME-4ACD8, ME-ICP06, and ME-MS42. See the Appendices for additional analytical details.

Of the 47 samples only the least altered ones were selected for lithogeochemical characterization. Samples subjected to hydrothermal alteration and consequent alkali changes were screened out using diagrams including Na/Al and K/Al and plotting

elements against immobile elements such as Sc, Ti, and V (Figure 11 and Figure 12). Major element oxides were normalized to 100% volatile-free, as presented in Table 1.

Whole-rock geochemical assay results were used to construct a model of geochemical dispersion and alteration around PCDs (Halley et al. 2015) to infer the location and zonation of possibly concealed at-depth PCDs. The model is based on the tendency of metals to be zoned in PCDs in regard to the heat source, fluid flow, and cooling or neutralization of the acidic fluid. The combination of whole-rock geochemical analysis with SWIR analysis is considered a rapid and cost-effective method for studying the hydrothermal mineralogy in PCDs. Zoning of trace metal enrichment and depletion has been found to be relatively consistent in a number of well-known PCDs (Halley et al. 2015). Trace metals zone upward from the Cu zone in the general sequence of Mo, W, Sn, Se, Te, Bi, Sb, As, Li, and Tl (Halley et al. 2015). The metal sequences beyond the Cu zone closely mimic the general decrease in solubility of metals in chloride in cooling hydrothermal fluids (Reed et al. 1984).

3.4. Spectral mineral analysis

Short-wave infrared (SWIR) spectroscopy analysis was used to identify hydrous minerals, each of which display distinctive spectra (Thompson 1999). A total of 102 rock samples with representative and preferably abundant hydrous alteration minerals were selected as the sample medium for the SWIR analyses. Samples were processed by ALS Geochemistry in Lima, Peru, using the ALS Geochemistry method TRSPEC-20, which includes crushing the sample and then subjecting it to a spectral scan using a TerraSpec® 4 HR spectrometer. Reflected infrared radiation was measured between 1400 and 2390 nm. The spectral results were processed using The Spectral Geologist™ software, which was used to identify the wavelength of each characteristic absorption feature. The obtained characteristic absorption features were then compared with reference standards (Thompson 1999; Goetz 2009). Hydrous minerals were identified that are well characterized using SWIR analysis and that are common in PCDs. Hydrous minerals identifiable by SWIR analysis that are central to this study include muscovite, muscovite-

illite, kaolinite, smectite, pyrophyllite, tourmaline, and chlorite. Henceforth, sericite and muscovite will be considered interchangeable terms.

3.5. Geochronology

Geochronology samples were collected from the main intrusive bodies for U-Pb in zircon age dating. The U-Pb in zircon samples were analysed by a commercial service at the Geological Institute of the Bulgarian Academy of Sciences in Sofia, Bulgaria. The samples were prepared using a jaw crusher (Sturtevant) (crushing to <0.3-0.5 cm) and disc mill (<0.6-1 mm) with a vertical door. The machines were opened and cleaned with an air blast and then methanol/acetone and a kimwipe after each sample. The whole sample of size fraction <0.6-1 mm was washed using a Wilfley table and separated into heavy and light fractions and then dried. The heavy fraction was sieved, and a magnetic separator was used to separate the non- to slightly magnetic fraction. The zircon concentrate was collected using heavy liquids (2.9 g/cm^3 bromoform and 3.32 g/cm^3 methylene iodide). The zircons were picked manually under a binocular microscope. For preparation of the mounts for analysis, 20 to 40 zircon grains were embedded in epoxy resin and polished to the middle of crystals. Then they were imaged using a microscope. LA-ICP-MS U-Th-Pb isotope zircon analysis was carried out using a New Wave Research (NWR) 193 nm excimer laser UP-193FX attached to a Perkin-Elmer ELAN DRC-e quadrupole inductively coupled plasma mass spectrometer (LA-ICP-MS). An in-laboratory designed ablation cell with lowered position effects, a “squid” smoothing device, an energy density per sample of ca. 7-7.2 J/cm^{-2}, and a repetition rate of 8 Hz were used. The ablation craters were 35 and 25 μm. The analyses were carried out in blocks of 22, using the GJ-1 zircon standard (Jackson et al. 2004) for fractionation corrections (2 analyses at the beginning, 2 in the middle, and 2 at the end of the block) and Plesovice (Sláma et al. 2008) to look for systematic errors (secondary SRM for internal control). The results were calculated off-line using Iolite software. For each sample, all concordant zircons were used to calculate a concordia age, or a mean $^{238}U/^{206}Pb$ age, and a probability density plot. The plots were processed using ISOPLOT 4.15.

4. RESULTS

4.1. Lithological units

The different lithological units described in the field, namely the basaltic andesite, porphyritic diorite, porphyritic granodiorite, and silicified ridges (Figure 17, Figure 19, Figure 21, Figure 23, and Figure 24) have well defined whole-rock compositional differences as well as petrographical characteristics (Figure 11 and Figure 14). A summary of the results, including whole-rock geochemical codes and thin section codes, is presented in Table 5. Lithological units such as ignimbrites and magmatic-hydrothermal breccias were not sampled for whole-rock geochemical analysis and were solely described based on field observations. Based on the findings, a lithological map of the prospect was composed (Figure 28). Additional data used to compose the map consisted of magnetic susceptibility data, IP data, and K-U-Th data provided by FQM.

Figure 7: Details of the Anaconda-style alteration map composed during field mapping. The complete map including the legend is provided in the Appendix (Figure 50).

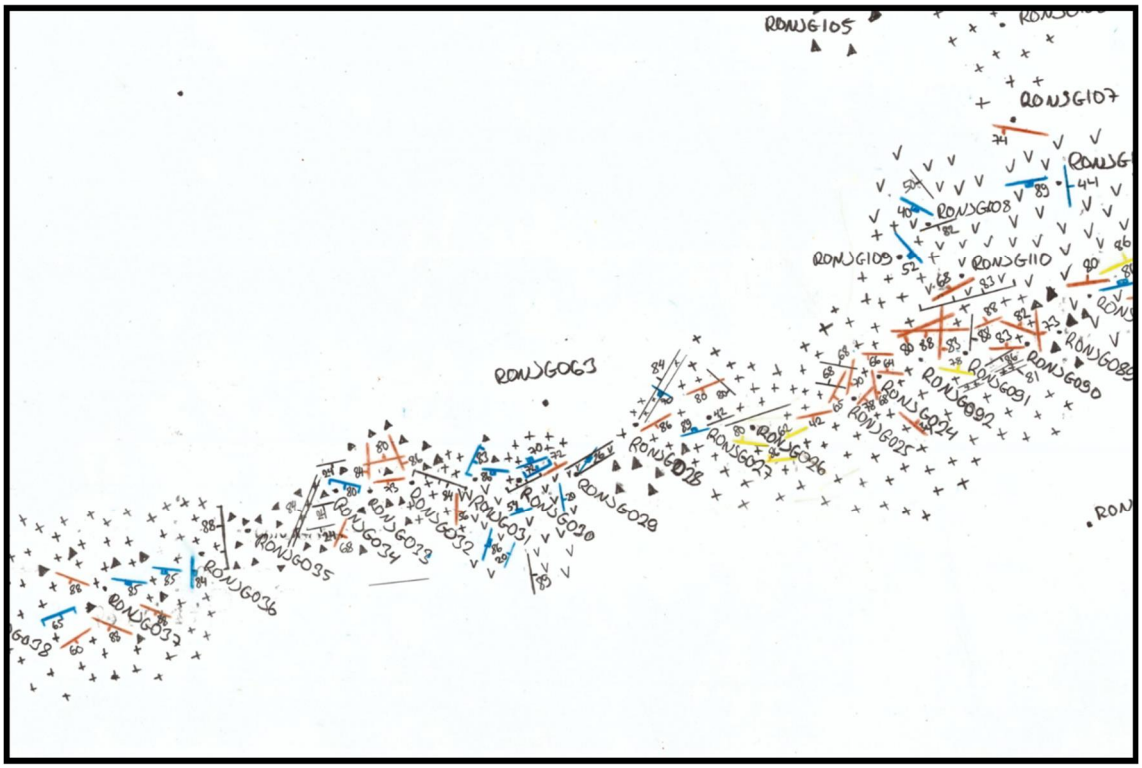

Figure 8: Details of the Anaconda-style lithology, structures and veins map composed during field mapping. The complete map including the legend is provided in the Appendix (Figure 51).

Figure 9: Details of the Anaconda-style mineralization map composed during field mapping. The complete map including the legend is provided in the Appendix (Figure 52).

Field observations

Field observations were made between the elevations of 3960 m and 4518 m. In addition to traditional geological mapping, detailed Anaconda style mapping was conducted. Details of the Anaconda style mapping are presented in Figure 7, Figure 8, and Figure 9, and the scanned, complete three layers of the map are presented in the Appendices (Figure 50, Figure 51, and Figure 52).

The lower parts of the prospect are dominated by intrusive rocks, such as porphyritic diorite and porphyritic granodiorite. Intrusive rocks and aplitic dikes were observed from 3960 m to 4472 m. The intrusive porphyritic diorite, porphyritic granodiorite, and aplitic dikes intrude the overlying gently dipping volcanic units, such as porphyritic basaltic andesites and equigranular basaltic andesites. Aplitic dikes – which most likely originate from the porphyritic granodiorite intrusion – crosscut the extrusive wall rock, which could be observed at high elevations in the prospect (up to 4475 m).

Extrusive rocks were observed from 4114 m to 4518 m. Although the intrusive units are overlain by volcanic units, this does not mean that the volcanic units are younger. In fact, the volcanic units are older of age, and the intrusive bodies have merely failed to intrude the entire volcanic sequence, a feature that could be especially well observed at high elevations at Ronaldo. Basaltic andesite roof pendants were observed throughout the elevated parts of the prospect. This suggests that the intrusions currently observed at Ronaldo are the topmost parts of the intrusions. Ignimbrite with characteristic welded fiamme and lithic clasts overlie the basaltic andesite. Hornfelsed rocks were encountered in the NE parts of the creek and at the contact of the porphyritic diorite and the magmatic-hydrothermal breccia. The hornfelsing of rocks is evidence of contact metamorphism in the host rock caused by heat expulsion from the intrusive bodies.

The dominant geologic features at the Ronaldo prospect are advanced argillic- and intermediate argillic-altered intrusive units. This altered zone, which mostly consists of porphyritic diorite, can be well observed from satellite images as a large yellow-brown colour anomaly extending over the elevated areas of the prospect (Figure 5). Apart from this, intrusive rocks displaying propylitic alteration are abundant throughout the prospect and can be found both in the creek and in distal parts of the system. The grain

size of this porphyritic intrusive rock seems to decrease with increasing elevation, which is especially evident on the southern hill of the prospect. This is most likely the result of faster cooling (i.e. chilling) of parts of the intrusive body that are in close contact with the extrusive wall rock.

The creek is characterized by intrusive units (porphyritic granodiorite to the west, porphyritic diorite to the east) and strongly altered magmatic-hydrothermal breccia in between the two intrusive bodies and on the northern hill (Figure 28). Jigsaw texture igneous breccias with subangular clasts of intrusive and extrusive rocks, some hosting hydrothermal biotite, were observed in the creek and on the southern hill (Figure 24 f.).

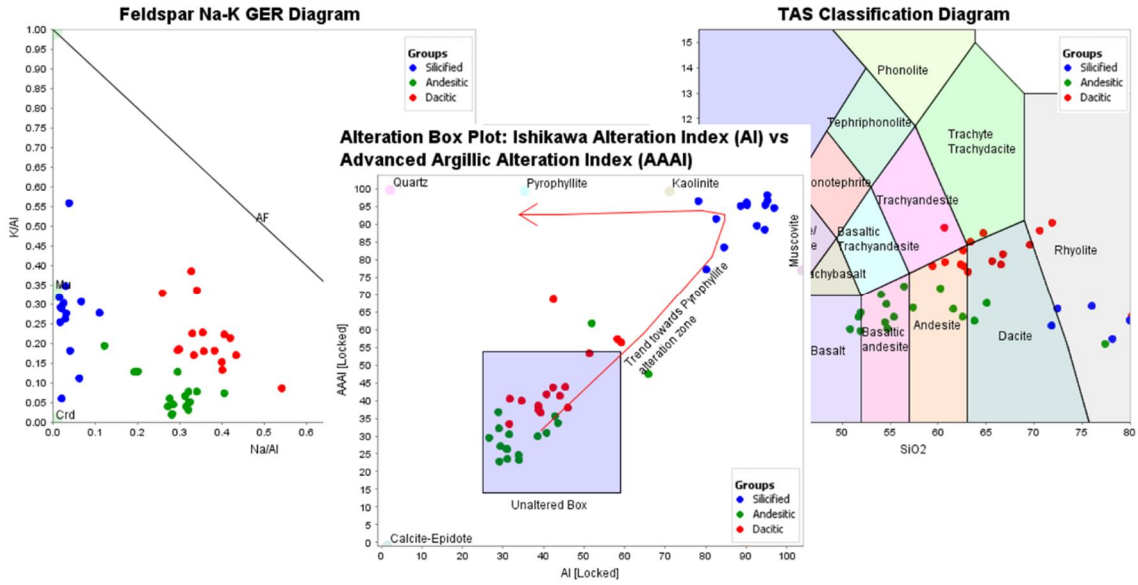

Figure 10: Preliminary division of whole-rock geochemical samples using the feldspar Na-K diagram, the alteration box plot diagram, and the TAS diagram.

The average observed magnetic susceptibility value was 37.1 for intrusive units and 41.1 for extrusive units, whereas the magnetic susceptibility of the intrusive units differed substantially: the porphyritic granodiorite had a much lower average magnetic susceptibility value (12) than the porphyritic diorite (47).

Petrographic description

The intrusive units could be distinguished using petrographic methods. A defining difference was that the porphyritic diorite generally showed amphibole phenocrysts (Figure 18 e. and f.), whereas the porphyritic granodiorite did not. The groundmass of the porphyritic diorite samples was very fine-grained plagioclase feldspar altered to either chlorite and epidote, or illite and illite/smectite (Figure 18 c. and d.), whereas the groundmass of the porphyritic granodiorite samples consisted of fine-grained quartz, potassium feldspar, and minor plagioclase feldspar (Figure 20 c. and d.). The plagioclase feldspar phenocrysts were generally relatively altered in the porphyritic diorite samples: in some they were pervasively altered to illite (Figure 40 a. and b.), while in others they were not as pervasively altered (Figure 18 a. and b.). The plagioclase phenocrysts in the porphyritic granodiorite samples were generally pervasively altered and sparse (Figure 20 e. and f.).

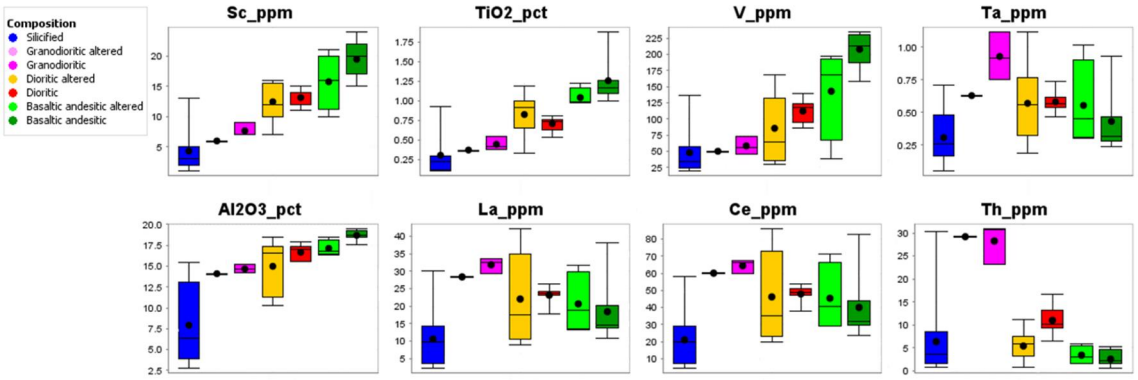

Figure 11: Box plots of immobile trace elements in the whole-rock geochemical samples.

Geochemical description

A total of 47 samples for whole-rock geochemical analysis were collected from the Ronaldo prospect. The aim was to study the different lithological units and their relationships based on their geochemical signature. A preliminary inspection of the K/Al and Na/Al ratios, alteration signatures, and prevalence of SiO_2 versus alkalis ($NaO + K_2O$) (Figure 10) revealed four relatively distinct data point clusters. This was in accord with

the field observations since samples were mostly taken from the extrusive rocks, the porphyritic diorite and porphyritic granodiorite intrusive rocks, and the silicified ridges. These four lithologic classes were roughly identified in the whole-rock geochemical assay results. To classify the intrusive and extrusive units, altered rock samples were ruled out from the data using constraints such as <70 wt. % SiO_2 and the plot of N/Al versus Na/Al using molar ratios (the feldspar Na-K diagram), the alteration box plot AI vs AAAI, and the TAS volcanic diagram (Figure 10).

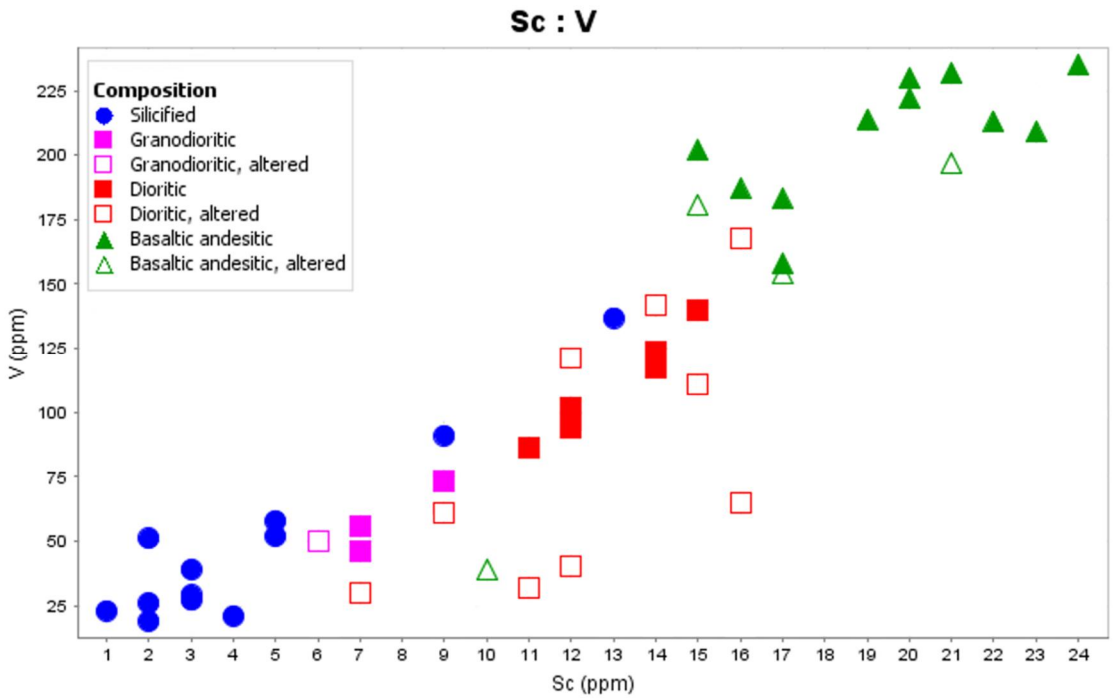

Figure 12: Unaltered and altered samples visualized with immobile trace elements.

Generally, intrusive rocks were found to be more altered than extrusive rocks, which was in line with the field observations. From this it was deducted that the intrusive units were more permeable and thus were subjected to more intense alteration. Samples that were clearly altered but were classified as unaltered or vice versa in the preliminary classification of the samples were further inspected using trace element data. Using immobile trace elements such as Sc, Ti, V, Ta, Al, La, Ce, and Th, the uncertain samples were further divided into the most representative classes, taking the field observations into account as well. First the uncertain samples were classified using Sc, which is an

immobile trace element that replaces Fe in crystal structures and can thus be used to estimate how mafic a rock was prior to alteration (Floyd et al. 1978). This was especially useful for samples in the case of which it was unclear during field mapping if the rock

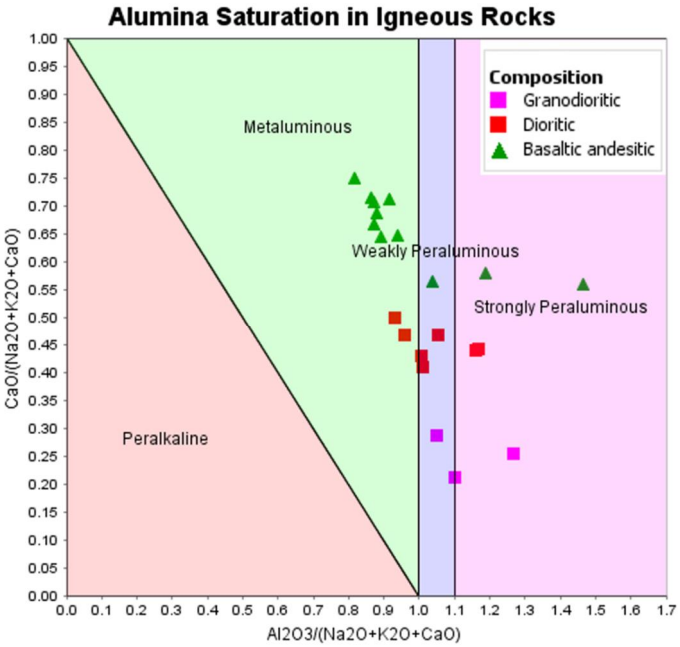

Figure 13: Aluminium saturation of unaltered intrusive and extrusive rock units at Ronaldo.

was intrusive or extrusive due to hydrothermal alteration and fine graininess of the sample. After this, other trace elements were used to classify the uncertain samples (Figure 11). The unaltered and altered samples were quite distinguishable in terms of immobile trace elements (Figure 12), as can also be seen in Figure 11. The samples were found to belong to the basaltic, basaltic andesitic, andesitic, dacitic, and rhyolitic fields (Figure 14). Henceforth, the intrusive samples mostly clustering in the andesitic (dioritic), and to some extent in the dacitic (granodioritic) fields, will be called dioritic, whereas the intrusive samples clustering in the dacitic (granodioritic) and rhyolitic (granitic) fields will be called granodioritic (the inferred corresponding intrusive names in parentheses). Extrusive samples mostly clustering in the basaltic andesitic, and to some extent in the basaltic fields, will be called basaltic andesitic. The subalkaline, unaltered basaltic andesitic, dioritic, and granodioritic samples are presented in the TAS diagram in Figure 14.

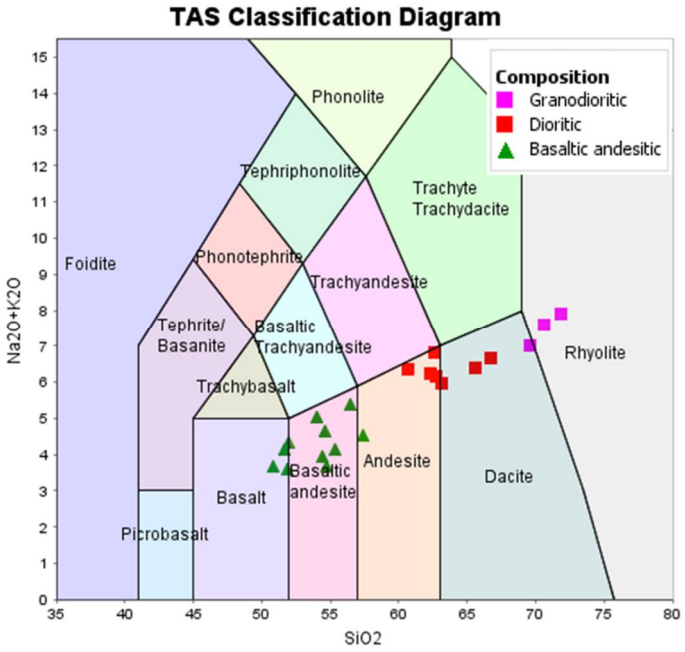

Figure 14: TAS diagram of unaltered intrusive and extrusive rock units at Ronaldo.

The unaltered intrusive rocks were dioritic to granodioritic in composition (Figure 14). The granodioritic samples also belong to the granitic field, but this is due to hydrothermal alteration and consequent loss in mobile elements. The samples were thus regarded as granodioritic. The values of the intrusive rocks ranged from ~61 to 72 wt. % SiO_2 and 6.0 to 8.0 wt. % NaO + K_2O. The intrusive rocks were generally weakly peraluminous (Figure 13). All intrusive samples were calc-alkaline (Figure 15) and were representative of a medium K calc-alkaline series.

In regards to aluminium saturation, the observed intrusions at Ronaldo were generally weakly peraluminous, which correlates with the general trend of mineralized porphyries (Figure 16), as discussed in Seedorf 2005.

The altered intrusive samples were separated into dioritic and granodioritic categories using immobile trace elements (Figure 11). The granodioritic samples have clearly been subjected to more hydrothermal alteration, which is evident from the TAS diagram (Figure 14) and the feldspar Na-K diagram (elevated K/Al ratio) (Figure 10). The feldspar Na-K diagram was used to classify and separate samples based on the degree of alteration they have been subjected to.

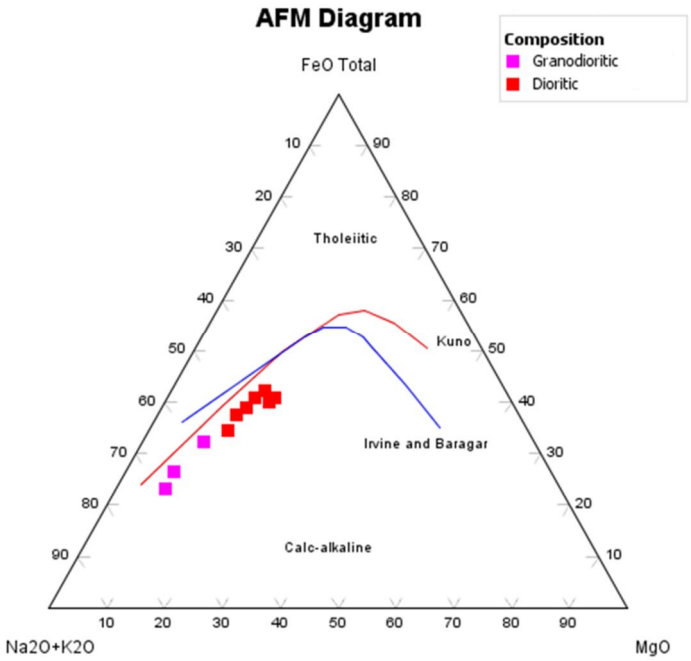

Figure 15: AFM diagram of unaltered intrusive rock units at Ronaldo.

The clearest difference in trace element compositions of intrusive samples (dioritic and granodioritic) could be seen in the highly elevated concentrations of Th in the granodioritic samples (Figure 11). There were higher concentrations of elements such as Nb, Ta, La, and Ce in the granodioritic samples than in the dioritic samples, whereas the concentrations of elements such as Sc, Ti, V, and Al were lower in the granodioritic samples than in the dioritic samples. All four porphyritic granodiorite samples had less mobile trace elements due to having been subjected to hydrothermal alteration, but their immobile trace element contents clearly showed that they differ from samples taken from silicified ridges or vein material (elevated Y, Nb, Ta, Al, La, Ce, and Th). Thus, they belong to neither the dioritic nor the silicified samples, and instead constitute their own granodioritic group. PES011241 was clearly more enriched in SiO_2 and depleted in Na and K (Table 1) and could thus be considered to be altered granodioritic and was not taken into further consideration. Dioritic samples clustered around the same rather

confined area in the feldspar Na-K diagram (Figure 10), while they also clustered in the diorite and granodiorite fields in the TAS diagram (Figure 14).

The unaltered extrusive rocks were mostly basaltic andesitic to basaltic in composition (Figure 14). The values of the extrusive rocks ranged from ~51 to 57 wt. % SiO_2 and 3.6 to 5.4 wt. % NaO + K_2O. The extrusive rocks were depleted in potassium (Na:K 3:1) compared to the intrusive rocks (Na:K 2:1). Nearly all the extrusive samples were also calc-alkaline in composition and belonged to a medium K calc-alkaline series. The extrusive rocks were generally metaluminous (Figure 13).

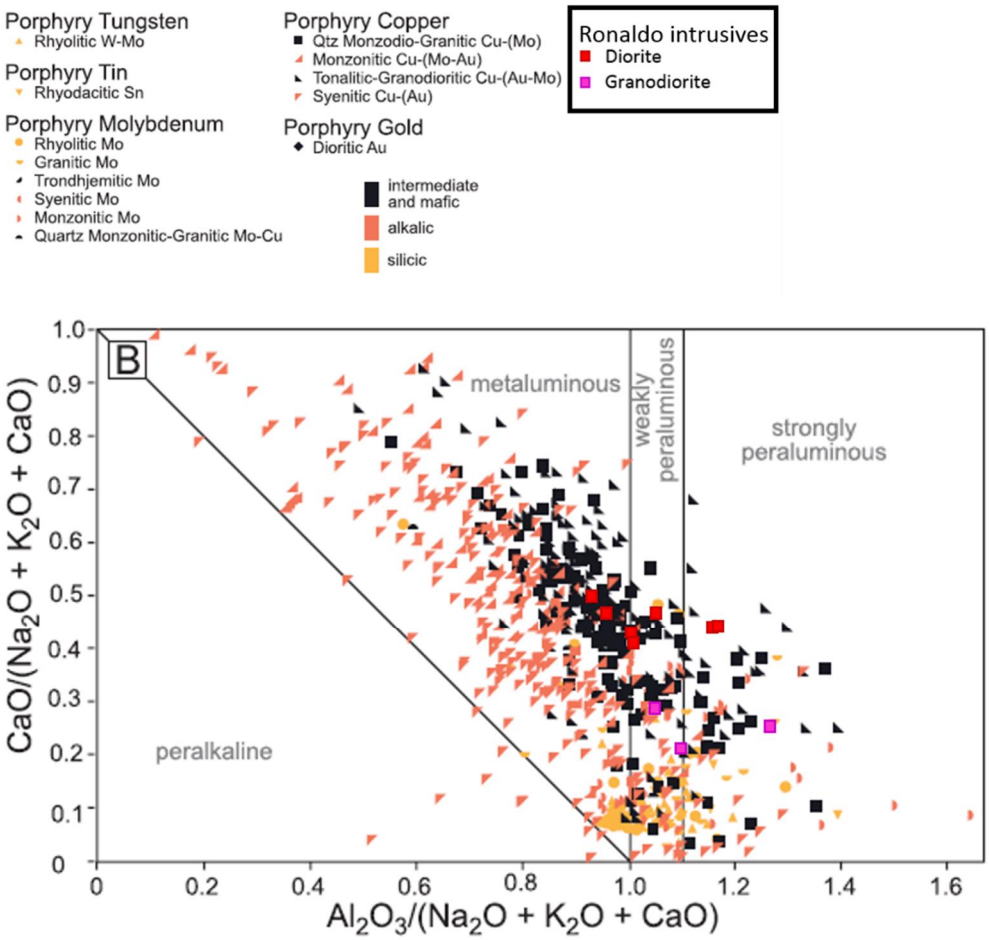

Figure 16: Intrusive samples from Ronaldo related to other rock suites hosting porphyry Cu±Mo±Au mineralization, compiled by Seedorf 2005.

Table 1: Whole-rock geochemical analysis results. The analysis methods for each element are detailed in the methods section.

		SiO_2	Al_2O_3	Fe_2O_3	MgO	CaO	Na_2O	K_2O	TiO_2	P_2O_5	MnO	BaO	Ag	As	Au	Ba	Be	Bi	Cd	Ce	Co	Cr	Cu
		%	%	%	%	%	%	%	%	%	%	%	ppm	ppm	ppm	ppm	ppm	ppm	ppm	ppm	ppm	ppm	ppm
	Rock Type	ME-ICP06	ME-ICP06	ME-ICP06	ME-ICP06	ME-ICP06	ME-ICP06	ME-ICP06	ME-ICP06	ME-ICP06	ME-ICP06	ME-ICP06	ME-4ACD81	ME-MS61r	Au-AA23	ME-MS61r	ME-MS61r	ME-MS61r	ME-4ACD81	ME-MS61r	ME-4ACD81	ME-MS61r	ME-4ACD81
PES011227	Porphyritic basaltic andesite	51.89	18.76	9.63	4.84	9.48	3.22	0.38	1.18	0.28	0.25	0.03	n.d.	27.4	0.005	270	1.01	0.07	n.d.	32.2	33	50	90
PES011229	Porphyritic basaltic andesite	51.67	19.23	9.79	4.65	8.77	3.34	0.81	1.19	0.28	0.17	0.05	n.d.	30.9	n.d.	460	0.88	0.05	n.d.	31.8	32	50	42
PES011230	Diorite	60.66	17.03	6.94	1.87	3.94	4.34	3.36	1.19	0.46	0.12	0.07	n.d.	16.9	n.d.	700	2.54	0.07	n.d.	86.3	8	11	18
PES011231	Porphyritic diorite	62.60	16.97	6.36	2.15	3.98	3.95	2.86	0.73	0.19	0.11	0.07	n.d.	37.5	n.d.	660	1.45	2.38	n.d.	49.6	14	8	27
PES011233	Porphyritic basaltic andesite	54.58	18.49	9.08	3.95	7.80	3.52	1.14	1.00	0.21	0.15	0.05	n.d.	8.3	n.d.	390	0.91	0.01	n.d.	29.8	26	16	46
PES011237	Porphyritic basaltic andesite	54.05	18.93	9.24	3.32	7.52	3.70	1.35	1.26	0.32	0.21	0.06	n.d.	21.6	n.d.	520	1.16	0.05	n.d.	43.7	24	15	38

PES011240	Silicified ridge	86.63	8.28	2.28	0.10	0.08	0.16	2.11	0.25	0.06	0.01	0.04	n.d.	41.6	0.007	370	0.23	1.33	n.d.	21.9	1	11	33
PES011241	Porphyritic granodiorite	76.03	14.10	3.88	0.65	0.27	0.58	4.00	0.37	0.05	0.02	0.06	n.d.	18	n.d.	590	0.95	1.6	n.d.	60.1	6	9	43
PES011243	Porphyritic granodiorite	71.89	14.20	2.97	0.99	1.51	2.83	5.06	0.38	0.07	0.04	0.07	n.d.	11.8	n.d.	650	1.76	0.12	n.d.	67.2	6	8	22
PES011246	Silicified ridge	91.73	4.21	1.22	0.15	0.16	0.10	2.18	0.12	0.03	0.03	0.08	3	14.5	0.022	670	0.4	0.09	n.d.	6.79	1	15	93
PES011247	Porphyritic diorite	60.70	17.97	7.10	2.90	3.75	3.27	3.07	0.81	0.18	0.15	0.07	n.d.	29.9	n.d.	650	1.09	0.05	n.d.	38.1	18	6	35
PES011248	Porphyritic diorite	62.56	17.64	5.15	3.65	5.58	2.07	2.09	0.91	0.21	0.04	0.05	n.d.	21.9	n.d.	430	1.14	0.21	n.d.	34.4	18	16	19
PES011249	Porphyritic diorite	61.59	18.52	4.12	4.03	5.82	2.27	2.20	1.07	0.23	0.05	0.05	n.d.	23.2	n.d.	400	0.95	0.15	n.d.	24.6	16	40	99
PES011250	Porphyritic basaltic andesite	57.39	18.53	8.00	2.99	7.03	3.66	0.87	1.10	0.25	0.10	0.03	n.d.	41.1	n.d.	300	0.94	0.2	n.d.	31.3	20	27	39
PES011251	Porphyritic diorite	64.70	16.55	6.01	1.91	2.30	4.09	3.40	0.71	0.17	0.07	0.07	n.d.	33.9	n.d.	680	1.17	0.07	n.d.	47.8	10	5	9
PES011252	Diorite	94.16	2.70	1.65	0.31	0.10	0.05	0.87	0.10	0.03	0.02	0.01	1.1	76.7	0.037	120	0.25	0.18	n.d.	4.17	2	16	28
PES011253	Diorite	71.85	11.75	10.87	1.10	0.23	0.79	3.02	0.33	0.02	0.02	0.04	n.d.	68.5	0.016	300	0.78	0.94	n.d.	21.2	67	9	30
PES011256	Diorite	63.36	16.97	5.95	1.55	3.49	4.47	2.66	0.93	0.34	0.15	0.10	n.d.	22.6	n.d.	900	1.77	0.47	n.d.	71.7	8	8	11

PES011258	Magmatic-hydrothermal breccia	66.53	15.27	5.73	2.27	2.48	5.03	1.21	0.92	0.40	0.11	0.03	0.9	22.1	0.009	310	1.49	0.46	n.d.	74.5	12	4	148
PES011259	Magmatic-hydrothermal breccia	80.18	10.86	2.81	0.67	0.34	2.64	1.53	0.60	0.29	0.04	0.04	52.1	30	0.297	370	1.13	1.91	230	35.3	16	5	3060
PES011263	Porphyritic granodiorite	69.55	15.23	4.43	1.31	1.68	2.40	4.62	0.54	0.11	0.06	0.08	n.d.	22.2	n.d.	710	1.6	0.21	n.d.	60	8	8	22
PES011266	Porphyritic granodiorite	70.59	14.61	3.43	0.96	2.19	3.03	4.55	0.41	0.09	0.06	0.07	n.d.	15.5	n.d.	680	1.54	0.14	n.d.	66.1	5	7	21
PES011278	Silicified ridge	92.40	4.20	1.90	0.62	0.06	0.16	0.44	0.16	0.04	0.01	0.01	84.8	188.5	0.992	50	0.5	0.78	n.d.	7.17	1	26	35
PES011279	Porphyritic basaltic andesite	54.72	19.54	11.50	4.78	4.10	3.35	0.34	1.09	0.30	0.20	0.05	1.5	3.8	n.d.	430	1	0.06	n.d.	23.5	34	22	28
PES011285	Porphyritic diorite	63.12	17.10	6.76	2.32	3.55	3.08	2.88	0.76	0.20	0.12	0.07	n.d.	10	n.d.	670	1.36	0.01	n.d.	47.3	11	6	9
PES011288	Porphyritic diorite	65.62	15.61	5.47	1.79	4.20	3.13	3.24	0.63	0.13	0.07	0.08	n.d.	39.2	0.006	760	1.16	0.22	n.d.	46.9	9	11	32
PES011290	Silicified ridge	80.62	15.50	2.27	0.03	0.05	0.20	0.87	0.30	0.13	0.01	0.03	n.d.	35.6	n.d.	270	0.36	1.17	n.d.	57.9	n.d.	6	19
PES011292	Ignimbrite	65.08	18.53	4.50	3.60	2.20	1.38	3.32	0.98	0.22	0.12	0.05	n.d.	15.1	n.d.	470	2.32	0.02	n.d.	71.4	5	4	4

PES013104	Porphyritic basaltic andesite	54.43	17.53	12.04	4.58	4.71	3.42	0.51	1.84	0.62	0.24	0.03	n.d.	60.3	n.d.	280	1.7	0.12	n.d.	73.1	27	55	36
PES013106	Basaltic andesite	77.40	10.32	5.24	1.90	1.04	1.86	1.22	0.75	0.19	0.07	0.02	0.6	24.6	0.026	170	0.92	0.23	n.d.	19.7	12	27	28
PES013109	Porphyritic basaltic andesite	56.45	19.26	8.27	3.11	5.78	3.99	1.39	1.17	0.29	0.18	0.06	n.d.	46.8	n.d.	540	0.97	0.02	n.d.	31.1	17	20	32
PES013112	Porphyritic basaltic andesite	63.76	16.33	6.76	2.59	5.15	3.20	0.79	0.97	0.24	0.13	0.04	0.5	56.3	0.007	340	1.04	0.22	n.d.	29	17	23	43
PES013116	Silicified ridge	94.25	2.91	1.86	0.12	0.01	0.03	0.68	0.10	0.02	0.01	0.01	4110	1280	16.65	90	0.33	2.91	1.6	6.5	n.d.	21	36
PES013121	Porphyritic basaltic andesite	60.23	16.82	7.65	2.86	5.69	4.15	1.14	1.00	0.24	0.13	0.04	3.2	33.9	0.032	320	0.95	0.07	n.d.	29.8	23	26	56
PES013122	Silicified ridge	78.16	12.58	4.19	0.61	0.06	0.23	3.05	0.93	0.16	0.01	0.03	1.1	32.7	0.038	310	0.64	4.07	n.d.	38.5	n.d.	11	11
PES013123	Silicified ridge	92.59	3.70	2.37	0.33	0.01	0.09	0.62	0.19	0.08	0.01	0.01	392	454	1.81	110	0.72	1.31	n.d.	11.1	n.d.	29	32
PES013124	Porphyritic diorite	66.73	15.61	4.90	1.75	3.49	3.37	3.29	0.54	0.12	0.11	0.07	1	14.8	0.006	600	1.57	0.06	n.d.	54	11	9	16
PES013126	Porphyritic basaltic andesite	50.82	18.03	12.00	4.80	7.72	2.99	0.67	1.88	0.67	0.33	0.04	n.d.	15.1	n.d.	280	1.93	0.14	n.d.	83	21	61	28

PES013128	Porphyritic diorite	62.33	17.36	6.49	2.16	4.24	3.52	2.73	0.73	0.18	0.14	0.08	n.d.	14.6	0.005	690	1.4	0.07	n.d.	50.8	12	8	15
PES013131	Silicified ridge	72.46	15.16	6.25	0.66	0.04	0.24	4.23	0.81	0.09	0.01	0.05	n.d.	842	0.133	500	0.98	1.98	n.d.	30.4	n.d.	11	37
PES013133	Silicified ridge	86.38	7.17	3.61	0.28	0.04	0.08	1.94	0.29	0.09	0.09	0.02	159	416	0.535	190	0.88	0.5	n.d.	17.65	3	16	30
PES013136	Silicified ridge	91.39	5.50	1.16	0.22	0.01	0.07	1.47	0.11	0.06	0.01	0.01	25.9	16.4	1.735	100	0.91	0.14	n.d.	24.3	1	13	7
PES013141	Silicified ridge	79.96	13.22	2.06	0.31	0.01	0.12	3.89	0.29	0.05	0.02	0.06	n.d.	17.6	0.251	550	1.29	0.22	n.d.	26	2	5	11
PES013143	Ignimbrite	59.40	16.85	8.08	2.33	5.41	4.11	2.07	1.22	0.29	0.14	0.06	n.d.	16.3	n.d.	580	1.38	0.06	n.d.	51.3	14	6	12
PES013145	Porphyritic basaltic andesite	51.91	18.90	9.79	5.34	8.12	3.63	0.70	1.09	0.27	0.15	0.03	n.d.	156	0.019	300	0.89	0.02	n.d.	25.2	33	30	5
PES013147	Porphyritic basaltic andesite	55.38	18.51	8.16	4.03	8.27	3.11	1.03	1.02	0.25	0.13	0.05	n.d.	16.3	n.d.	410	0.98	2.07	n.d.	35.5	27	42	79
PES013148	Porphyritic diorite	62.71	16.05	6.54	2.66	4.74	3.49	2.67	0.75	0.16	0.14	0.06	n.d.	18.7	n.d.	560	1.21	0.16	n.d.	48.9	16	35	32

		Cs	Ga	Ge	Hf	Hg	In	La	Li	Mn	Mo	Nb	Ni	P	Pb	Rb	Re	S	Sb	Sc	Se	Sm	Sn
		ppm	ppm	ppm	ppm	ppm	ppm	ppm	ppm	ppm	ppm	ppm	ppm	ppm	ppm	ppm	ppm	ppm	ppm	ppm	ppm	ppm	ppm
	Rock Type	ME-MS61r	ME-MS61r	ME-MS61r	ME-MS61r	ME-MS42	ME-MS61r	ME-MS61r	ME-4ACD81	ME-MS61r	ME-4ACD81	ME-MS61r	ME-4ACD81	ME-MS61r	ME-4ACD81	ME-MS61r	ME-MS61r	ME-MS61r	ME-MS61r	ME-4ACD81	ME-MS61r	ME-MS61r	ME-MS61r
PES011227	Porphyritic basaltic andesite	1.8	20.9	0.12	0.4	0.016	0.069	14.6	20	1960	n.d.	5.8	29	1250	20	9.5	0.002	2000	2.37	20	n.d.	4.45	1.3
PES011229	Porphyritic basaltic andesite	2.21	21	0.13	0.6	0.011	0.065	15.3	20	1340	1	5.5	36	1220	4	14.9	n.d.	100	3.49	20	1	4.46	1
PES011230	Diorite	17.85	22.9	0.19	0.3	0.012	0.067	42.3	30	970	1	20.2	1	2090	28	102.5	n.d.	100	1.65	16	n.d.	9.47	3.1
PES011231	Porphyritic diorite	2.66	19.2	0.11	0.9	0.015	0.247	24.3	30	851	n.d.	8	7	790	14	99.9	n.d.	n.d.	1.79	12	n.d.	4.6	1.6
PES011233	Porphyritic basaltic andesite	1.64	21.2	0.12	0.4	0.018	0.055	13.7	10	1100	n.d.	4.7	11	850	5	19.4	n.d.	100	0.74	23	n.d.	3.69	1.3
PES011237	Porphyritic basaltic andesite	1.63	22.1	0.14	0.5	0.011	0.063	20.1	20	1520	n.d.	8.5	9	1360	6	24.9	n.d.	100	2.2	19	n.d.	5.66	1.5
PES011240	Silicified ridge	3.29	14.9	0.08	0.2	0.025	0.106	10.7	20	85	12	4.7	n.d.	270	7	98.7	n.d.	200	4.69	5	2	1.74	2.8

PES011241	Porphyritic granodiorite	8.72	20.7	0.13	0.2	0.038	0.136	28.4	20	134	5	5.4	2	210	21	214	0.003	21500	4.13	6	3	4.88	2.8
PES011243	Porphyritic granodiorite	3.94	17.4	0.15	0.5	0.011	0.074	33.6	10	294	4	10.7	2	350	12	227	0.006	5300	2.52	7	1	4.85	2.6
PES011246	Silicified ridge	2.78	3.2	0.05	0.3	0.024	0.015	3.4	90	208	9	1.8	2	130	39	99.5	n.d.	300	10.85	2	n.d.	0.84	0.5
PES011247	Porphyritic diorite	5.15	20.3	0.13	1.2	n.d.	0.057	17.7	30	1100	2	6.6	5	780	35	106	n.d.	3000	4.16	15	n.d.	4.37	1.6
PES011248	Porphyritic diorite	2.12	16.95	0.11	0.2	0.009	0.034	15.6	40	323	3	5.3	10	860	14	69.9	0.008	22400	2.93	14	3	4.18	4.4
PES011249	Porphyritic diorite	6.75	19.65	0.11	0.2	0.012	0.041	10.7	40	333	10	4.4	21	920	15	81.9	0.012	9300	2.77	16	2	3.25	4.6
PES011250	Porphyritic basaltic andesite	1.52	21.4	0.15	0.2	0.015	0.073	13.8	10	751	2	5.9	12	1170	13	29.3	0.003	5300	5.82	16	1	4.09	2.6
PES011251	Porphyritic diorite	3.29	19.4	0.12	1.4	0.012	0.052	23.3	20	508	2	7.7	3	810	5	149	n.d.	400	4.42	15	n.d.	4.63	1.6
PES011252	Diorite	2.76	3.29	0.05	n.d.	0.011	0.011	2.1	100	114	3	0.9	2	120	50	51.4	n.d.	1100	20.5	2	n.d.	0.44	0.5
PES011253	Diorite	6.77	10.2	0.14	0.1	0.009	0.055	10.3	20	140	2	7.2	4	110	6	141	0.021	49700	2.16	9	8	1.55	2.7
PES011256	Diorite	2.3	22.3	0.16	0.3	0.01	0.063	33.7	10	1140	1	14.9	n.d.	1580	32	63.7	0.002	3900	1.79	11	1	7.54	2.4

PES011258	Magmatic-hydrothermal breccia	2.57	20.7	0.15	0.3	0.009	0.067	36.3	10	820	303	11.8	2	1700	15	42.4	5.74	10200	1.48	12	2	8.51	2.6
PES011259	Magmatic-hydrothermal breccia	4.67	11.75	0.24	n.d.	1.68	0.056	17.4	60	278	3	8.1	3	1330	25300	78.8	0.013	23500	26.9	7	50	3.53	1.6
PES011263	Porphyritic granodiorite	3.93	17	0.13	0.5	0.008	0.04	29.4	20	436	2	8.1	6	480	41	231	n.d.	1200	2.19	9	n.d.	5.44	2.2
PES011266	Porphyritic granodiorite	3.88	17.7	0.12	0.5	0.03	0.063	32.6	10	426	1	9.1	3	380	40	222	0.003	100	3.48	7	n.d.	5.55	2.1
PES011278	Silicified ridge	1.76	4.59	0.06	0.1	0.236	0.066	3.5	130	59	16	0.6	n.d.	180	125	23.2	0.002	300	74.1	3	2	0.69	5.1
PES011279	Porphyritic basaltic andesite	6.87	21.2	0.16	0.1	0.056	0.053	12.1	50	1400	n.d.	4.9	34	960	27	4.2	n.d.	200	1.11	22	n.d.	3.69	1.6
PES011285	Porphyritic diorite	1.85	20	0.15	0.6	0.046	0.059	23.7	20	931	n.d.	7.9	3	780	15	69.2	n.d.	n.d.	1.84	14	n.d.	5.23	1.4
PES011288	Porphyritic diorite	1.81	17.85	0.13	0.6	0.022	0.077	23.1	20	537	3	7.8	7	580	10	96	0.011	2400	1.66	12	1	4.73	1.5
PES011290	Silicified ridge	0.94	10.65	0.11	0.6	0.033	0.013	30.1	10	25	6	4.2	2	480	61	30.2	n.d.	700	18.5	3	2	3.49	1.7
PES011292	Ignimbrite	27.7	24.9	0.17	0.7	0.019	0.079	31.7	80	921	1	17.6	2	910	11	163	n.d.	100	4.15	10	n.d.	8.35	2.7

PES013104	Porphyritic basaltic andesite	3.2	22.8	0.21	0.4	0.016	0.066	34.6	50	1760	n.d.	14.3	43	2590	12	17.3	n.d.	2400	2.58	21	1	9.34	2.5
PES013106	Basaltic andesite	6.92	13.05	0.08	0.1	0.028	0.027	8.9	80	588	5	3.5	12	820	5	78.6	0.002	12800	26.2	12	1	2.69	1.5
PES013109	Porphyritic basaltic andesite	1.42	24.1	0.14	0.2	0.016	0.051	13.7	30	1370	n.d.	6.6	11	1250	38	37.8	0.007	3900	3.67	17	1	4.17	3.6
PES013112	Porphyritic basaltic andesite	1.85	19.85	0.14	0.2	n.d.	0.08	13.3	30	995	267	6.1	11	1010	12	31.6	3.89	8100	4.13	15	2	3.6	3.2
PES013116	Silicified ridge	3.18	4.91	0.21	n.d.	3.27	0.268	3.5	110	56	795	0.3	1	110	2110	41	0.002	1000	1255	2	18	0.75	3
PES013121	Porphyritic basaltic andesite	1.29	18.95	0.12	0.3	0.056	0.106	13.6	20	980	4	5.8	16	1080	22	42.2	0.004	100	5.43	17	n.d.	3.9	3.3
PES013122	Silicified ridge	3.85	17.85	0.07	0.3	0.076	0.064	18.5	30	30	33	4.7	n.d.	690	63	123.5	0.003	500	26.1	9	4	3.29	2.7
PES013123	Silicified ridge	2.79	4.51	n.d.	n.d.	0.714	0.035	5.5	120	63	123	0.6	1	400	1045	41.7	n.d.	300	247	3	5	1.07	2.1
PES013124	Porphyritic diorite	2.75	17.85	0.08	0.3	0.032	0.049	26.4	10	774	1	8.4	7	520	20	121.5	n.d.	n.d.	2.34	11	n.d.	4.75	1.2
PES013126	Porphyritic basaltic andesite	4.25	26	0.17	0.3	0.029	0.121	38.3	30	2480	n.d.	15.6	39	2950	19	26.1	n.d.	300	2.68	24	1	10.85	3.4

PES013128	Porphyritic diorite	2.93	20.8	0.1	0.4	0.047	0.062	23.6	10	1040	1	7.4	7	750	15	100	n.d.	n.d.	1.48	14	n.d.	5.21	1.7
PES013131	Silicified ridge	6.48	24	0.09	0.3	0.136	0.13	14.9	30	71	6	2.7	1	440	9	201	n.d.	300	32.3	13	3	2.64	2.2
PES013133	Silicified ridge	9.53	9.71	0.06	0.1	0.147	0.028	8.8	100	701	21	2.7	1	400	227	102	n.d.	200	85.6	5	3	1.69	4.2
PES013136	Silicified ridge	6.84	7.66	n.d.	0.5	0.056	0.006	13	110	81	122	3.6	n.d.	300	51	90.9	n.d.	n.d.	40.8	1	n.d.	2.38	0.6
PES013141	Silicified ridge	9.07	17.45	n.d.	0.6	0.009	0.022	12.8	20	129	2	10.1	n.d.	230	8	208	n.d.	100	6.02	4	1	1.71	4.8
PES013143	Ignimbrite	5.66	23.7	0.12	4.2	0.027	0.063	24.1	30	1080	2	9.2	n.d.	1420	21	61.9	n.d.	n.d.	1.9	21	n.d.	5.92	1.8
PES013145	Porphyritic basaltic andesite	1.41	22.2	0.1	1.5	0.02	0.042	10.8	30	1140	1	4.4	47	1210	n.d.	8.1	n.d.	n.d.	7.59	15	n.d.	3.59	0.8
PES013147	Porphyritic basaltic andesite	3.55	22.3	0.1	0.3	0.02	0.056	15.6	20	1030	1	6.3	26	1050	9	18.8	n.d.	n.d.	3.28	17	1	4.26	1.5
PES013148	Porphyritic diorite	1.64	20.5	0.11	0.8	0.021	0.069	23.2	20	1080	1	7.4	10	730	12	110.5	n.d.	n.d.	1.88	14	n.d.	5.12	2

		Sr	Ta	Te	Th	Tl	U	V	W	Y	Zn	Zr	Dy	Er	Eu	Gd	Ho	Lu	Nd	Pr	Tb	Tm	Yb
		ppm	ppm	ppm	ppm	ppm	ppm	ppm	ppm	ppm	ppm	ppm	ppm	ppm	ppm	ppm	ppm	ppm	ppm	ppm	ppm	ppm	ppm
	Rock Type	ME-MS61r	ME-MS61r	ME-MS61r	ME-MS61r	ME-MS61r	ME-MS61r	ME-MS61r	ME-MS61r	ME-MS61r	ME-4ACD81	ME-MS61r	ME-MS61r	ME-MS61r	ME-MS61r	ME-MS61r	ME-MS61r	ME-MS61r	ME-MS61r	ME-MS61r	ME-MS61r	ME-MS61r	ME-MS61r	ME-MS61r
PES011227	Porphyritic basaltic andesite	579	0.31	n.d.	1.62	0.1	0.3	222	0.5	18.9	154	10.8	3.56	1.83	1.33	4.06	0.65	0.21	18.7	4.36	0.58	0.24	1.51
PES011229	Porphyritic basaltic andesite	650	0.28	n.d.	1.02	0.11	0.2	230	0.3	18.1	87	14.9	3.57	1.66	1.27	4.14	0.63	0.16	19.2	4.51	0.56	0.2	1.21
PES011230	Diorite	342	1.12	n.d.	11.1	0.3	1.8	65	0.7	37.1	112	11.5	7.4	3.56	1.98	8.73	1.35	0.39	45.5	11.45	1.19	0.47	2.89
PES011231	Porphyritic diorite	369	0.55	n.d.	10.05	0.57	1.7	102	0.9	20.5	52	29.6	3.84	1.98	1.07	4.29	0.7	0.25	23.2	6.05	0.59	0.28	1.73
PES011233	Porphyritic basaltic andesite	508	0.27	n.d.	2.64	0.12	0.5	209	0.4	19.1	103	8.5	3.74	2.04	1.1	3.68	0.72	0.29	16.4	3.91	0.55	0.29	1.88
PES011237	Porphyritic basaltic andesite	547	0.47	n.d.	2.23	0.17	0.4	214	0.4	24.6	100	9.4	4.68	2.32	1.43	5.34	0.88	0.27	24.8	5.76	0.74	0.3	1.89
PES011240	Silicified ridge	32.1	0.5	0.57	10.6	0.62	1.2	58	3.2	4	7	5.6	0.81	0.49	0.18	1.15	0.14	0.06	9.6	2.64	0.12	0.07	0.42
PES011241	Porphyritic granodiorite	49.4	0.63	0.65	29.2	1.15	5.1	50	2.4	15.3	48	5.5	2.96	1.52	0.51	3.62	0.52	0.2	25.2	6.99	0.48	0.21	1.4

PES011243	Porphyritic granodiorite	199	1.12	0.06	31	0.93	6.5	46	1.9	21.3	28	12.5	3.84	2.1	0.61	4.34	0.71	0.28	25.7	7.49	0.6	0.3	2.01
PES011246	Silicified ridge	31.4	0.16	0.26	4.51	1.08	1.8	19	1.2	4.2	41	7.8	0.75	0.44	0.09	0.83	0.15	0.06	3.7	0.93	0.12	0.06	0.4
PES011247	Porphyritic diorite	396	0.47	0.1	6.43	0.92	1.6	140	1.5	20.1	191	33	3.94	2.03	0.99	4.3	0.75	0.23	19.7	4.97	0.62	0.26	1.7
PES011248	Porphyritic diorite	503	0.37	0.5	6.05	0.76	0.8	142	1.8	19.4	35	4.4	3.95	1.9	1.01	4.33	0.71	0.2	18.6	4.48	0.61	0.24	1.5
PES011249	Porphyritic diorite	508	0.28	0.28	3.43	1.02	0.6	168	2.5	15.4	40	3.8	3.13	1.52	1.06	3.21	0.57	0.17	13.8	3.25	0.47	0.21	1.29
PES011250	Porphyritic basaltic andesite	579	0.32	0.41	2.06	0.36	0.4	187	1.1	17	42	5.9	3.64	1.73	1.21	4.13	0.65	0.19	18	4.17	0.59	0.23	1.4
PES011251	Porphyritic diorite	260	0.56	0.08	8.72	1.23	1.9	111	1.7	20.5	34	40.9	3.99	2.04	1.06	4.63	0.75	0.2	22.4	5.8	0.63	0.27	1.59
PES011252	Diorite	16.2	0.05	0.18	0.81	0.5	0.1	26	0.8	1.3	65	2.9	0.28	0.13	0.1	0.38	0.05	0.02	2	0.54	0.05	0.02	0.13
PES011253	Diorite	48.9	0.6	2.22	2.95	1.33	0.4	61	1.3	4.4	15	2.7	0.91	0.42	0.28	1.25	0.16	0.05	8.8	2.51	0.16	0.06	0.41
PES011256	Diorite	402	0.85	0.39	6.24	0.45	0.9	32	1	33	106	9.9	6.96	3.47	1.82	8.14	1.29	0.39	35.1	8.99	1.13	0.47	2.83
PES011258	Magmatic-hydrothermal breccia	272	0.68	0.27	5.85	0.41	0.7	40	1.5	32.3	80	16.5	6.81	3.2	1.9	8.13	1.22	0.34	39.4	9.89	1.09	0.44	2.66

PES011259	Magmatic-hydrothermal breccia	149.5	0.49	0.08	3.91	0.9	0.5	30	3	7.4	20100	2	2.31	0.86	0.72	3.08	0.36	0.08	17.5	4.34	0.39	0.1	0.64
PES011263	Porphyritic granodiorite	207	0.75	0.08	23.1	0.99	5	73	2.7	21.8	87	10	4.16	2.28	0.77	4.67	0.84	0.29	27.9	7.37	0.68	0.33	1.9
PES011266	Porphyritic granodiorite	231	0.92	0.08	30.7	0.93	6.9	56	1.6	26.3	70	12.5	4.92	2.67	0.79	5.44	0.93	0.35	28.4	7.83	0.76	0.38	2.43
PES011278	Silicified ridge	14.5	n.d.	2.6	2.33	0.27	0.4	29	0.2	2.1	39	3.6	0.44	0.22	0.13	0.56	0.08	0.03	3.3	0.84	0.07	0.03	0.2
PES011279	Porphyritic basaltic andesite	460	0.29	n.d.	1.6	0.25	0.3	213	0.3	21.8	144	3	3.84	2.1	1.29	4.06	0.74	0.24	15.7	3.61	0.59	0.27	1.67
PES011285	Porphyritic diorite	438	0.58	n.d.	10.25	0.55	1.5	122	1.1	23.8	99	20.3	4.59	2.27	1.11	5.1	0.84	0.23	24.4	6.16	0.73	0.3	1.82
PES011288	Porphyritic diorite	362	0.62	n.d.	13.3	0.31	2.5	94	0.9	23.9	43	14.1	4.48	2.4	0.88	4.71	0.85	0.31	21.8	5.78	0.68	0.34	2.17
PES011290	Silicified ridge	203	0.46	0.15	30.4	0.36	2	27	1.4	3.8	7	19.6	0.84	0.38	0.49	2.13	0.14	0.06	21.2	6.34	0.17	0.05	0.33
PES011292	Ignimbrite	360	1.02	n.d.	5.92	1.21	0.9	39	0.5	22.1	87	31.4	5.08	2.07	1.8	7.32	0.84	0.19	39.1	9.76	0.91	0.26	1.44
PES013104	Porphyritic basaltic andesite	351	0.87	0.06	4.64	0.24	0.6	232	1.2	35.9	121	8.9	7.88	3.51	2.15	9.43	1.38	0.3	42.8	9.98	1.28	0.43	2.48
PES013106	Basaltic andesite	142.5	0.19	n.d.	0.84	0.88	0.1	121	2.1	11.1	50	4	2.46	1.15	0.76	2.7	0.44	0.1	11.8	2.67	0.4	0.14	0.84

PES013109	Porphyritic basaltic andesite	591	0.39	0.19	2.21	0.51	0.4	158	1.1	16.9	180	6.3	3.87	1.77	1.29	4.4	0.68	0.19	17.7	4.15	0.61	0.23	1.4
PES013112	Porphyritic basaltic andesite	500	0.3	0.18	1.78	0.46	0.4	181	1.1	14.6	68	4.3	3.05	1.4	1.09	3.48	0.52	0.13	16.1	3.83	0.48	0.17	1.04
PES013116	Silicified ridge	28.5	n.d.	16.4	1.14	0.41	0.6	51	0.5	1.5	109	1	0.33	0.17	0.13	0.5	0.06	0.02	2.9	0.81	0.05	0.02	0.16
PES013121	Porphyritic basaltic andesite	516	0.34	n.d.	1.56	0.44	0.3	154	1.4	15.3	71	8.1	3.11	1.56	1.11	3.49	0.59	0.18	17.4	3.97	0.52	0.21	1.19
PES013122	Silicified ridge	17.5	0.29	1.58	5.3	1.16	0.5	91	0.9	5.3	9	9.7	1.33	0.56	0.52	2	0.22	0.05	18.1	4.8	0.25	0.07	0.38
PES013123	Silicified ridge	19.7	n.d.	4.08	1.44	0.44	0.4	39	0.6	3.2	36	1.1	0.67	0.3	0.2	0.78	0.11	0.03	5.3	1.36	0.1	0.04	0.25
PES013124	Porphyritic diorite	311	0.74	n.d.	16.6	0.49	3.9	86	1.5	21.2	75	5.8	3.85	2.2	0.75	4.03	0.77	0.3	23.8	6.48	0.6	0.31	1.98
PES013126	Porphyritic basaltic andesite	467	0.93	n.d.	5.26	0.44	0.8	235	2.2	38.9	154	11.3	7.94	3.8	1.98	9.69	1.44	0.36	50	11.75	1.35	0.46	2.71
PES013128	Porphyritic diorite	400	0.54	n.d.	9.29	0.47	1.6	117	0.5	23.7	64	9.2	4.3	2.39	1.06	4.71	0.85	0.29	26.1	6.44	0.68	0.3	1.97
PES013131	Silicified ridge	26.3	0.17	0.54	3.73	1.7	0.8	137	1.2	7	27	6.5	1.52	0.75	0.54	1.98	0.27	0.07	14.7	3.79	0.26	0.09	0.61
PES013133	Silicified ridge	22.7	0.17	0.19	3.32	1.1	0.7	52	2.8	5	33	8	1.15	0.55	0.33	1.41	0.2	0.06	8.3	2.23	0.2	0.07	0.5
PES013136	Silicified ridge	12.2	0.26	0.09	3.58	0.65	0.7	23	0.6	9.2	10	18.3	1.78	0.92	0.36	2.05	0.34	0.09	12.7	3.27	0.35	0.12	0.72

PES013141	Silicified ridge	28.7	0.71	0.14	9.63	1.66	1	21	1.8	5.6	16	20.8	1.01	0.59	0.21	1.22	0.2	0.08	10.9	3.1	0.17	0.09	0.56
PES013143	Ignimbrite	479	0.56	n.d.	4.53	0.27	1.3	197	0.7	24.6	107	139	4.78	2.57	1.41	5.57	0.94	0.32	27.9	6.68	0.79	0.35	2.2
PES013145	Porphyritic basaltic andesite	680	0.24	n.d.	0.53	0.12	0.2	202	0.3	12.8	97	43.8	2.97	1.36	1.08	3.48	0.52	0.13	16.1	3.52	0.49	0.16	0.97
PES013147	Porphyritic basaltic andesite	550	0.39	0.16	4.65	0.22	1.1	183	0.5	17.2	94	7.5	3.56	1.87	1.12	3.87	0.67	0.24	20	4.77	0.57	0.26	1.56
PES013148	Porphyritic diorite	349	0.57	n.d.	11.2	0.45	2.2	124	2	23.3	82	17.3	4.46	2.45	1.04	4.9	0.9	0.31	24.7	6.17	0.71	0.34	2.12

Note: n.d. = not detected

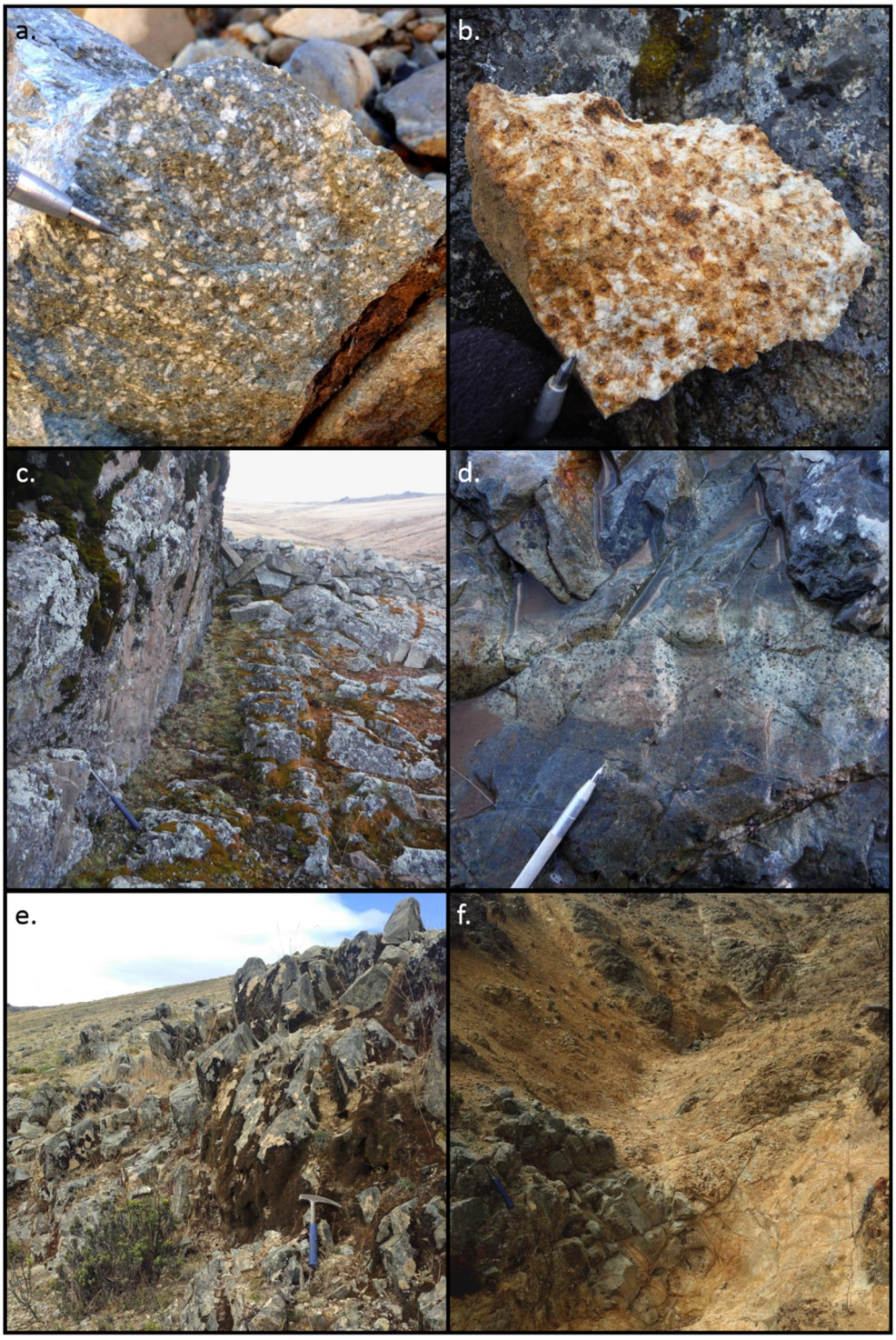

Figure 17: Porphyritic diorite field photographs: **a.)** Porphyritic textured diorite with abundant coarse plagioclase feldspar phenocrysts, altered amphibole phenocrysts, biotite phenocrysts, and very sparse quartz eyes in a very fine-grained groundmass. Field observation RONJG008. **b.)** The colour anomaly observed in satellite imagery originates largely from this intermediate argillic- and advanced argillic-altered porphyritic diorite, in which the plagioclase phenocrysts have altered to kaolinite, while pyrite and other ferrous minerals have altered to goethite. Near field observation RONJG109. **c.)** Igneous contact between porphyritic basaltic andesite (to the left) and porphyritic diorite (to the right). Note that the rock pile in the background is man-made. Field observation RONJG110. **d.)** Light-coloured porphyritic diorite dike crosscutting porphyritic basaltic andesite. Thin magnetite veinlets crosscut both units. Field observation RONJG090. **e.)** Outcrop displaying irregular, sparse fracturing and rounded shapes typical of porphyritic diorite in the prospect. Field observation RONJG121. **f.)** Basaltic andesite roof pendants in intermediate argillic-altered porphyritic diorite. The presence of roof pendants indicates that the top of the intrusion is preserved; it has been exposed by erosion of the overlying rock. Field observation RONJG112.

4.1.1. Porphyritic diorite

Field observations

The central parts of the prospect host a porphyritic diorite intrusion (Figure 28). This porphyritic intrusion is characterized by a non-continuous porphyritic texture, since a wide array of grain sizes was observed throughout the intrusive body, but it is generally characterized by large plagioclase feldspar and altered amphibole and biotite phenocrysts in a very fine-grained groundmass (Figure 17 a. and Figure 18 a. and b.). The porphyritic diorite outcrops generally display rounded shapes and few fractures (Figure 17 e.) compared to the extrusive units. The intrusion is bordered by tourmaline-bearing magmatic-hydrothermal breccia in the creek (Figure 28) and is spatially related to the banded molybdenite quartz (BMQ) veins (Figure 34 b.) and polymetallic veins (Figure 32 b.). The porphyritic diorite intrudes into the overlying porphyritic basaltic andesite (Figure 17 d.) and contacts between the two lithological units were widely observed (Figure 17 c.). The porphyritic diorite intrusion is extensive (~1,5 km in diameter) and it has been subjected to advanced argillic and intermediate argillic alteration on the hills surrounding the creek (Figure 17 b. and f. and Figure 38 a.) and to sericitic and chlorite-sericitic alteration in the creek near the major fault. The porphyritic diorite was found to have been subjected to much stronger alteration than the overlying porphyritic basaltic andesite, most likely due to the more permeable nature of the intrusive rock (Figure 17 f.). The different alteration zones will be discussed in chapter 4.5 in detail.

Petrographic description

The porphyritic diorite was characterized by abundant plagioclase feldspar glomerocrysts (Figure 18 a. and b.) and very sparse quartz glomerocrysts (Figure 18 a., b., e., and f.). Euhedral and subhedral phenocrysts of clinopyroxene were found in most of the porphyritic diorite samples. The amphibole phenocrysts could be distinguished from the sparse clinopyroxene phenocrysts through their typical bipyramid crystal shape, very low degree of extinction, common twinning, low relief, and stronger tendency to alter to chlorite.

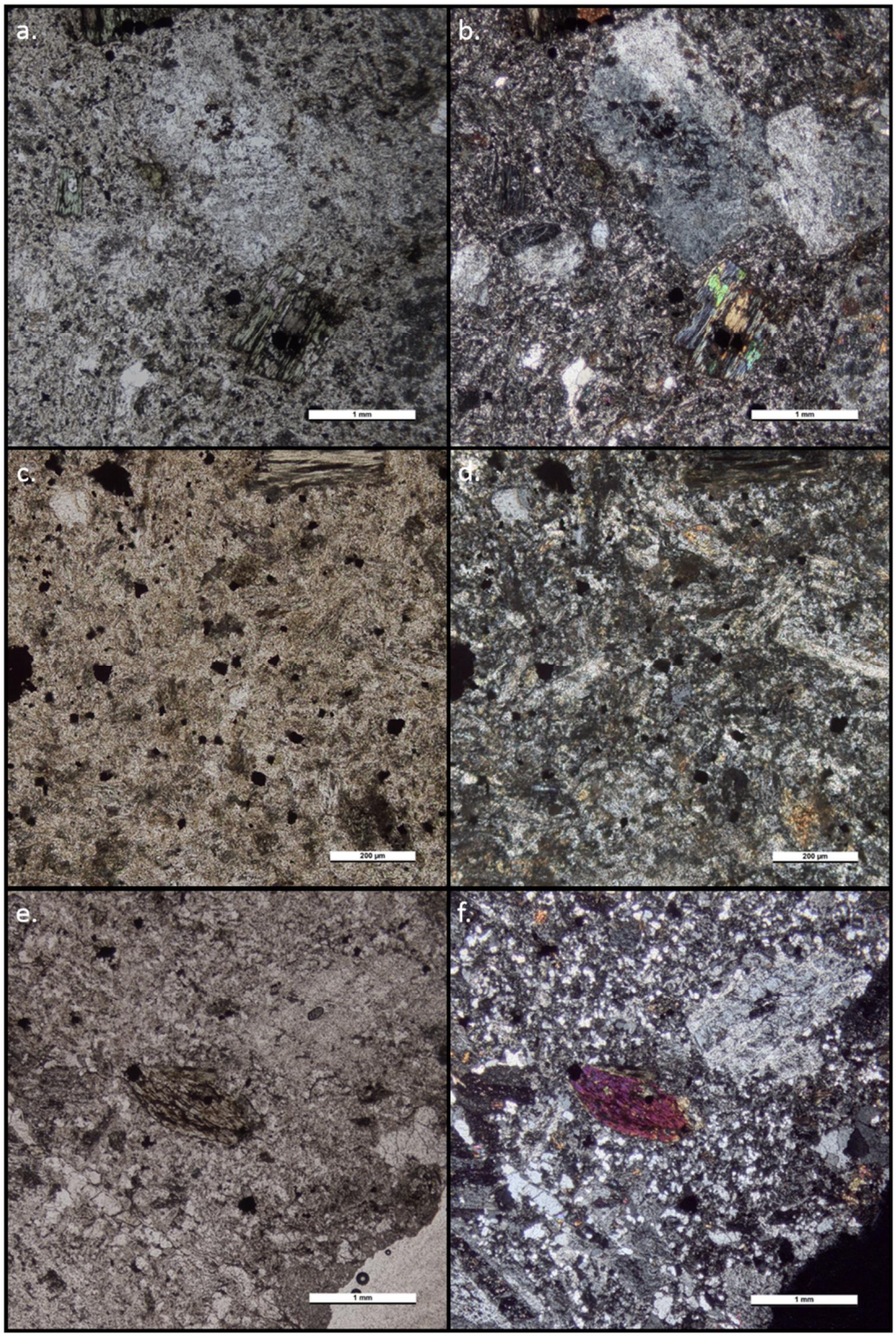

Figure 18: Porphyritic diorite thin-section microphotographs taken in transmitted light. Abbreviations explained at the end of this caption: **a.)** Typical porphyritic diorite with very fine-grained, altered groundmass with large plagioclase phenocrysts. The green phenocryst below the large plagioclase phenocryst was altered to epidote in the centre, while altered to iron-rich chlorite on the outside. The primary Ca-rich amphibole in the centre has been altered to epidote, while the outer primary biotite has been altered to chlorite. Thin section PES011231 (ppl). **b.)** Thin section PES011231 (xpl). **c.)** Typical porphyritic diorite groundmass with fine-grained plagioclase, opaque minerals (magnetite and pyrite), chlorite, and illite/smectite. Thin section PES011231 (ppl). **d.)** Thin section PES011231 (xpl). **e.)** Amphibole phenocryst in groundmass that consists of fine-grained recrystallized quartz and feldspars. Thin section PES011288 (ppl). **f.)** Thin section PES011288 (xpl). (ppl = plane-polarized light, xpl = cross-polarized light)

(Figure 39 c. and d.). Chlorite pseudomorphs altered from biotite were abundant in both the porphyritic diorite and porphyritic granodiorite samples (Figure 18 a. and b., Figure 39 a. and b.).

An interesting, common observation was anhedral epidote engulfed in chlorite clearly replacing biotite (Figure 18 a. and b., Figure 39 e. and f.). It is likely that the epidote in the centre has replaced Ca-rich amphibole, which was surrounded by biotite before it was altered to chlorite (Figure 39 e. and f.). This would be a primary magmatic feature, in which the hydrous amphibole mineral is surrounded by hydrous biotite due to maturing of the magma over time. The crystallization of hydrous minerals such as amphiboles and biotite would suggest that the magma from which the porphyritic diorite crystallized was well hydrated throughout its evolution, which is a positive indication for the formation of a possible PCD.

4.1.2. Porphyritic granodiorite

Field observations:

The western, lower parts of the prospect are characterized by a porphyritic granodiorite intrusion (Figure 28). The porphyritic granodiorite hosts rather infrequent but large (up to 1.0 cm) potassium feldspar phenocrysts (Figure 19 a. and b. and Figure 20 a.), in addition to frequent plagioclase feldspar phenocrysts. Occasional biotite phenocrysts partially or completely altered to chlorite were observed, as well as mafic clusters altered to chlorite and epidote (Figure 19 b.). Outcrops were found to be generally regularly fractured (Figure 19 c.). The overlying porphyritic basaltic andesite units are intruded by subhorizontal aplitic dikes (Figure 19 d.), which most likely originate from late felsic melts of the porphyritic granodiorite intrusion. Some parts of the porphyritic granodiorite host rounded clasts of porphyritic basaltic andesite (Figure 19 e.), which were most likely extracted from

Figure 19: Porphyritic granodiorite field photographs: **a.)** Weathered surface of porphyritic granodiorite with potassium feldspar phenocrysts at the scratcher's tip and in the bottom right corner. Field observation RONJG019. **b.)** Fresh surface of porphyritic granodiorite with an elongated potassium feldspar phenocryst in the bottom of the image, near the scratcher's tip. Abundant plagioclase feldspar phenocrysts can be seen, in addition to chlorite and epidote alteration. Field observation RONJG082. **c.)** Outcrop of regularly fractured porphyritic granodiorite in the creek with rounded surfaces due to weathering. Field observation RONJG017. **d.)** Subhorizontal aplitic dike crosscutting the overlying basaltic andesite. Field observation RONJG009. **e.)** Rounded basaltic andesite xenoliths in porphyritic granodiorite. Field observation RONJG082. **f.)** Intensely silicified and sericitized porphyritic granodiorite near the major fault, in which relict plagioclase phenocrysts can still be seen. Field observation RONJG016.

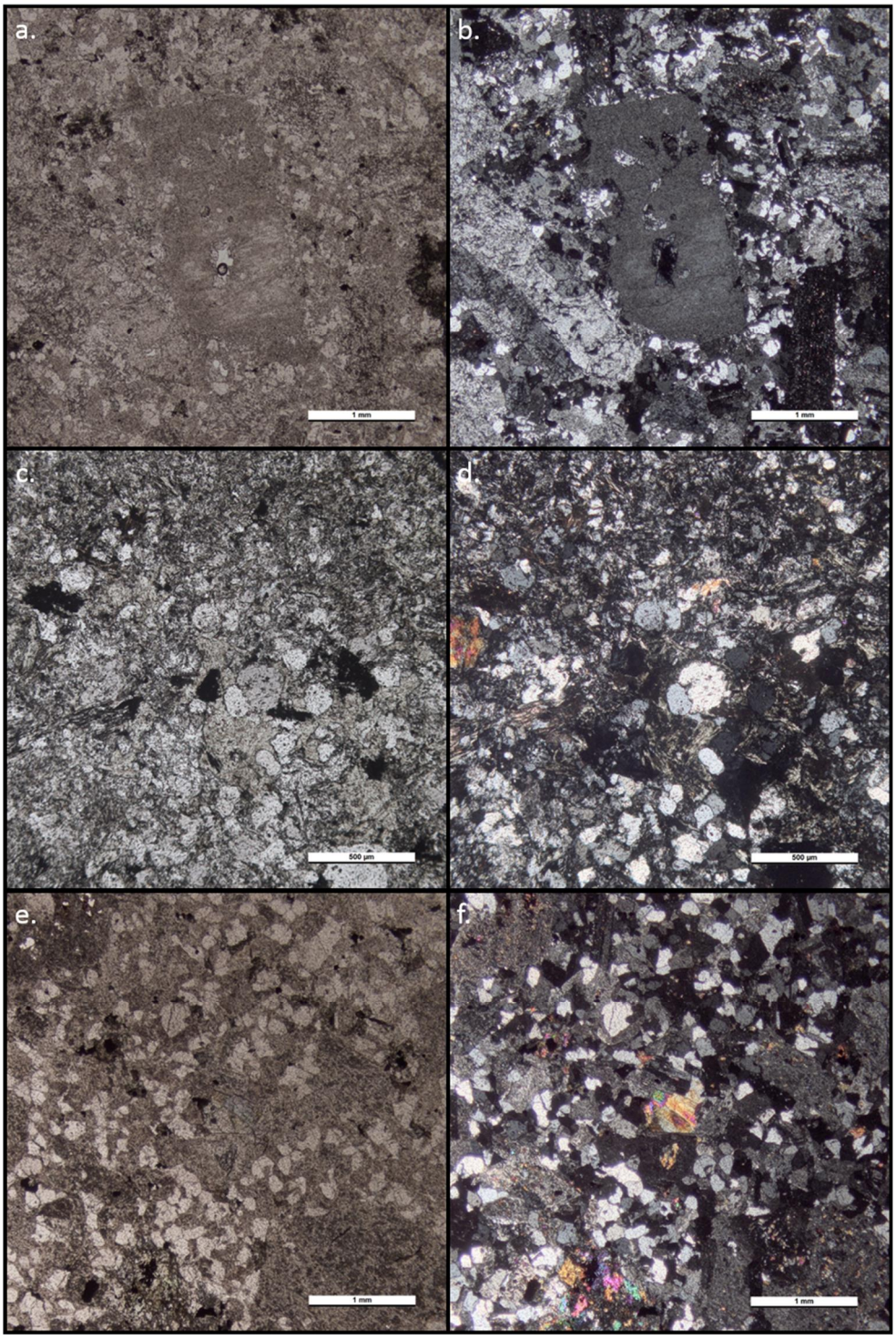

Figure 20: Porphyritic granodiorite thin section microphotographs taken in transmitted light: **a.)** Porphyritic granodiorite with large euhedral potassium feldspar phenocrysts and altered plagioclase phenocrysts. Thin section PES011263 (ppl). **b.)** Thin section PES011263 (xpl). **c.)** The groundmass consists of recrystallized quartz, feldspars, chlorite, and epidote. Thin section PES011248 (ppl). **d.)** Thin section PES011248 (xpl). **e.)** Medium sized plagioclase phenocrysts in a groundmass consisting of recrystallized quartz, plagioclase, potassium feldspar, and epidote. Thin section PES011266 (ppl). **f.)** Thin section PES011266 (xpl).

the volcanic sequences as the intrusion ascended through the crust. The porphyritic granodiorite is intruded by infrequent diorite and quartz-eye-rich diorite dikes, which generally run perpendicular to the major fault structure.

Petrographic description

The porphyritic granodiorite samples were characterized by generally large (2.0 mm) potassium feldspar phenocrysts that were relatively unaltered compared to the plagioclase feldspar phenocrysts present in the same samples (Figure 20 a. and b.). The potassium feldspar phenocrysts were formed later than the plagioclase feldspar phenocrysts, which is evident from the many quartz and plagioclase feldspar inclusions in the potassium feldspar phenocrysts (Figure 20 a.). Myrmekite texture could be observed in some of the porphyritic granodiorite samples. Primary magmatic biotite was observable in one porphyritic granodiorite sample while chlorite pseudomorphs altered from biotite were abundant. Clinopyroxene was commonly observed in aplitic dikes.

4.1.3. Basaltic andesite

Field observations

The textures of the basaltic andesites observed in the field differed quite substantially: The basaltic andesite was generally fine grained (Figure 21 d.) or crystalline and hosted abundant magnetite veinlets (Figure 34 e.) on the northern hill and the lower parts of the southern hill, whereas the texture of the basaltic andesite was more porphyritic at the top of the southern hill and in the centre of the creek. Apart from the textures of the fine-grained and porphyritic basaltic andesite, textures such as trachytic (Figure 21 a.) and amygdular basaltic andesite (Figure 21 b.) also occurred.

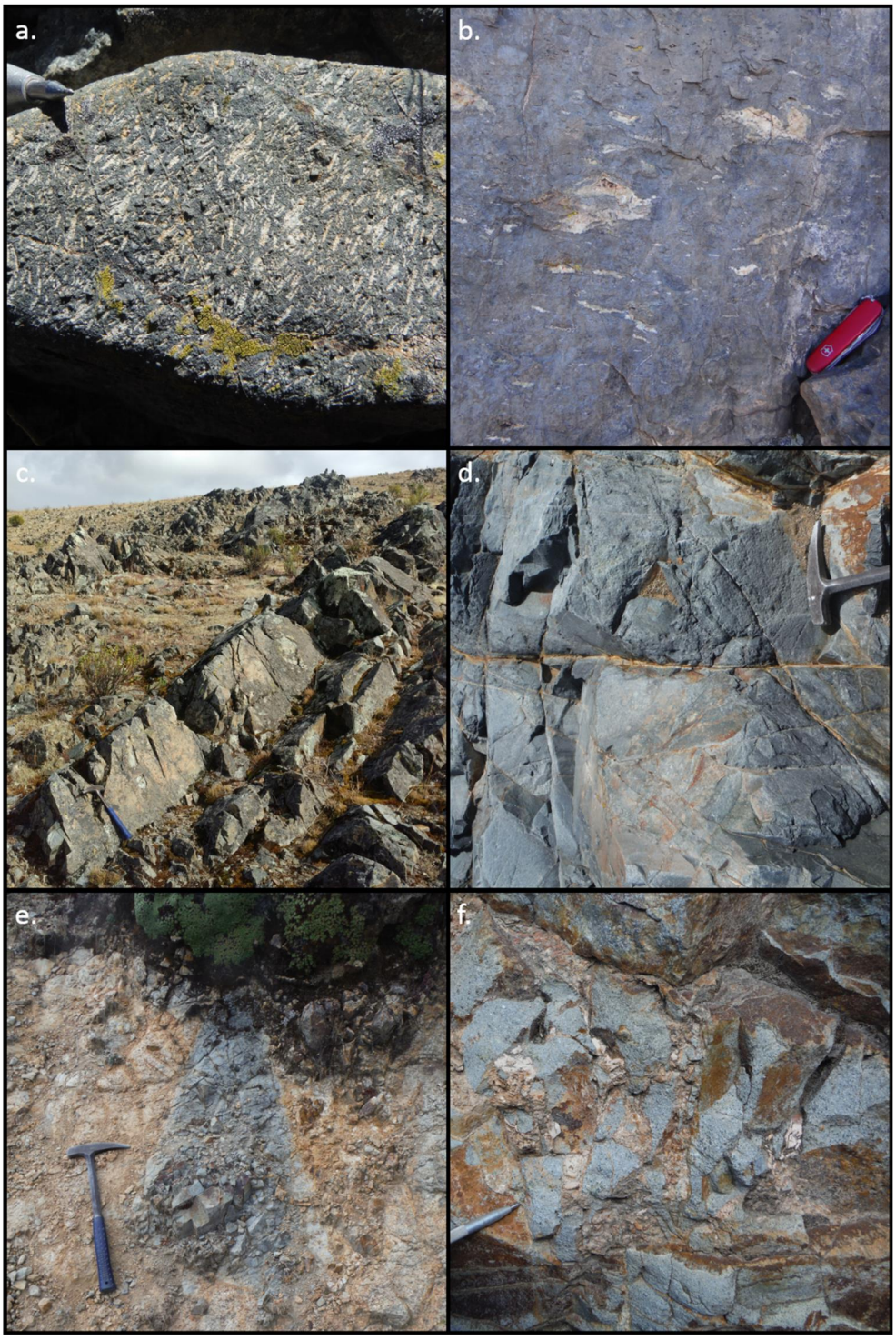

Figure 21: Basaltic andesite field photographs: **a.)** Trachytic basaltic andesite with flow-foliated, elongated plagioclase feldspar phenocrysts. Field observation RONJG146. **b.)** Amygdular basaltic andesite with secondary quartz infilling lenticular vesicles. Field observation RONJG144. **c.)** Gently dipping bedding in porphyritic basaltic andesite outcrop. Field observation RONJG111. **d.)** Fine-grained equigranular basaltic andesite in creek. Field observation RONJG090. **e.)** Porphyritic basaltic andesite roof pendants in intermediate argillic-altered porphyritic diorite. The presence of roof pendants indicates that the top of the intrusion is preserved; they have been exposed due to the erosion of the overlying rock. Near field observation RONJG112. **f.)** Porphyritic basaltic andesite with carbonate travertine in fractures. Field observation RONJG087.

The observed basaltic andesite was generally characterized by distinct flow foliation and bedding (Figure 21 c.). Basaltic andesite also occurred as weakly propylitic-altered roof pendants overlying advanced argillic- and intermediate argillic-altered porphyritic diorite along the hills (Figure 21 e. and Figure 17 f.). The basaltic andesite at Ronaldo is most likely related to low-sulfidation epithermal mineralization, as exemplified by carbonate travertines in fractures in basaltic andesite (Figure 21 f.). Carbonate travertines are distal hot spring discharge products and are generally observed in low-sulfidation and intermediate-sulfidation epithermal settings (Sillitoe 2010). The porphyritic basaltic andesite on the southern hill has been intruded by aplitic dikes, which was also observed on the northern hill. The presence of abundant magnetite veinlets observed in extrusive rocks on the northern hill, and to some extent the southern hill, was further evidence that the extrusive rocks are older than the intrusive bodies since the veinlets most likely originated from the underlying intrusive body. Finally, the porphyritic basaltic andesites on the southern hill, which were not evident on the northern hill, were covered by welded ignimbrite.

Petrographic description

The volcanic units were mostly characterized by plagioclase feldspar phenocrysts with an average length of 1.0 mm and commonly displayed crowded texture (Figure 22 a. and b.). The fine-grained groundmass was typically pervasively altered to chlorite, magnetite, and at times also to illite or illite/smectite (Figure 22 c. and d.). In some samples, the chlorite alteration was patchy rather than pervasive. The plagioclase feldspar phenocrysts were variably altered, in some samples more than others (compare Figure 22 b. and e.). Plagioclase feldspar phenocrysts were generally less altered at high elevations. Some basaltic andesite samples had green euhedral to subhedral hexagonal phenocrysts surrounded by disseminated magnetite (Figure 22 f.). They were deduced to be serpentine pseudomorphs of olivine surrounded by magnetite, which form from excess iron being expelled from the olivine crystal structure as it alters to serpentine. Most extrusive rocks observed at Ronaldo were basaltic andesitic in composition, which explains the relatively common occurrence of these olivine pseudomorphs. Basaltic

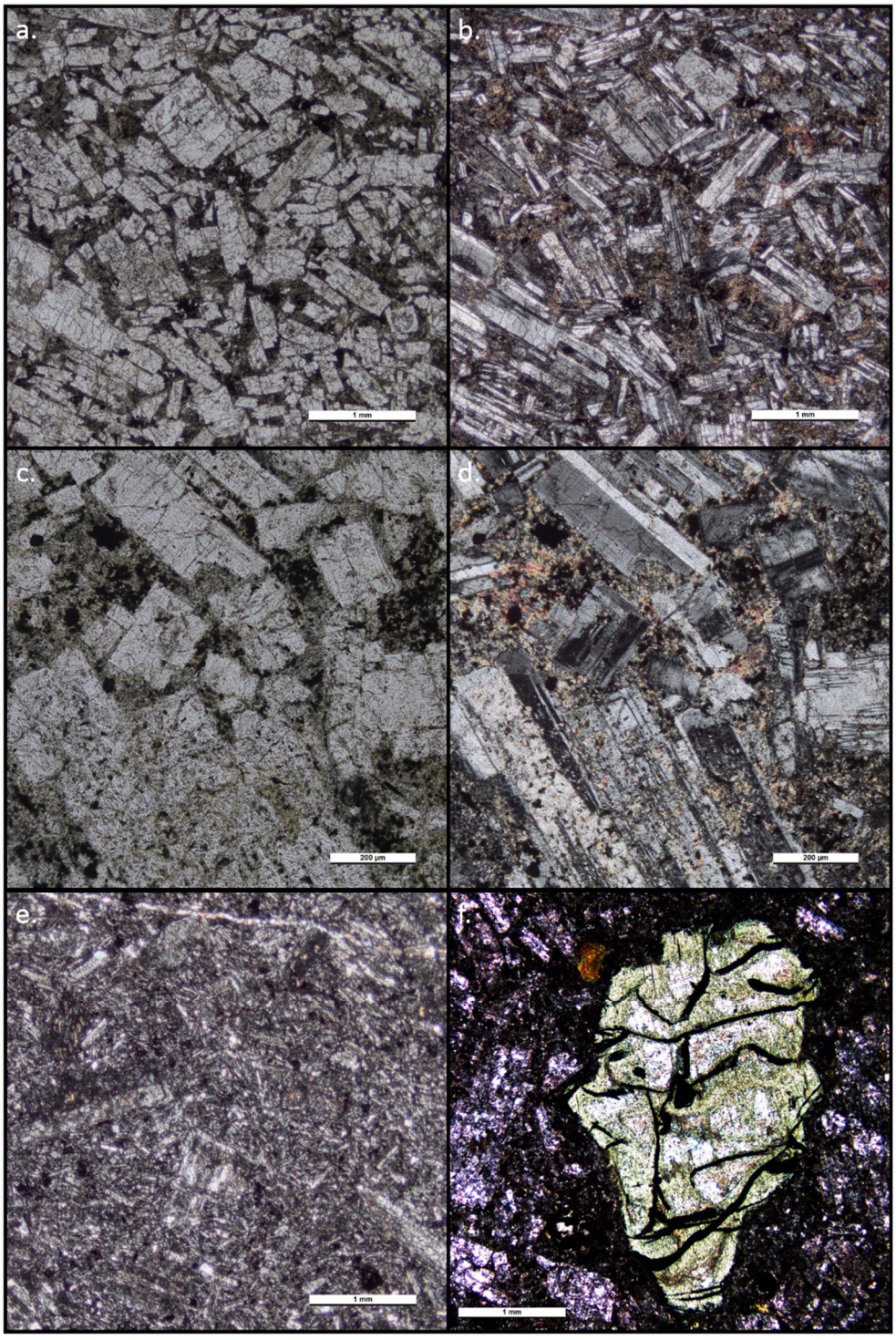

Figure 22: Basaltic andesite thin section microphotographs taken in transmitted light: **a.)** Typical porphyritic basaltic andesite with groundmass altered to chlorite, magnetite, and illite/smectite. Thin section PES011227 (ppl). **b.)** Thin section PES011227 (xpl). **c.)** Close-up of porphyritic basaltic andesite groundmass, showing chlorite, magnetite, and illite/smectite. Thin section PES011227 (ppl). **d.)** Thin section PES011227 (xpl). **e.)** Strongly altered porphyritic basaltic andesite in which large plagioclase phenocrysts can still be seen. Thin section PES011237 (xpl). **f.)** Subhedral olivine pseudomorph replaced by serpentinite and magnetite. Thin section PES013144 (ppl).

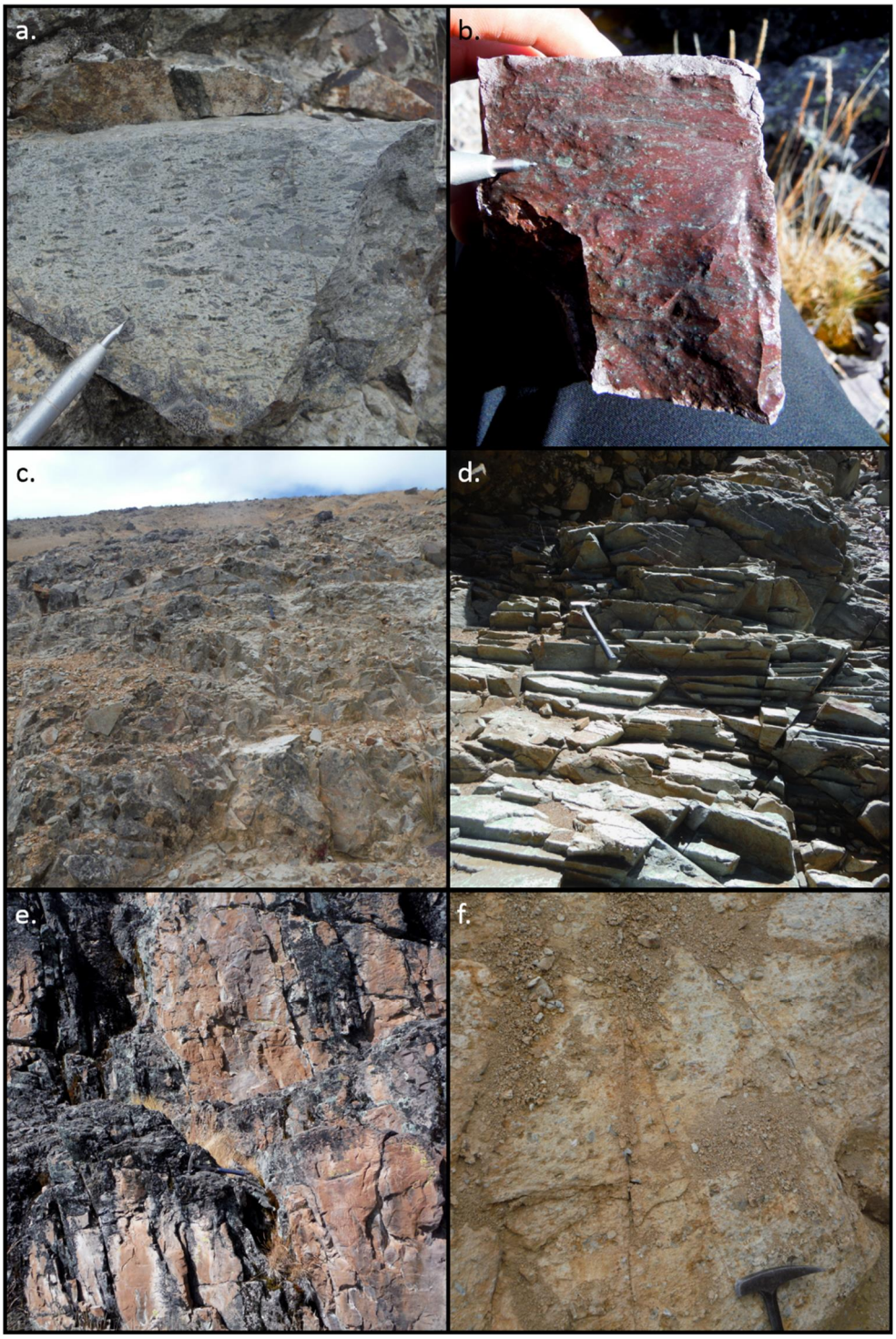

Figure 23: Ignimbrite field photographs: **a.)** Flow-foliated welded ignimbrite with abundant fiamme and elongated lithic clasts. Field observation RONJG123. **b.)** Welded ignimbrite strongly altered to hematite. Field observation RONJG127. **c.)** Contact between the welded ignimbrite (above the hammer head) overlying the porphyritic diorite. Near field observation RONJG113. **d.)** Outcrop of gently dipping flow-foliated welded ignimbrite with abundant fiamme displaying regular fractures. Field observation RONJG084. **e.)** Gently dipping massive welded ignimbrite outcrop. Field observation RONJG127. **f.)** Welded ignimbrite subjected to intermediate argillic alteration. Field observation RONJG114.

andesite samples were found to host clinopyroxene as either sparse, small phenocrysts or as glomerocrysts of subhedral phenocrysts.

4.1.4. Ignimbrite

Field observations

Ignimbrite occurs as massive units (Figure 23 e.) along the highest ridge of the southern hill but were also observed at lower elevations and even once in the creek. These ignimbrites are characterized by welded fiamme and subangular lithic fragments in very fine-grained volcanic glass (Figure 23 a. and Figure 23 f.) in addition to frequent and regular fracturing (Figure 23 d.). Generally, the ignimbrites show very weak or no alteration, but altered segments were also observed: at the southern ridge, the ignimbrite exhibited abundant hematite alteration (Figure 23 b.) due to intense oxidation at near to surface conditions, while units displaying intermediate argillic alteration were also observed (Figure 23 f.). Ignimbrite was found overlying both intrusive and basaltic andesite units (Figure 23 c.).

4.1.5. Magmatic-hydrothermal breccia

Field observations

The creek is characterized by intrusive units and strongly altered magmatic-hydrothermal breccia in between the two intrusive bodies, a relationship that was also observed on the northern hill (Figure 24 b.). The dominant alteration type of the magmatic-hydrothermal breccia is sericitic alteration (Figure 24 a.). Molybdenite-bearing quartz veins and polymetallic veins (Au-Ag-Cu-Pb-Zn) were observed in the porphyritic diorite and the strongly altered magmatic-hydrothermal breccia near the porphyritic diorite (Figure 36).

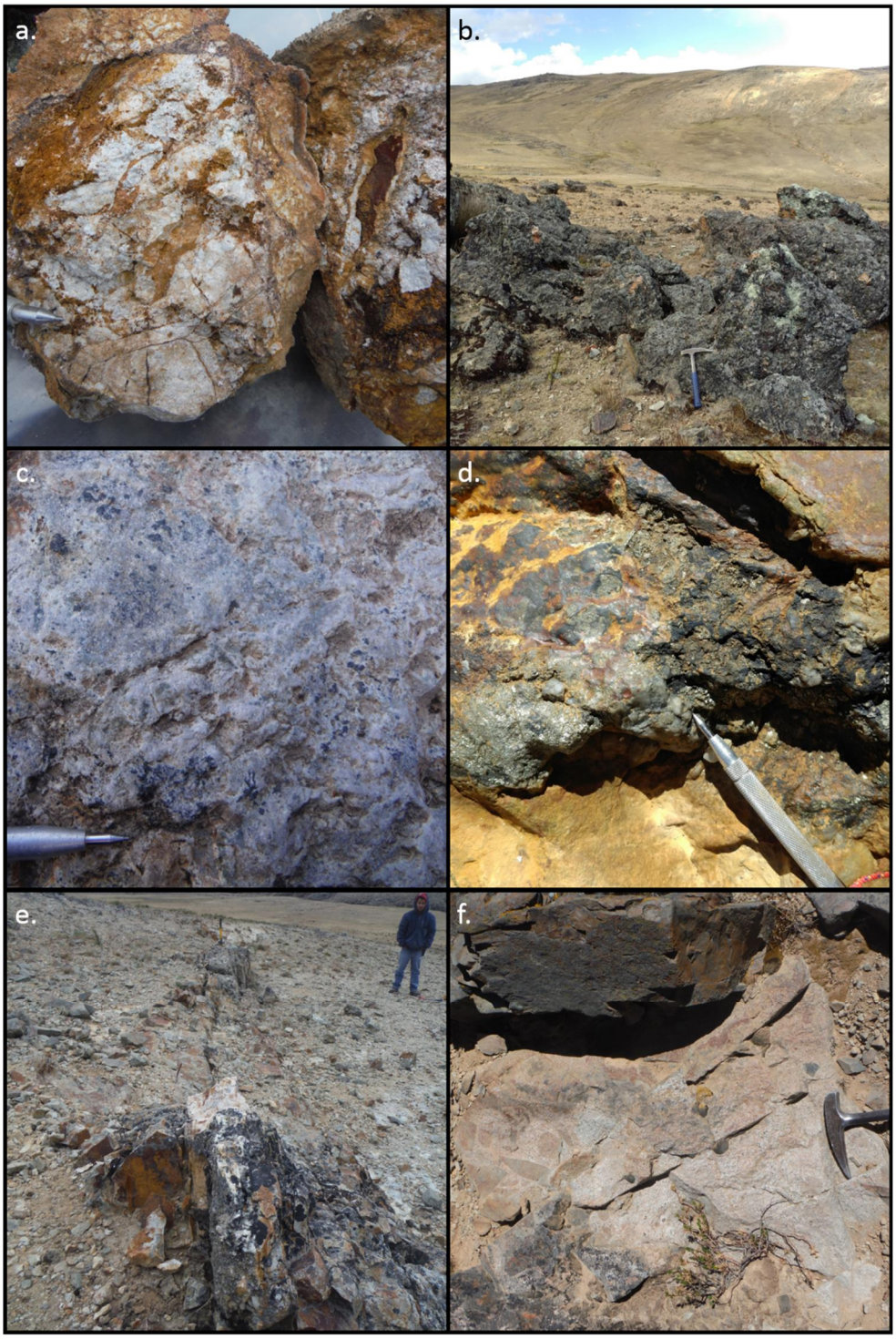

Figure 24: Breccia field photographs: **a.)** Silicified and goethite bearing magmatic-hydrothermal breccia, with abundant oxides that infill the voids. An angular lithic clast can be seen at the very right of the image. Field observation RONJG120. **b.)** Outcrop of magmatic-hydrothermal breccia. Field observation RONJG101. **c.)** Tourmaline patches in irregular magmatic-hydrothermal breccia. Field observation RONJG024. **d.)** Magmatic-hydrothermal breccia with large patches of remnant magnetite and pyrite. Field observation RONJG028. **e.)** Silicified ridge related to magmatic-hydrothermal breccia, displaying jigsaw texture at times. Milky and drusy quartz was observed. Field observation RONJG124. **f.)** Intrusive breccia displaying jigsaw texture. Field observation RONJG140.

The silicified ridges display similarities to magmatic-hydrothermal breccia (jigsaw texture, sericitic alteration) and host different quartz types (milky quartz, drusy quartz) (Figure 24 e.). The degree of silicification differed widely. Generally, the silicified ridges on the northern hill of the prospect are much more pervasively silicified than those on the southern hill.

The cement of the magmatic-hydrothermal breccia consists of muscovite (Figure 24 a.), quartz, tourmaline (Figure 24 c.), pyrite, and isolated magnetite aggregates (Figure 24 d.). This cement is typical of late magmatic-hydrothermal breccias (Sillitoe 2010). There was also an occurrence of rare, low-temperature boron-bearing tourmaline called dumortierite (Figure 38 d.) related to the magmatic-hydrothermal breccia at high elevation. Rather than tourmaline, dumortierite is the principal borosilicate mineral in lithocaps (Sillitoe 2010).

Tourmaline-quartz-pyrite-bearing veins were observed in the porphyritic diorite intrusion, which is spatially closely related to the magmatic-hydrothermal breccia. The most promising PCD-style mineralization – quartz veins hosting molybdenite in the creek – is also believed to be linked to the magmatic-hydrothermal breccia unit although the veins mostly occurred in the porphyritic diorite. Indeed, the most abundant occurrence of magmatic-hydrothermal breccia is related to the porphyritic diorite intrusion, as are the polymetallic veins and molybdenite-bearing quartz veins.

The overprinting of potassic alteration by later sericitic alteration may be observed in the magmatic-hydrothermal breccia through isolated magnetite aggregates that occur as stranded remnants of potassic alteration in sericitic zones (Sillitoe 2010). These isolated magnetite aggregates can occur up to 1 km above the magnetite-cemented potassic parts of the magmatic-hydrothermal breccia (Sillitoe 2010). This suggests some depth to a possible overprinted potassic zone related to porphyry Cu mineralization.

4.2. Geochronology

Four samples were dated by using the U-Pb method on zircons. The samples collected in the field were sent to a commercial laboratory which performed the entire process of dating the zircons. There were two samples from the porphyritic diorite intrusion, one from the porphyritic granodiorite intrusion, and one from the porphyritic basaltic andesite, which was crosscut by aplitic dikes (Figure 26). The estimated magmatic concordia age of the porphyritic diorite intrusion was 19.90±0.54 Ma and 20.00±1.0 Ma, while the porphyritic granodiorite intrusion was dated at 21.29±0.52 Ma (Table 2). The porphyritic basaltic andesite was dated at 21.70±0.54 Ma. The error margin is given as ±2σ. The estimated magmatic concordia ages were determined based on most of the zircons from the samples, except in the basaltic andesite sample, where only the best-fitting samples were selected. Zircon populations were abundant in all the intrusive samples but only sparse in the sample collected from the porphyritic basaltic andesite.

Table 2: Summary of U-Pb geochronology results.

Observation	Sample	Rock type	Age (Ma)
RONJG008	PES011231	Porphyritic diorite	19.90 ± 0.54
RONJG009	PES011233	Porphyritic basaltic andesite*	21.70 ± 0.54
RONJG017	PES011241	Porphyritic granodiorite	21.29 ± 0.52
RONJG028	PES011270	Porphyritic diorite	20.00 ± 1.0

* = zircons most likely from the porphyritic granodiorite

The age of the porphyritic basaltic andesite sample (21.70±0.54 Ma) correlated much better with magmatic activity during the early Miocene than with effusive activity during the late Eocene-Oligocene. The porphyritic basaltic andesite was initially mapped as a porphyritic granodiorite and was only therefore included in the geochronological analysis. Since only one coherent population of zircon ages occurred in the sample (Figure 26 d.), it is not plausible that the zircons originate from the aplitic dike

crosscutting the porphyritic basaltic andesite sample since zircons from the extrusive host rock would create their own distinct population along the concordia line. It is possible that the sample was taken from a more mafic part of the intrusive sequence, although the sample does fit perfectly within the unaltered basaltic andesite population in the whole-rock geochemical assay, so this seems unlikely. Therefore, the most likely source of the confusion was a sampling error, and it is possible that the sample for whole-rock geochemical analysis was taken from the porphyritic basaltic andesite, whereas the sample for the geochronological analysis was taken from the porphyritic granodiorite. The sample will be henceforth considered to represent porphyritic granodiorite (Table 2).

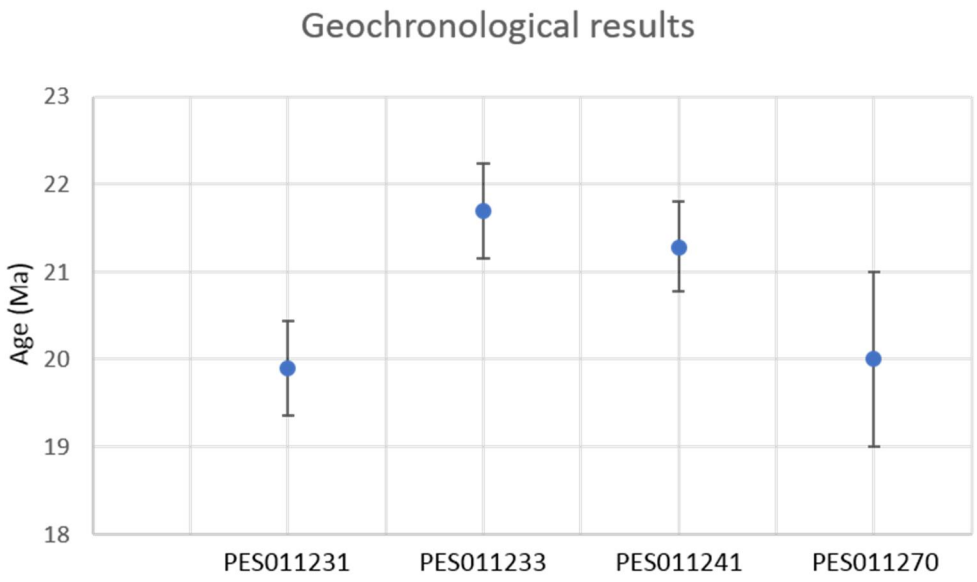

Figure 25: Dating by U-Pb method on zircon results from intrusive units at Ronaldo, results are displayed in Table 2. Error bars are given as ±2σ.

The porphyritic granodiorite intrusion (samples PES011233 and PES011241) is older than the porphyritic diorite intrusion (samples PES011231 and PES011270). When the average age of each sample was considered as their true age, the 1.79 Ma age difference suggests that the two intrusions were emplaced close in time but that they were formed during different magmatic events, possibly even originating from the same parental magma. The error margins of sample PES011270 overlap with those of sample

PES011241, so it is not completely certain that they did not form during the same intrusive event. The error margin of sample PES011270 is rather wide, and its average age correlates very well with sample PES011231. Sample PES011231 clearly belongs to a different age generation than the granodiorite samples, which strongly suggests that the initial observation of the presence of two different intrusive units is very likely.

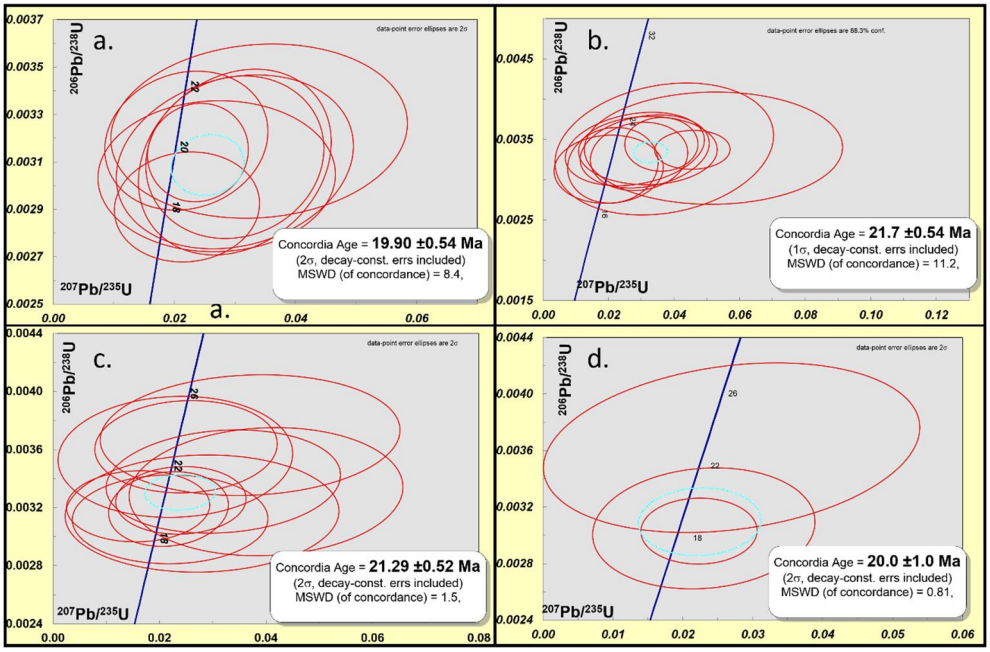

Figure 26: Geochronological results: a.) Porphyritic diorite (PES011231), b.) porphyritic basaltic andesite (PES011233), c.) porphyritic granodiorite (PES011241), and d.) porphyritic diorite (PES011270). The results are shown as Wetherill concordia plots and as a rank order plot of Th-corrected 206 Pb/ 238 U ages.

With an age of 20.00±1.0 Ma, sample PES011270, which is a porphyritic diorite, showed at least four anomalously old zircon ages (e.g. $^{206}Pb/^{238}U$ age 409.0 Ma and $^{207}Pb/^{235}U$ age 571 Ma and $^{206}Pb/^{238}U$ age 62.9 Ma and $^{207}Pb/^{235}U$ age 370 Ma), which may be evidence of crustal assimilation of Middle Paleozoic and even some Lower Cenozoic wall rocks. The laboratory that conducted the analyses deemed seven out of ten samples unrepresentative and only used the three remaining samples to derive the age of the rock sample (Figure 26 d.), which explains why the error margins are much wider than for other samples (Figure 25).

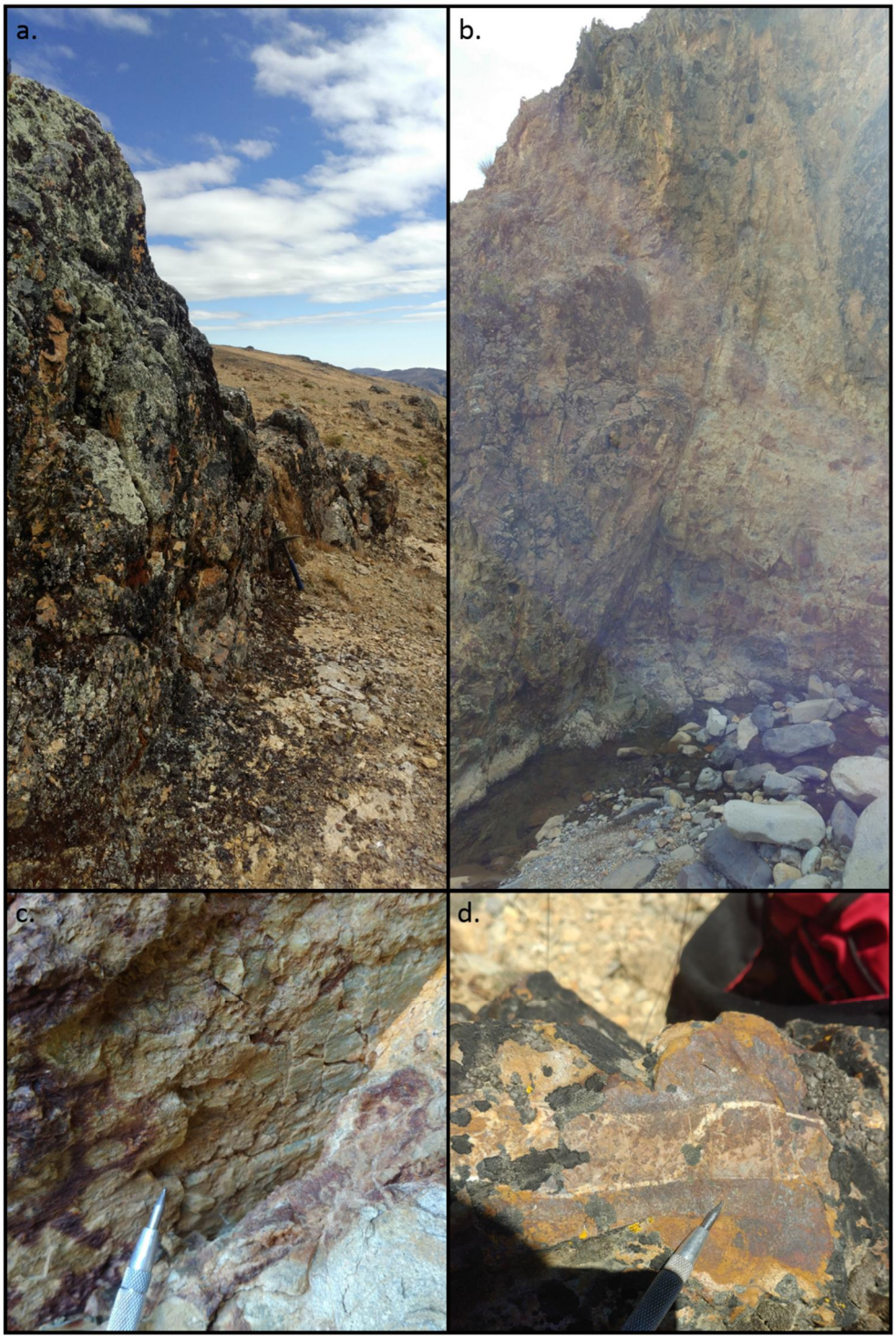

Figure 27: Structural field observation: **a.)** Large silicified ridge oriented subparallel to the major fault, with abundant drusy quartz infilling voids. Field observation RONJG122. **b.)** Sinistral fault oriented parallel to the creek crosscutting polymictic igneous breccia. Field observation RONJG034. **c.)** Same sinistral fault displaying slickenside surface. Field observation RONJG034. **d.)** Sinistral milky quartz vein formed in and around an older quartz vein. Vein hosted in magmatic-hydrothermal breccia. Field observation RONJG067.

4.3. Structural geology

The creek at Ronaldo (oriented ENE-WSW) coincides with a major structure: a sinistral fault transecting the entire prospect (Figure 27 b., c., and d.). This major fault also corresponds to a regional lineament of faults, namely the Abancay Deflection (Marocco 1978). Nearly all sulfide mineralization observed at the prospect was closely related to this major sinistral fault. The polymetallic veins are hosted in fractures with drusy quartz directly intruding along the fault. The BMQ vein is spatially related to the major fault but does not seem to be directly related to it. In contrast to other mineralization, the silicified ridges hosting Ag and Au mineralization generally run parallel to the major fault at a distance.

Sharp contacts between advanced or intermediate argillic altered rock and propylitic-altered or fresh porphyritic basaltic andesites (Figure 17 f. and Figure 21 e.) suggest that there is significant structural and lithological control to the alteration. This control is best exemplified by the sericitic alteration mostly confined to the silicified ridges, magmatic-hydrothermal breccia, and the major fault (Figure 37) or by the advanced and intermediate argillic alteration mostly confined to the porphyritic diorite intrusion. Minor faults perpendicular to the major sinistral fault are found in the creek. There are diorite and quartz-eye-rich diorite dikes crosscutting the main intrusive units in the creek and oriented similarly as the minor perpendicular faults.

The dominant, advanced argillic- and intermediate argillic-altered porphyritic diorite is crosscut by steeply dipping (avg. 77°) silicified ridges oriented subparallel to the major fault with drusy quartz veinlets hosting epithermal silver and gold mineralization (Figure 27 a.). The silicified ridges are 30 to 250 cm wide structures (Figure 27 a.) and can reach lengths of over 200 metres, averaging at over 100 metres. Silicified ridges are abundant on both the northern and southern hill. The silicified ridges are oriented so that their roots most likely join with the major fault at depth, which is most likely the main fluid conduit responsible for the formation of the advanced argillic lithocap. The silicified ridges that were observed in elevated parts of the prospect (Figure 27 a.) are interpreted in this study as being the steeply dipping, deep root zone of a lithocap, which is a structurally and lithologically confined part of lithocap.

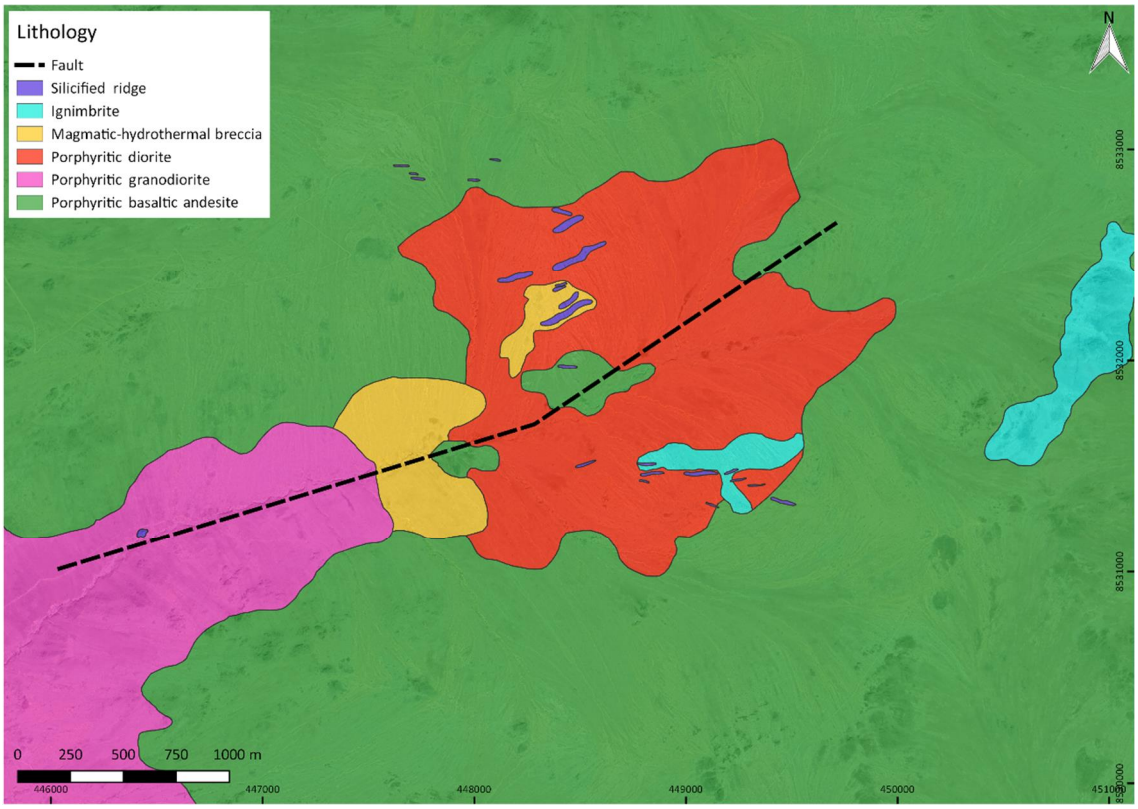

Figure 28: Lithological and structural map of the Ronaldo prospect. The base map can be clearly seen in Figure 5.

4.4. Vein analysis

Veins were found throughout the whole prospect, both in the creek and on the hills surrounding it. Different kinds of veins were observed relating to either the porphyry or the epithermal environments. Out of the 18 polished thin sections of veins, two hosted intermediate-sulfidation mineralization, seven hosted low-sulfidation mineralization, three were barren drusy quartz veins, and six were possibly PCD related. The ore mineralogy and paragenesis are described below.

4.4.1. Low-sulfidation epithermal veins

Field observations

The intrusive rocks are crosscut at high elevations by young, steeply dipping silicified ridges with low-sulfidation epithermal-style drusy quartz veins, some of which host abundant Ag and Au mineralization (Table 1). No silicified ridges were observed crosscutting extrusive units. It is possible that crosscutting of extrusive rocks by silicified ridges was not observed because of strong advanced argillic and intermediate argillic alteration around the silicified ridges, making the lithological units hard to recognize. It would be peculiar if the silicified ridges did not crosscut the extrusive units because the extrusive rocks are older than the intrusive units. It is possible that the intrusive rocks were simply more permeable and that therefor the silicified ridges rather crosscut them than the volcanic units. In addition, there are extrusive rocks close to silicified ridges showing very weak alteration, while the underlying intrusive rock proximal to the silicified ridges has been subjected to pervasive argillic or sericitic alteration. This feature of intense alteration sandwiched between little-altered volcanic rocks may be explained by lateral fluid flow controlled by permeability variations, which is typical of low-sulfidation epithermal deposits (White et al. 1995).

The epithermal mineralization related to the silicified ridges is assigned to a low-sulfidation type due to strong textural evidence including crustiform banding (Figure 29 a.), cavity-filling veins (Figure 29 f.), banded quartz-chalcedony veins (Figure 29 c.), druse-lined cavities (Figure 29 b.), lattice-textured bladed calcite replaced by quartz (Figure 29 d. and Figure 31 e.), and botryoidal silica (Figure 29 e.). All previously listed textures are diagnostic of low-temperature, low-sulfidation mineralization. Common Ag and minor Au (high Ag/Au ratio) (Table 3) also support the low-sulfidation epithermal hypothesis whereas the common occurrence of sphalerite and galena in the silicified ridges rules out high-sulfidation epithermal mineralization, for it is very rare that these minerals occur in this mineralization type (White and Hedenquist 1995).

As mentioned before, the silicified ridges are interpreted in this study as the remnant structurally and lithologically confined part of the lithocap. The silicified ridges crosscut the previous alteration zones, such as the advanced and intermediate argillic alteration. The silicified ridges are a product of rock replacement with well-developed alteration zoning: residual quartz, associated with silicification phasing outward to quartz-kaolinite and smectite (Sillitoe 2010).

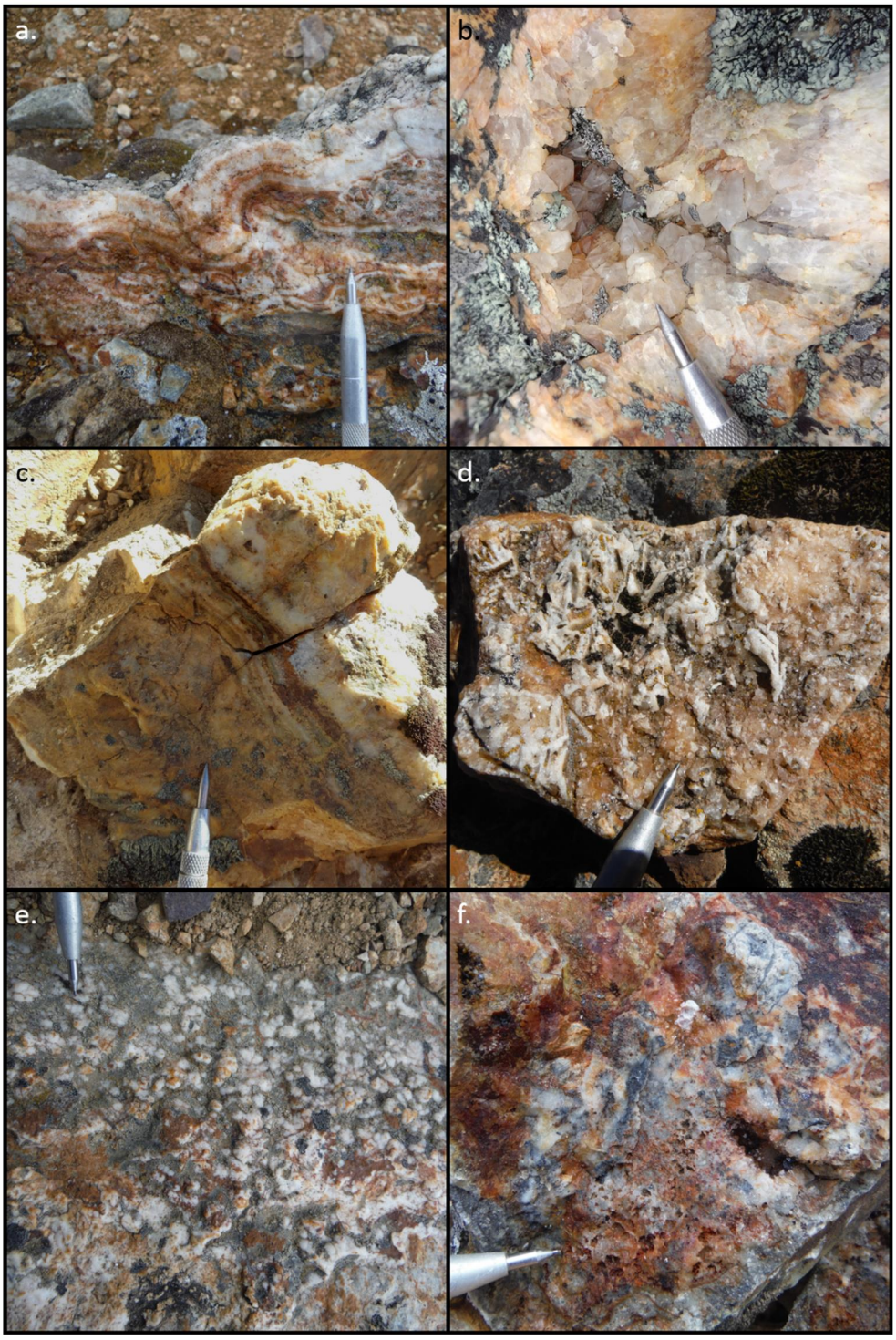

Figure 29: Field photographs of low-sulfidation epithermal mineralization features: **a.)** Crustiform-banded quartz veinlets in a silicified ridge that crosscuts the porphyritic diorite intrusion. Near field observation RONJG103. **b.)** Drusy quartz infilling voids of the silicified ridge. Field observation RONJG097. **c.)** Banded quartz-chalcedony vein related to a silicified ridge which also hosts lattice-textured bladed calcite replaced by quartz. Field observation RONJG050. **d.)** Grab sample displaying lattice-textured bladed calcite replaced by quartz. Field observation RONJG152. **e.)** Fine botryoidal-textured silica. Field observation RONJG094. **f.)** Detail of a 2-metre-wide part of a silicified ridge with local quartz-chalcedony-banding, crustiform-banding textures, and cavity-filling veins. Silver sulfosalts and galena are either related to thin quartz veinlets or infill voids between the quartz crystals. Field observation RONJG097.

Abundant drusy quartz veins generally associated with silicified ridges are observed throughout the prospect, on the elevated northern and southern hill, as well as in the creek related to the mayor fault. Low-sulfidation epithermal mineralization in silicified ridges occurs at high elevations in the system (elevation ~4370 m), while polymetallic veins associated with magmatic-hydrothermal breccia and porphyritic diorite occur in the creek (elevation ~4150 m).

Bonanza low-sulfidation epithermal mineralization (up to 4110 ppm Ag and 16 ppm Au) was observed in the silicified ridges on the northern hill, at a point of jointing of silicified ridges (Table 1), where molybdenite and abundant silver sulfosalts were observed (Figure 29 f.). The silver sulfosalts were confirmed to be pyrargyrite and most likely argentite using reflected light microscopy. Accordingly, many of the samples for whole-rock geochemical analysis collected from silicified ridges hosted elevated levels of Ag and Au and some also of Mo and Pb. Translucent quartz and milky, fine-grained, banded quartz-chalcedony with mineralization were also observed (Figure 29 c.).

Petrographic description

Mineral assemblages and textures indicating low-sulfidation epithermal mineralization were found in several polished thin sections: An array of minerals including pyrargyrite, argentite (Figure 30 c. and d.), native gold (Figure 30 f.), sphalerite, galena (Figure 30 e.), and adularia (Figure 31 c. and d.) were present in these veins. The metallic minerals were mostly infilling voids between euhedral quartz crystals (e.g. Figure 30). Replacement of sulfide minerals by hematite could be observed in many thin sections (Figure 30 a. and b., Figure 31 b.). Lattice-textured bladed calcite replaced by quartz was also observed with a microscope (Figure 31 e.). The replaced calcite had retained its hexagonal shape, and the elongated bladed texture could be observed as quartz with abundant fluid inclusions after replacement. Each blade consisted of a series of parallel seams separated by quartz crystals.

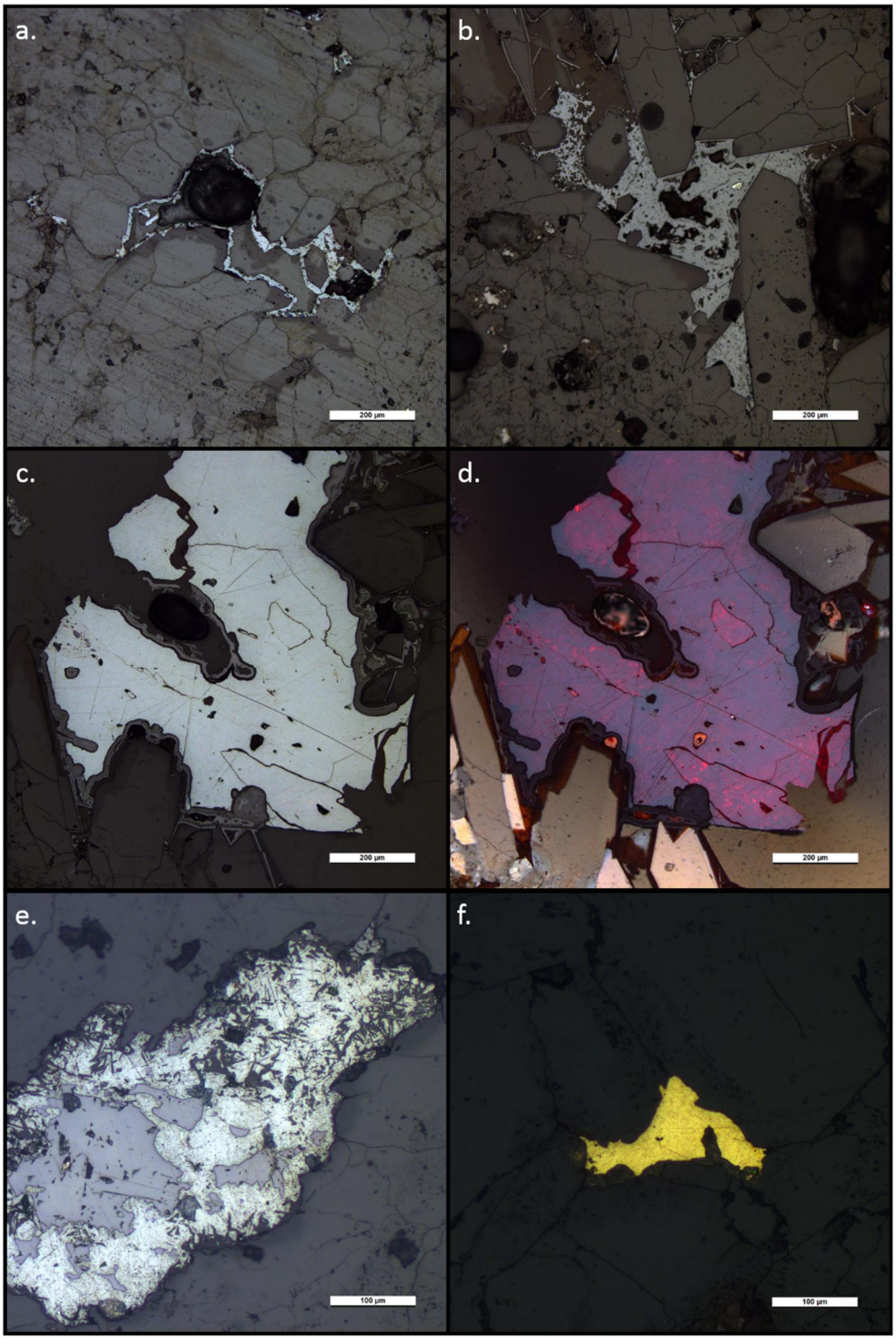

Figure 30: Low-sulfidation epithermal mineralization; microphotographs taken in plain-polarized reflected light unless otherwise mentioned: **a.)** Mineralization altered to hematite infilling empty voids. Thin section D21-008. **b.)** Anhedral phenocryst of galena surrounded by hematite. Thin section D21-013. **c.)** Pyrargyrite altered to argentite at rims. Thin section D21-013. **d.)** Typical internal reflections of pyrargyrite visible in cross-polarized reflected light. Thin section D21-013. **e.)** Sphalerite surrounded by anhedral galena. Thin section D21-013. **f.)** Native gold infilling empty voids in between quartz crystals. Thin section D21-016.

Typical vein adularia ($KAlSi_3O_8$) crystals were observed in four samples as euhedral rhombic crystals with patchy twinning and low interference colours in cross-section intergrown with quartz, replacing aluminosilicates (Figure 31 c. and d.). The crystals were very large compared to what is generally observed in epithermal veins (5-50 µm), locally occurring as euhedral crystals up to 200 µm long and generally 100 µm long. The adularia was confined to only certain layers of the quartz vein, which had many different generations of quartz, demonstrating the reopening of the vein multiple times. In some cases (D21-002), the adularia occurred together with illite and was quite damaged and very few rhombic crystals could be seen. The same layer where the adularia and illite occurred had euhedral cubic pyrite crystals, which were commonly brecciated.

Vein adularia forms over a wide range of temperatures, from about 150 to 300°C, indicates neutral pH, good permeability, and is common at shallow to intermediate depths in epithermal systems. Adularia is a hydrothermal variety of orthoclase and is a diagnostic mineral of low-temperature, low-sulfidation epithermal mineralization as it is often associated with boiling fluids, and therefore also with gold in epithermal vein deposits. Increasing of solution pH due to boiling and exsolution of CO_2 promotes stability of adularia over illite, which is a hydrothermal alteration mineral widely observed in intrusive rocks at Ronaldo. Adularia is commonly replaced by illite. The presence of adularia in the quartz veins related to the silicified ridges revealed that there were fluids with increased pH flowing through them at some point. It is important to note that despite this association, all vein samples with adularia at Ronaldo displayed low Au in their whole-rock geochemical assay results. Many of the low-sulfidation epithermal vein samples displayed illite as an alteration mineral, and some even displayed adularia in different parts of the highly stratified quartz vein. From this one can conclude that fluctuations in the pH of the hydrothermal fluid responsible for ore deposition were common.

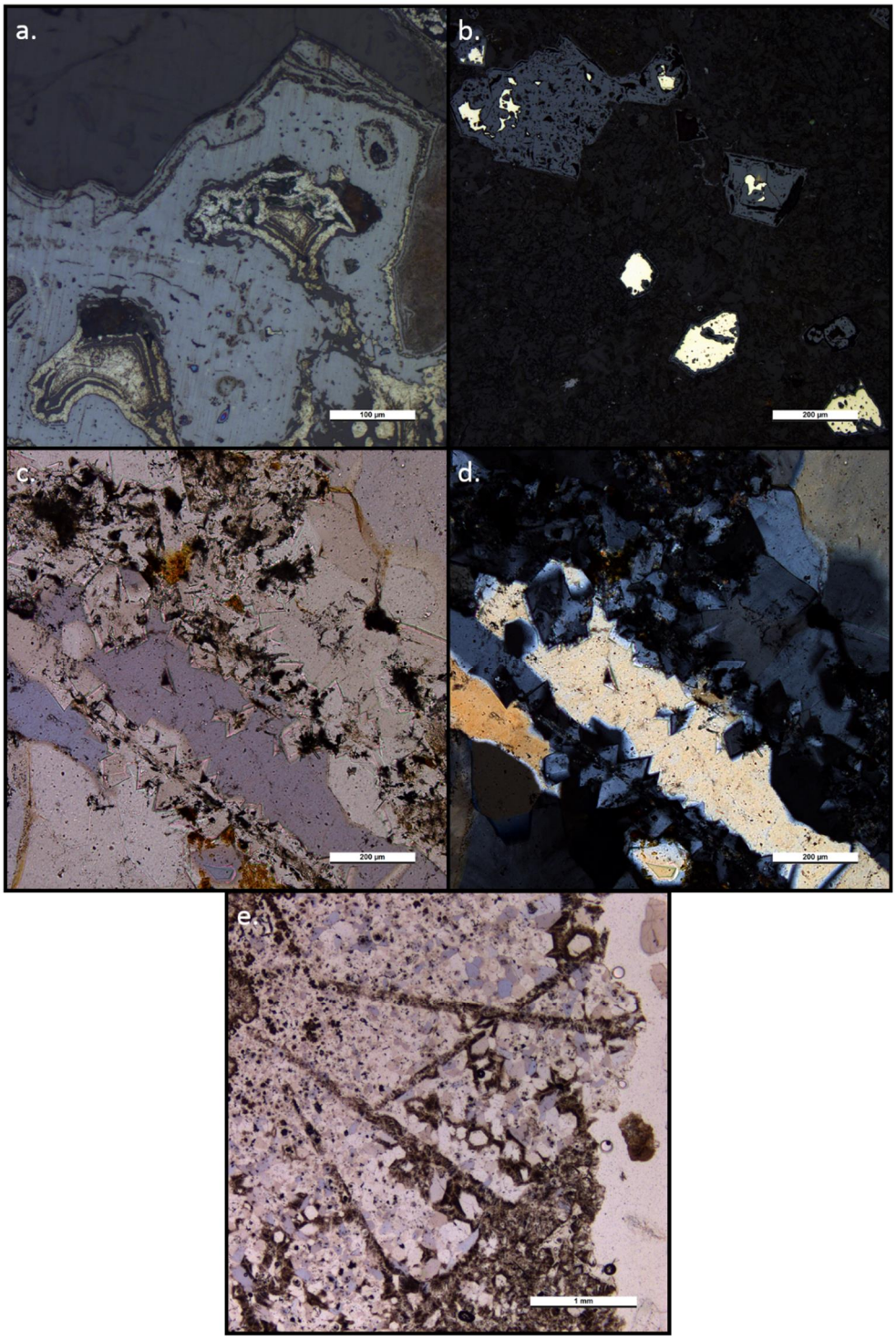

Figure 31: Low-sulfidation epithermal mineralization; microphotographs taken in plain-polarized reflected light unless otherwise mentioned: **a.)** Infill of empty voids by magnetite, hematite, and galena. Thin section D21-016. **b.)** Hematite pseudomorphs replacing euhedral pyrite. Thin section D21-003. **c.)** Rhombic adularia crystals. Thin section PES011246 (transmitted, ppl). **d.)** Thin section PES011246 (transmitted, xpl). **e.)** Lattice-textured bladed calcite replaced by quartz. Thin section PES013123 (transmitted, ppl).

Quartz (SiO_2) was the main mineral component of all veins related to low-sulfidation epithermal mineralization. Large, subparallel to parallel elongated drusy quartz crystals averaging 1.0 cm in length and oriented perpendicular to the vein wall were abundant (Figure 29 b.). The formation of drusy quartz requires relatively slow-changing conditions and open space during crystal growth (Dong et al. 1995). Other quartz crystal textures also existed, such as very fine-grained quartz related to wall rock fragments in the veins, unoriented elongated medium-grained quartz crystals, and fine-grained quartz zones in the reopened quartz veins. The veins were clearly reopened by multiple different hydrothermally active events, which was evident due to the stratified appearance of the quartz veins, which could be seen as many different quartz generations. Coarse grained, drusy euhedral quartz, medium-grained subhedral quartz, and fine-grained anhedral quartz were some of the observed quartz types. Illite tended to occur as fracture filling, patches, or layers that were interlaid with fine-grained quartz. Sulfide, oxide, and metallic mineralization was hosted in quartz, but pyrite was commonly observed in the wall rock (Figure 31 b.).

Botryoidal or colloform texture could be seen in the centre of open-spaced veins, perpendicular to the vein wall, where the spheres were highlighted by the distribution of impurities within the aggregates of silica (Figure 33 d.). The texture is diagnostic of low-temperature epithermal veins because it records the presence of a silica gel precursor. To form the silica gel, the hydrothermal fluid needs to be highly supersaturated with silica, which may occur when a rapidly ascending hydrothermal fluid does not precipitate silica during its ascent (Dong et al. 1995). The botryoidal silica occurred in veins that hosted intermediate-sulfidation epithermal mineral assemblages but closer to the centre of the veins, which may suggest that the veins had been reopened during a later, low-sulfidation epithermal-dominated hydrothermal event. The adularia and the botryoidal silica occurred closer to the centre of the veins, which suggests that the veins were indeed reopened by a later low-sulfidation hydrothermal event.

A common feature of low-sulfidation epithermal veins was the presence of abundant hematite (Fe_2O_3) filling voids and lining fractures, presumably altered from sulfides as can be seen in samples D21-003 and D21-009, where hematite pseudomorphs had

replaced pyrite in the wall rock and thereby preserved the original cubic form of the pyrite crystal (Figure 31 b.). The hematite is characterized by its bluish grey colour, low reflectance, and very strong dark red internal reflections (Figure 30 a. and b.). The diagnostic brownish grey anisotropism usually observed in hematite was masked by the internal reflections. Hematite was also observed in open spaces surrounding galena (Figure 30 b.). The presence of hematite indicates that iron-bearing minerals were oxidized in a higher oxidation state, suggesting oxidation in an environment near the surface, exposed to surface water or the atmosphere.

Sphalerite ((Zn,Fe)S) could be found in some low-sulfidation epithermal quartz veins. It was the same translucent, green-coloured (ppl, in transmitted light) type as in the intermediate-sulfidation epithermal veins (Figure 33 c.). It is a medium grey, poorly reflective anisotropic mineral with yellow-orange internal reflections. The subhedral sphalerite phenocrysts were surrounded by white, quite isotropic anhedral minerals, which were interpreted to be galena (Figure 30 e.). Diagnostic triangular pits were not observed, but the whole-rock geochemical assay results revealed that the Pb content was elevated in the sample, as was the case for other samples with similar mineral assemblages.

In sample D21-016 there were minerals of three shades of grey infilling open spaces (Figure 31 a.). These three minerals were interpreted to be 1) magnetite (low reflectance, dark grey mineral with reddish tint) at the rims of the once empty void, 2) hematite (low reflectance, bluish-grey mineral with strong red internal reflections), and 3) argentiferous galena infilling the final parts of the empty void. The galena had a skeletal texture and was deposited simultaneously with a silicate mineral. The whole-rock geochemical assay results from the sample showed elevated values of Ag, although no silver sulfosalt minerals were observed. The silver may exist in the form of a minor silver sulfide mineral phase or as limited silver in solid solution within the galena structure. It is possible that the whole infill has been incorrectly interpreted and that the empty void is in fact infilled with acanthite and native silver. Electron probe microanalysis (EPMA) is necessary to decide which of these possible interpretations is correct.

Silver sulfosalts were observed infilling open spacing, as had already been recognized from hand samples. The mineral was interpreted to be pyrargyrite (Ag_3SbS_3) due to its blue-grey colour and very strong red internal reflections, which mask the anisotropy (Figure 30 c. and d.). The mineral was also translucent and darkened when exposed to light during microscopical work. The mineral was difficult to distinguish from proustite but was more likely to be pyrargyrite due to the anomalous, highly elevated values of Sb and the presence of galena, quartz, and sphalerite, which are commonly associated with pyrargyrite. It is important to note that the As and Mo values were also significantly elevated in the whole-rock geochemical assay results, and no As or Mo bearing minerals were observed in the D21-013 thin section. It is possible that proustite, arsenopyrite, or molybdenite occur in the sample but were not recognized. Further work using EPMA is required to distinguish between the many blue-grey minerals in the sample. Native gold (Au) was observed in many thin sections (e.g. D21-013, D21-014, and D21-016) as an anhedral, reflective, yellow-gold coloured mineral infilling empty voids in quartz veins (Figure 30 f.).

4.4.2. Intermediate-sulfidation veins

Field observations

Along the major fault in the creek, a large drusy quartz vein (Figure 32 d.) with jigsaw-textured brecciated segments (Figure 32 a. and c.) hosted in magmatic-hydrothermal breccia was observed. This quartz vein hosted intermediate-sulfidation epithermal mineralization, including abundant sphalerite, galena, chalcopyrite, pyrite, and covellite. A drusy quartz vein with intermediate-sulfidation epithermal mineralization related to porphyritic diorite was also observed in the creek (Figure 32). Such polymetallic veins can be defined as either intermediate-sulfidation epithermal or as subepithermal veins. Both vein types host similar metal associations, but their formation environments differ (Sillitoe 2010). Subepithermal veins are fault- and fracture-controlled and form in the propylitic, distal parts of a porphyry Cu system, whereas intermediate-sulfidation veins overlie porphyry stocks alongside the lithocap environment. Defining the polymetallic

veins at Ronaldo was challenging because propylitic alteration was widespread and because the polymetallic veins were related to the major fault but also existed alongside the lithocap

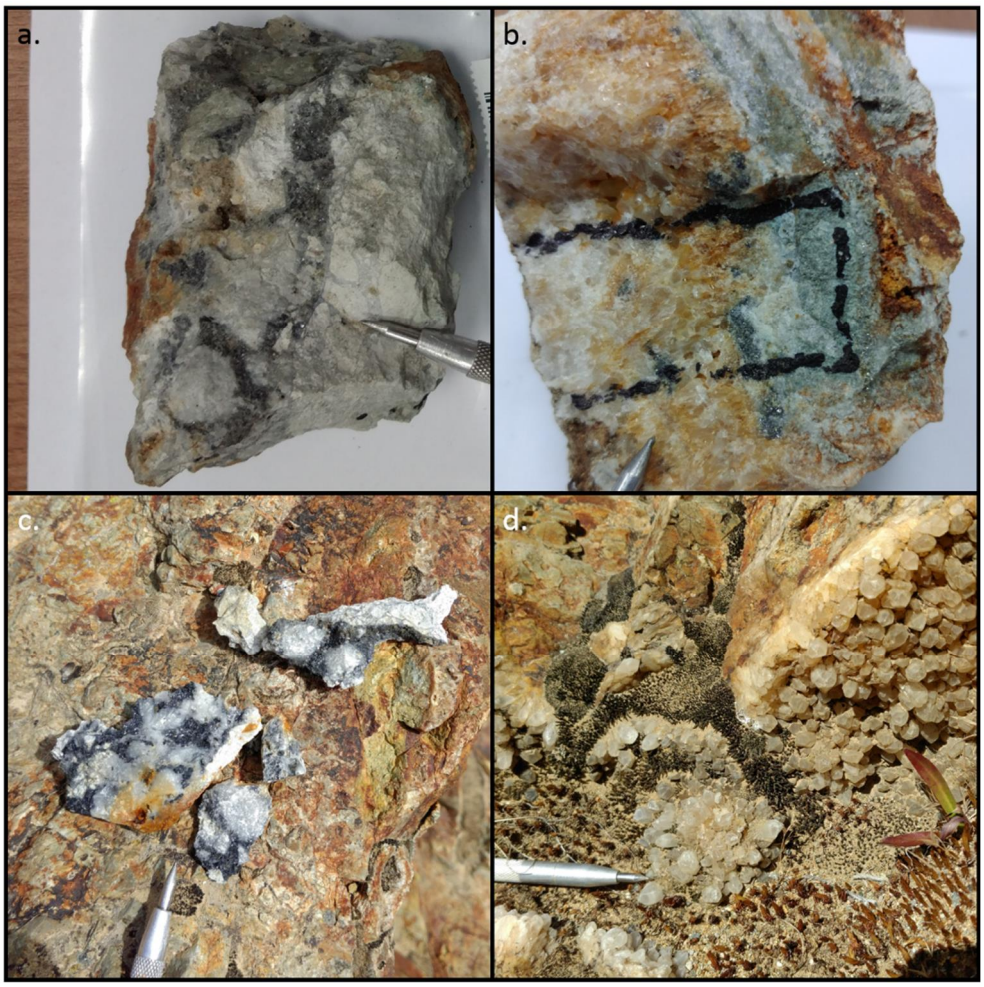

Figure 32: Field photographs of intermediate-sulfidation epithermal mineralization features: **a.)** Jigsaw-textured strongly silicified magmatic-hydrothermal breccia with galena, sphalerite, chalcopyrite, and pyrite mineralization (intermediate-sulfidation epithermal) in matrix. Field observation RONJG033. **b.)** Drusy quartz vein with the same mineralization as in a.). The mineralization is located between the drusy quartz and the fine-grained equigranular quartz zones. At the centre of the vein (in the left-most part of the image) there is a zone of botryoidal texture quartz. Field observation RONJG024. **c.)** Rock chips of the intermediate-sulfidation epithermal mineralization lying on top of the magmatic-hydrothermal breccia where it is hosted. Field observation RONJG033. **d.)** The drusy quartz vein to which the jigsaw-textured intermediate-sulfidation epithermal mineralization is closely related to at field observation point RONJG033.

environment. In addition, deep parts of fault arrays are known to host massive sulfide veins, such as were observed. Thus, it is uncertain if the polymetallic veins represent either intermediate-sulfidation epithermal veins or subepithermal veins. Some

intermediate-sulfidation epithermal deposits have been known to adjoin advanced argillic lithocaps (Sillitoe 2000). The polymetallic veins observed at Ronaldo will be referred to as intermediate-sulfidation epithermal veins in this study.

Petrographic description

Mineral assemblages indicative of intermediate-sulfidation epithermal mineralization were found in thin sections D21-002 and D21-004: sphalerite, galena, pyrite, chalcopyrite and covellite were present in decreasing order (Figure 33 e. and f.). The lack of appreciable amounts of arsenopyrite and pyrrhotite strongly suggests that the mineralization is intermediate-sulfidation epithermal (Sillitoe et al. 2003).

The sphalerite ((Zn,Fe)S) observed in the intermediate-sulfidation epithermal veins has a medium grey colour, is weakly reflective, and is isotropic. It was present as crystals up to 1.0 mm in diameter. The sphalerite crystals were subhedral, translucent, and green in transmitted light. The crystals also displayed yellow-orange internal reflections, which can be used as a quantitative estimative method of estimating that the Fe content of the mineral was ~10% (Awadh 2009), which is quite low: This method was supported by the translucence of the crystals. Fe-poor sphalerite is considered diagnostic of intermediate-sulfidation epithermal mineralization (Giggenbach 1997). The subhedral sphalerite crystals hosted numerous inclusions or blebs of chalcopyrite (“chalcopyrite disease”) and galena. Both occurred mainly as blebs (chalcopyrite 3 µm, galena 40 µm) within the sphalerite crystals (Figure 33 b.). Chalcopyrite disease is a feature typical of unmetamorphosed hydrothermal vein deposits formed at moderate temperatures (200-400°C) and in a geologically brief time (Barton et al. 1987).

Galena (PbS) is a white, relatively reflective, isotropic minerals found throughout the mineralized segments of the thin sections as either anhedral intergrowths in the sphalerite crystals or as massive anhedral crystals filling interspaces of other minerals present. The anhedral crystals were up to 1 mm in diameter, and they were white, moderately reflective, and isotropic. The typical triangular pits diagnostic of galena were found even in the sphalerite intergrowths.

Pyrite (FeS_2), a light yellow, reflective isotropic mineral, was present in the form of euhedral crystals measuring 0.1 mm in diameter. The pyrite formed crystal clusters separate from the other sulfide minerals or appeared as anhedral crystals between the sphalerite crystals (Figure 33 a.). In some parts of the thin sections, one can deduce that the pyrite crystals were subjected to brittle, low temperature deformation on the basis of the cataclastic texture of some of the pyrite crystals.

Chalcopyrite ($CuFeS_2$) is brassy yellow and moderately reflective. It was present in the form of anhedral 0.2 mm crystals. It displayed typical weak, olive-green anisotropy. It also occurred as crystallographically oriented chalcopyrite disease in subhedral sphalerite crystals. Chalcopyrite was the most abundant Cu-bearing mineral at Ronaldo, but it is economically insignificant because it is found in the intermediate-sulfidation epithermal veins.

Covellite (CuS) has an indigo-blue hue, is very weakly reflective, and is anisotropic, displaying orange shade colours. The observed covellite was deposited in a secondary, oxidized form that coats chalcopyrite.

The observations made on the paragenetic relationship between the sulfide minerals are as follows: Subhedral sphalerite hosts inclusions of chalcopyrite and galena. Euhedral pyrite crystals are surrounded by both chalcopyrite and galena. Anhedral pyrite can be seen surrounding subhedral sphalerite, which would suggest that sphalerite formed earlier in the paragenetic sequence. These observations conclude that sphalerite was the first sulfide to form, after which pyrite crystallized. Chalcopyrite and galena were formed afterwards. Their relationship is unclear, but chalcopyrite disease in sphalerite suggests that chalcopyrite crystallized before galena. Nevertheless, chalcopyrite and galena may be cogenetic.

The sulfide minerals occurred in highly stratified quartz veins which have been reopened multiple times, a texture typical at the low temperature end of the epithermal mineralization spectrum, including low- and intermediate-sulfidation epithermal mineralization. The bands of silica were less delicate than seen in the low-sulfidation epithermal mineralized veins, although low-temperature textures such as botryoidal

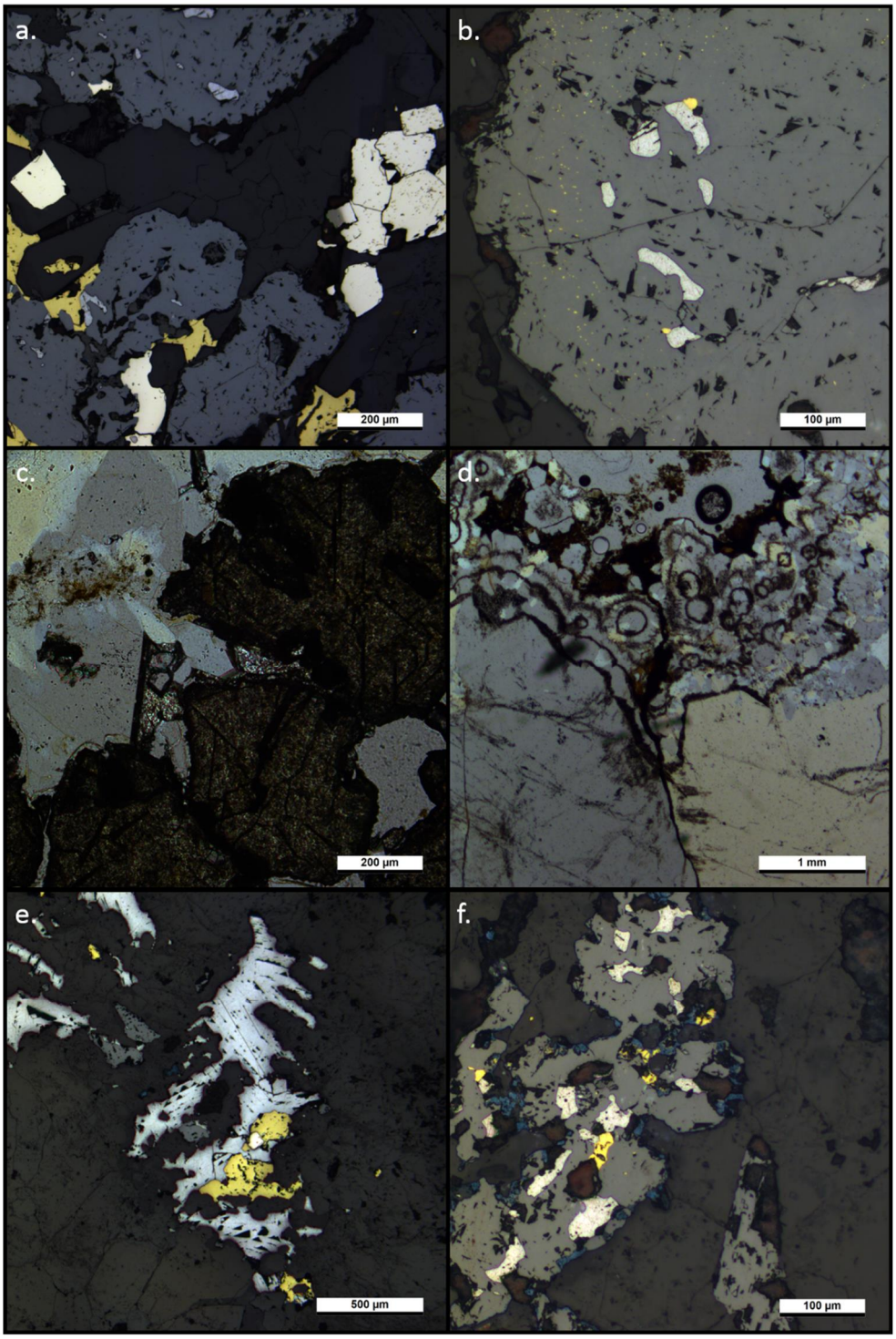

Figure 33: Intermediate-sulfidation epithermal mineralization; microphotographs taken in plain-polarized reflected light unless otherwise mentioned: **a.)** Mineral assemblage of cogenetic sphalerite, galena, chalcopyrite, and pyrite and a separate, later generation of euhedral pyrite. Thin section D21-002. **b.)** Chalcopyrite disease and chalcopyrite and galena intergrowths in sphalerite. Thin section D21-002. **c.)** Green, translucent Fe-poor galena typical of intermediate-sulfidation mineralization; plain-polarized transmitted light. Thin section D21-002. **d.)** Botryoidal or colloform texture in the centre of the open spaced vein: plain-polarized transmitted light. Thin section D21-002. **e.)** Triangular pits in galena, cogenetic chalcopyrite, sphalerite, and pyrite. Thin section D21-004. **f.)** Cogenetic sphalerite, chalcopyrite, and pyrite, chalcopyrite altered to secondary covellite. Thin section D21-004.

silica occurred in the intermediate-sulfidation epithermal veins. Sulfide minerals diagnostic of intermediate-sulfidation epithermal mineralization occurred between the stratified layers of silica. The sulfides occurred in a layer of fine-grained irregular quartz crystals and euhedral adularia crystals and were superimposed by large, euhedral drusy quartz crystals.

4.4.3. PCD-style veins

Field observations

Sparse PCD-style veining was observed in the creek, mostly related to the porphyritic diorite intrusion and neighbouring magmatic-hydrothermal breccia. BMQ veins were observed (Figure 34 b.) in one location, crosscut by drusy quartz epithermal veins.

A sinuous sugary quartz vein with related fractures filled with abundant molybdenite and pyrite mineralization was observed (Figure 34 a.), and straight quartz veins with pyrite centrelines (possible B veins) were also observed (Figure 35 d.). D-type pyrite veins with wide sericite alteration halos (Figure 34 c.) as well as banded magnetite-quartz veins (Figure 34 d.) and magnetite veinlets with albite halos (Figure 34 e.) were also observed.

Magnetite veinlets are often related to A-veins in PCDs and thus suggest a rather shallow emplacement of porphyry stocks (Proffett 2009). The magnetite-bearing veins might be high temperature veins and veinlets related to relatively shallowly sourced PCDs (Seedorf 2005). The presence of magnetite ± quartz veinlets may suggest the proximity of a potassic alteration zone which may be overprinted with sericitic alteration.

While conducting reconnaissance mapping in the area, vein types, width, frequency, and relationships were documented. Apart from the mineralized veins discussed here, an array of other vein types were mapped. All mapped veins are presented in Figure 36.

Figure 34: Field photographs of PCD features: **a.)** Sinuous sugary quartz vein and related fracture filled with molybdenite and pyrite hosted in magmatic-hydrothermal breccia. Field observation RONJG033. **b.)** Banded molybdenite quartz (BMQ) vein with epidote-chlorite-pyrite centreline hosted in basaltic andesite. Field observation RONJG092. **c.)** D veinlets hosted in porphyritic granodiorite, displaying a sericite halo. Field observation RONJG038. **d.)** Quartz vein reopened multiple times by magnetite, hosted in porphyritic basaltic andesite. Field observation RONJG110. **e.)** Magnetite veinlets with albite halos and local epidote hosted in porphyritic basaltic andesite. Field observation RONJG090.

Petrographic description

The quartz in the PCD-style veins differed from the quartz described in the epithermal veins in that no large, drusy, euhedral quartz crystals occurred. The quartz in sample D21-005 was medium grained and granular.

Where PCD-style veining occurred, the host rock hosted abundant pyrite mineralization (e.g. Figure 35 d. and f.). The pyrite occurred in clusters and was either fine-grained and anhedral or medium grained and euhedral. Pyrite also occurred as fracture filling in the wall rock or within the quartz veins. Cases were also observed in which the pyrite had reopened quartz veins. Such veins had halos of fine-grained quartz and illite, which would make them QSP veins, in other words, D veins (Figure 35 d.). Pyrite was observed altered to hematite in many examples.

Disseminated chalcopyrite in wall rock was observed in only one sample (D21-005), where disseminated pyrite was also present. The quartz vein in the sample had pyrite as fracture filling, and the vein was related to a fracture filled with abundant molybdenite (MoS_2) and pyrite mapped in the field (Figure 34 a.).

Molybdenite occurred as bright grey phenocrysts with very strong anisotropism of dark grey colours (Figure 35 a. and b.) and was observed in one BMQ vein sample (D21-010). The mineral occurred in the form of rosette texture (Figure 35 a.) at the rims of the vein, with the growth direction towards the centre of the vein on both sides. The vein had a centreline of fine-grained pyrite, fine-grained epidote, and fine-grained fibrous radial chlorite, possibly altered from amphibole (Figure 35 c.). The centreline was likely formed during a later re-opening of the BMQ vein. The vein also had an occurrence of isotropic, irregularly fracture-filling medium-grey poorly reflective mineral that filled fractures and intruded the quartz vein, which makes the mineral younger than the BMQ vein. The medium grey mineral was interpreted to be magnetite.

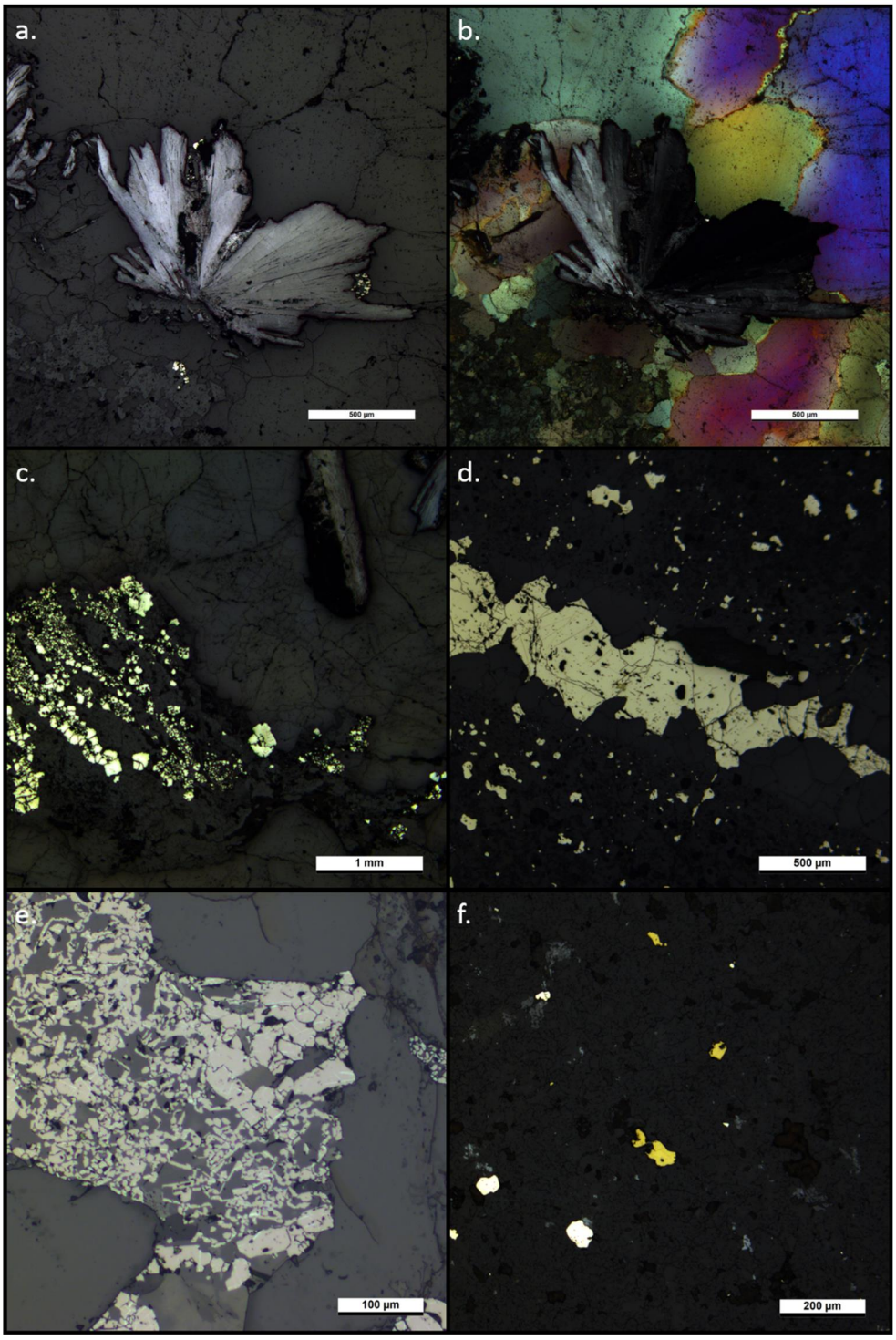

Figure 35: PCD-style vein mineralization; microphotographs taken in plain-polarized reflected light unless otherwise mentioned: **a.)** Flaky rosette texture molybdenite lining the sides of a quartz vein, growth direction toward the centre of the vein; typical BMQ vein. Thin section D21-010. **b.)** Anisotropy of the same molybdenite rosette visible in cross-polarized transmitted light. Thin section D21-010. **c.)** Pyrite, epidote, and chlorite centreline of a BMQ vein, above which a large molybdenite phenocryst can be seen. Thin section D21-010. **d.)** Quartz vein reopened by pyrite. Thin section D21-006. **e.)** Quartz vein reopened by magnetite which is partially altered to crystallographically oriented hematite. Thin section D21-015. **f.)** Disseminated anhedral chalcopyrite and pyrite in wall rock, related to a sinuous sugary quartz vein. Thin section D21-005.

A pinkish grey, poorly reflective isotropic mineral occupied the centre of the quartz vein in sample D21-015, which was clearly reopened after the quartz vein formed. The mineral was interpreted to be magnetite, as had also been done in the field. The magnetite was at times replaced by crystallographically oriented hematite (Figure 35 e.), which showed as a light grey mineral.

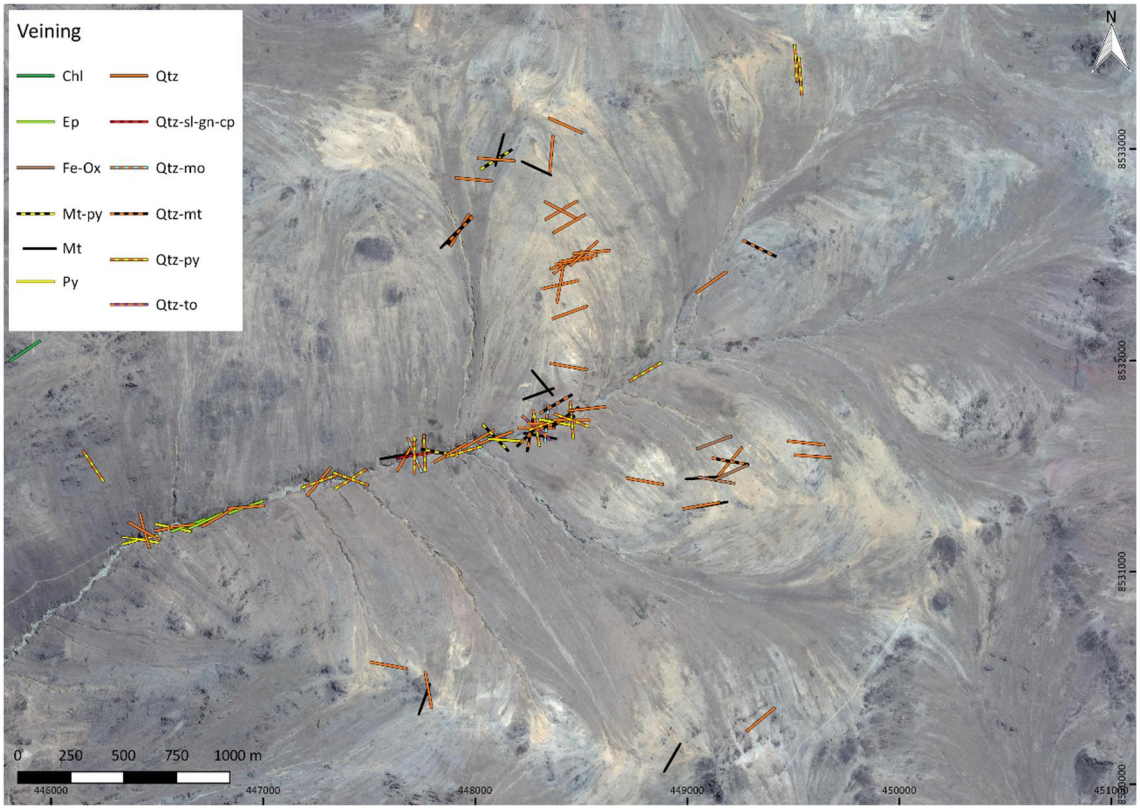

Figure 36: Veins and veinlets mapped at Ronaldo. (Chl = chlorite, Ep = epidote, Fe-Ox = iron oxides, Mt = magnetite, Mt-Py = magnetite-pyrite, Py = pyrite, Qtz = quartz, Qtz-Mo = quartz-molybdenite, Qtz-Mt = quartz-magnetite, Qtz-Py = quartz-pyrite, Qtz-Sl-Gn-Cp = quartz-sphalerite-galena-chalcopyrite-pyrite, Qtz-To = quartz-tourmaline)

4.4.4. Geochemical description

The average Ag/Au ratio of the studied low-sulfidation epithermal quartz veins was 148.3 (Table 3), which is well representative of a high Ag/Au value typical of low-sulfidation epithermal mineralization (White et al. 1995). This value was obtained from samples that were definitely representative of low-sulfidation mineralization (6 samples). There is quite a clear difference to the average Ag/Au ratio obtained from

intermediate-sulfidation epithermal quartz veins, which was 102.6. If the mineralization were high-sulfidation, the Ag/Au values would be anomalously low (White et al. 1995), which was clearly not the case. It is worth mentioning that there is significant dispersion in Ag/Au values obtained from both the low-sulfidation and intermediate-sulfidation epithermal veins. The Ag/Au values for low-sulfidation epithermal veins range from 15 to 297 (Table 3), while the Ag/Au values for intermediate-sulfidation epithermal veins range from 30 to 175. Three of the low-sulfidation epithermal vein samples have Ag/Au values from 216 to 297, which is the only consistent group of values thought to best represent the low-sulfidation epithermal mineralization.

Table 3: Au and Ag values of mineralized epithermal veins at Ronaldo.

	Sulfidation state	Ag	Au	Ag/Au
PES011278	Low-sulfidation	84.8	0.992	85.48
PES013122	Low-sulfidation	1.1	0.038	28.94
PES013116	Low-sulfidation	4110	16.65	246.84
PES013123	Low-sulfidation	392	1.81	216.57
PES013133	Low-sulfidation	159	0.535	297.19
PES013136	Low-sulfidation	25.9	1.735	14.92
Average		795.5	3.630	148.33
PES011252	Intermediate-sulfidation	1.1	0.037	29.72
PES011259	Intermediate-sulfidation	52.1	0.297	175.42
Average		26.6	0.170	102.58

The Ag value was highly elevated in most samples classified as low-sulfidation epithermal veins, as were the As and Au values (Table 1). The Hg and Li values were elevated in both low- and intermediate-sulfidation epithermal veins. The Mo values were consistently elevated in samples from low-sulfidation epithermal veins and also in the BMQ vein. The samples were enriched in Pb and depleted in S compared to samples collected from intermediate-sulfidation veins and PCD-style veins. This is most likely due

to the similar spatial positioning of the intermediate-sulfidation veins and the PCD-style veins compared to the low-sulfidation veins, since the intermediate-sulfidation epithermal veins and the PCD-style veins were situated along the major fault in the creek. The Sb values were somewhat higher in low-sulfidation epithermal veins than in other vein types and was significantly elevated in one sample, which was the one with pyrargyrite mineralization. Sc, Sm, Sr, Th, V, Y, and Zn were generally depleted in both low- and intermediate-sulfidation epithermal veins. The Te value was elevated in low-sulfidation epithermal veins, especially in the sample with pyrargyrite mineralization. All rare earth elements were less common in low- and intermediate-sulfidation epithermal veins than in PCD-style veins.

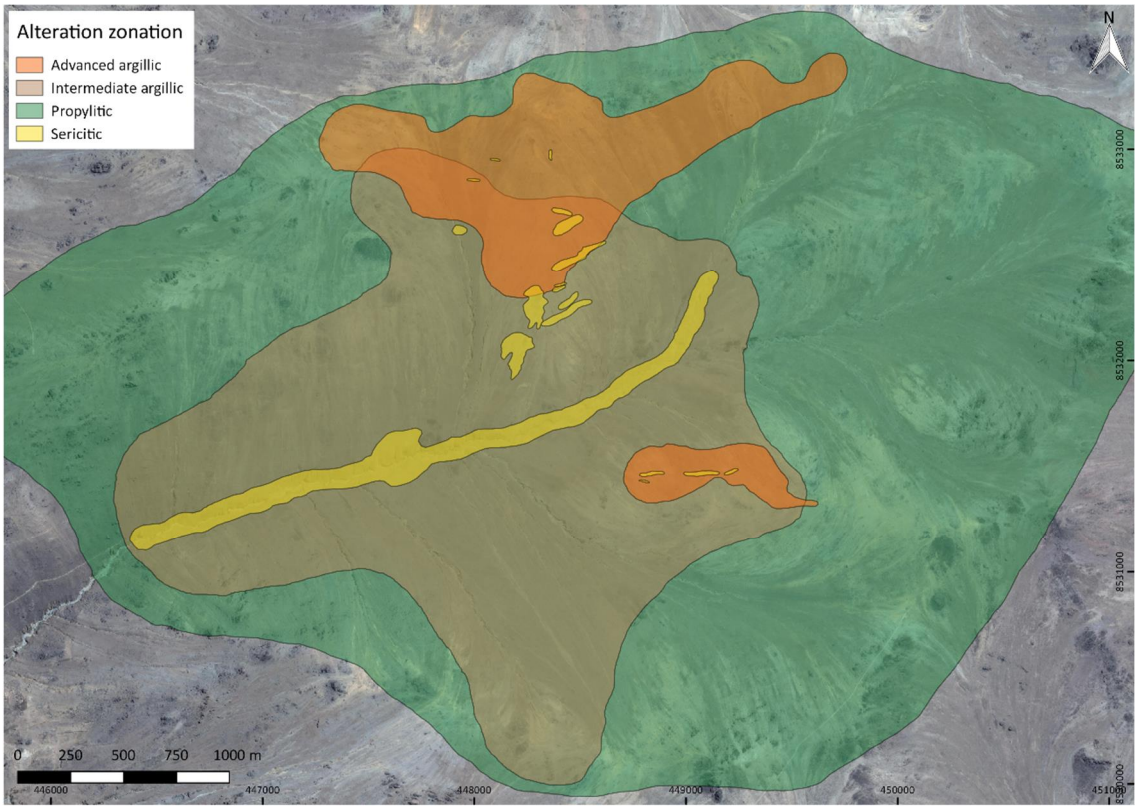

Figure 37: Alteration zonation at the Ronaldo prospect. The base map can be seen clearly in Figure 5.

It is important to note that the relative proportion of wall rock to vein material differs in the samples and sample groups (low-sulfidation epithermal, intermediate-sulfidation epithermal, and PCD style), and most certainly affects the assay results. Therefore, the whole-rock geochemical assay results regarding the vein samples with <70 wt. % SiO_2, should be viewed with some scepticism. In addition, there were not many samples for whole-rock geochemical assays from vein types: the best represented ones were low-sulfidation epithermal veins, of which there were 9 samples, and the two intermediate-sulfidation epithermal veins with distinct mineralization.

4.5. Hydrothermal alteration mineral analysis

All rock units at the Ronaldo prospect were affected by a rather confined hydrothermal system, in which different rock units tend to exhibit different alteration features. The alteration features at Ronaldo show a hydrothermal system which was weakened in the course of time. Extensive distal areas hosting extrusive units exhibit different degrees of propylitic alteration, while intrusive units generally exhibit intermediate argillic alteration. The highly elevated parts of Ronaldo exhibit advanced argillic alteration and intermediate argillic alteration, which can be observed as extensive colour anomalies in satellite imagery (Figure 5). The magmatic-hydrothermal breccia and the rocks near the major fault transecting the creek show sericitic alteration, as do the silicified ridges, which in addition exhibit extensive silicification. These features were observed during field work and were later confirmed and specified during SWIR analysis. Hydrothermal alteration minerals observed at Ronaldo using SWIR include muscovite, kaolinite, smectite, pyrophyllite, tourmaline, and chlorite (Table 5). Petrographic examination showed that many of the primary mineralogical contents had been altered to secondary minerals such as sericite, illite, smectite, chlorite, and epidote. The detailed field examinations of the hydrothermal alteration mineralogy and the SWIR analysis results are presented below.

4.5.1. Field observations

The main alteration features observed at Ronaldo were widespread, distal propylitic alteration in extrusive rocks, intermediate argillic alteration in intrusive rocks and somewhat minor advanced argillic alteration, the latter of which displayed an extensive colour anomaly observed in satellite imagery (Figure 5) and at the macroscopic scale (Figure 17 b. and f.). Smectite, illite, kaolinite, and goethite were abundant in the porphyritic diorite intrusion and appeared around silicified ridges in the host rock. Smectite, which typifies intermediate argillic alteration, was the most abundant alteration mineral related to the intrusive unites. This hydrothermal mineral is the result of a weaker and lower temperature form of hydrolytic alteration than sericitic alteration (Figure 40 e. and f.). Smectite can be found in most places in the prospect but mostly related to the altered porphyritic diorite intrusion, and to some extent the weakly altered overlying extrusive units. The abundant occurrence of smectite strongly suggests that the hydrothermal system waned over time and that overprinting of previous alteration likely occurred. Isolated magnetite aggregates in the magmatic-hydrothermal breccia may also be indicative of overprinting of previous alteration at Ronaldo.

Kaolinite, pyrophyllite, and dumortierite, all of which were observed at Ronaldo, are characteristic alteration minerals of an advanced argillic lithocap, possibly connected to a deep-seated PCD. Kaolinite-bearing samples (Figure 17 b.) were only found at high elevations in the prospect (>4440 m), and mostly on the northern hill. Pyrophyllite-bearing samples also occurred at the same elevation and near kaolinite-bearing samples.

Figure 38: Field photographs of hydrothermal alteration minerals: **a.)** Intermediate argillic-altered porphyritic diorite crosscut by a stockwork of quartz-sericite-tourmaline veinlets. Field observation RONJG080. **b.)** Hornfelsed basaltic andesite displaying chlorite-epidote alteration. Field observation RONJG007. **c.)** Silicified, tourmaline-bearing magmatic-hydrothermal breccia displaying sericite-goethite alteration. Field observation RONJG080. **d.)** Abundant dumortierite in strongly silicified host rock with strong surficial goethite alteration. Field observation RONJG065. **e.)** Abundant surficial jarosite alteration in magmatic-hydrothermal breccia near the major fault. Field observation RONJG089. **f.)** Strongly silicified porphyritic granodiorite displaying hematite and goethite alteration. Field observation RONJG016.

Now, the advanced argillic lithocap is largely eroded and only the roots of the once larger lithocap are visible as silicified ridges. There was no evidence of advanced argillic alteration zones being overprinted by later, sericitic alteration, but it is possible that overprinting of advanced argillic alteration and sericitic alteration by later intermediate argillic alteration occurred at Ronaldo. The clay minerals, such as kaolinite and smectite have mostly replaced plagioclase phenocrysts in the argillic alteration zones. Iron oxides were mostly found infilling voids and replacing the ground mass (Figure 19 f. and Figure 38 c. and f.) of the silicified, sericitic, or intermediate argillic-altered rocks.

In areas dominated by advanced argillic and intermediate argillic alteration, the silicified ridges exhibited sericitic alteration. The more distal parts of the silicified ridges were smectite bearing and represent intermediate argillic alteration. The host rock around these silicified ridges did not exhibit sericitic alteration but rather graded out from advanced argillic to intermediate argillic alteration. The silicified ridges and magmatic-hydrothermal breccia were largely impregnated by sericite, clay minerals, and, most importantly, replacement silica (Figure 38 c., d., and f.). The interpretation is that the silicified ridges are temporally related to the advanced argillic alteration and most likely crosscut the intermediate argillic alteration.

Areas with sericite, sericite-chlorite, and tourmaline alteration were widely observed in the creek, which indicates sericitic alteration of the rock. Sericite-chlorite alteration was mostly confined to the major fault in the creek. The muscovite-bearing samples, which characterize the sericitic alteration zone, were only confined to narrow or otherwise limited areas and were encompassed by either propylitic, advanced argillic, or intermediate argillic alteration. It is important to note that sericitic alteration was identified in only a small volume of rock in the examination of the entire prospect. In turn, tourmaline is a diagnostic hydrothermal alteration mineral of magmatic-hydrothermal breccia (Figure 24 c.). The observed tourmaline-bearing samples were indeed related to magmatic-hydrothermal breccias and occurred in the same areas where sericitic alteration occurred.

Many of the rocks related to the silicified ridges and rocks in the creek were subjected to fracture filling and iron oxide staining caused by supergene sulfide oxidation. Abundant pyrite mineralization was observed in the wall rock around the major fault,

because the fault likely functioned as a major fluid conduit. At times, the major fault hosted abundant jarosite, a secondary hydrous sulfate (Figure 38 e.). The jarosite observed in the creek close to the fault was observed in the porphyritic diorite and the related hydrothermal breccia. The jarosite formed in an acidic environment by oxidizing the abundant pyrite and possibly other sulfides related to the fault in the creek. Iron oxides related to the silicified ridges were formed in less acidic environments, and the dominant iron oxides there were goethite and hematite. Thus, it is safe to assume that the acidic environment was strictly confined to the major fault in the creek.

Propylitic alteration was abundant in all parts of the prospect, excluding the areas of advanced argillic and sericitic alteration surrounding the silicified ridges (Figure 37) and the intermediate argillic-altered intrusive units, making propylitic alteration by far the most widespread hydrothermal alteration feature at Ronaldo. Chlorite and epidote typify the propylitic alteration zone (Figure 38 b.), which was especially prominent in the elevated, distal parts of the prospect, in the extrusive units. Propylitic alteration was also present in the creek, but farther away from the major fault. The clay-rich area near the fault which exhibited sericitic alteration and focused pyrite precipitation, was limited to a narrow area and was juxtaposed with propylitic alteration. Even at distances of a few metres away from the fault, propylitic altered rock with no sericitic alteration could be observed. In some places on the northern hill, porphyritic, propylitic-altered basaltic andesites exhibited abundant magnetite veinlets, which most likely originate from the underlying porphyritic diorite intrusion.

Propylitic alteration characterized by chlorite and epidote was the most widespread alteration type at Ronaldo (Figure 39 a. and b., Figure 40 c. and d., and Figure 38 b.). The SWIR analysis results did not show much chlorite (Table 5), but observations in the field showed chlorite and epidote alteration in the host rock throughout most of the prospect. Propylitic alteration was also abundant in the creek, even a few metres away from the fault, where generally smectite and sericite were the dominant alteration minerals.

No evident potassic alteration minerals were observed, except for some hydrothermal biotite and possible potassium feldspar in xenoliths in some igneous breccias. The

isolated magnetite aggregates (Figure 24 d.) in magmatic-hydrothermal breccia may be indicative of sericitic overprinting of underlying potassic alteration (Figure 42).

The Ronaldo prospect seems to exhibit features associated with root zones beneath lithocaps, which are characterized by broad vertical and narrow lateral alteration zonation. The quartz-muscovite alteration assemblage was the most dominant vertical alteration zonation in the silicified ridges, with only a few samples displaying pyrophyllite and some samples displaying kaolinite alteration, which is associated with shallower level lithocap alteration. Thus, one can conclude that the prospect is spatially situated in erosional remnants of deep parts of a lithocap, close to its root zone. Further evidence supporting this interpretation is that – rather than tourmaline – dumortierite is the principal borosilicate mineral in lithocaps. Both tourmaline and dumortierite were observed at Ronaldo, and dumortierite specifically at high elevations in the advanced argillic alteration zone. As previously mentioned, it was observed that the lateral alteration halo around the major fault in the creek was quite narrow, only a few metres wide. The silicified ridges have relatively sharp contacts with the wall rock and pass outward to advanced argillic and intermediate argillic alteration assemblages: this is a distinct feature of deep-level lithocaps (Holliday et al. 2007).

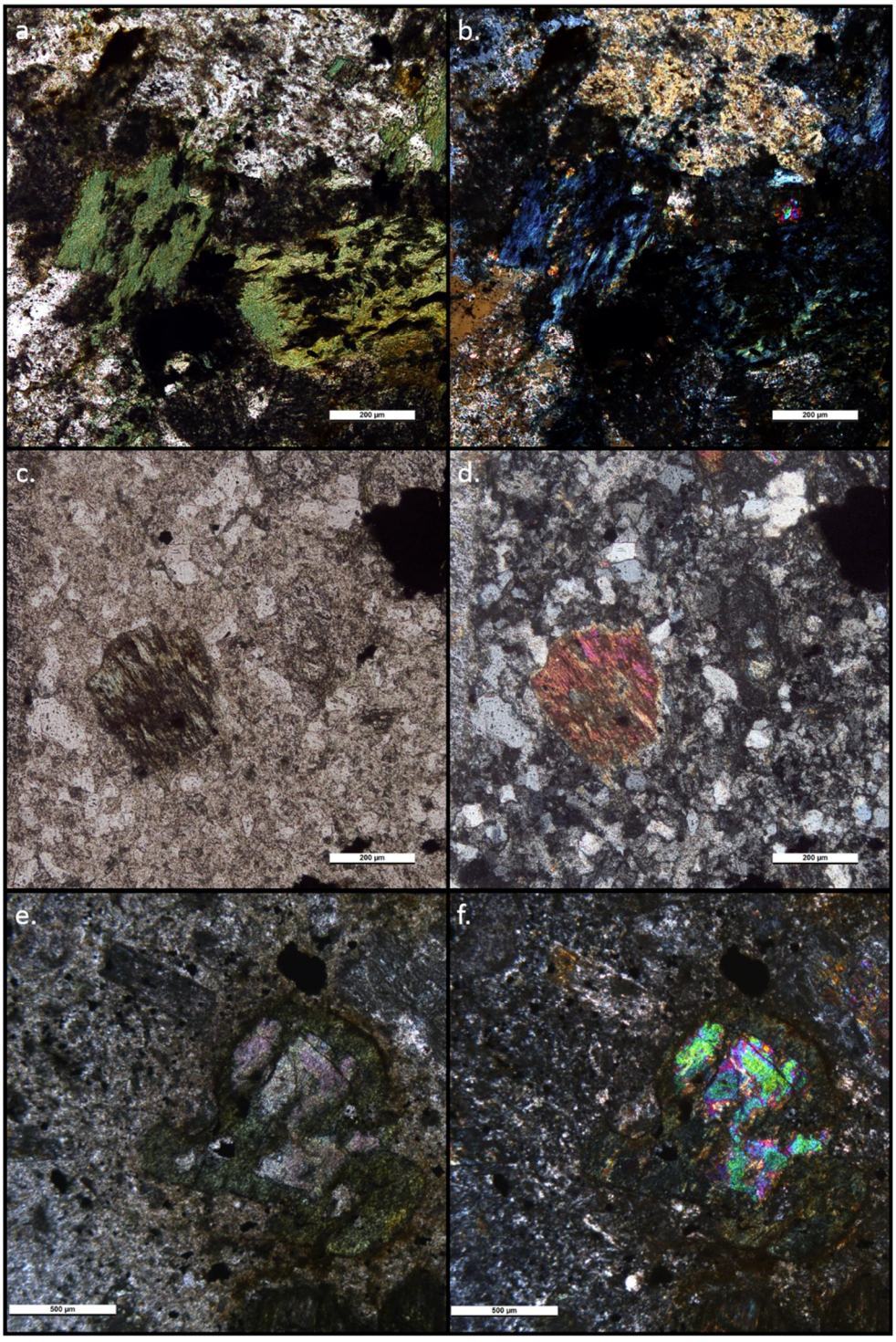

Figure 39: Alteration minerals in microphotographs: **a.)** Chloritized biotite. Thin section PES011251 (ppl). **b.)** Chlorite displaying anomalous Berlin blue interference colours. Thin section PES011251 (xpl). **c.)** Thin section PES011288 (ppl). **d.**) Amphibole with clear twinning. Thin section PES011288. **e.)** Thin section PES011231 (ppl). **f.)** Ca-rich amphibole altered to epidote in centre, engulfed by biotite altered to chlorite. Thin section PES011231 (xpl).

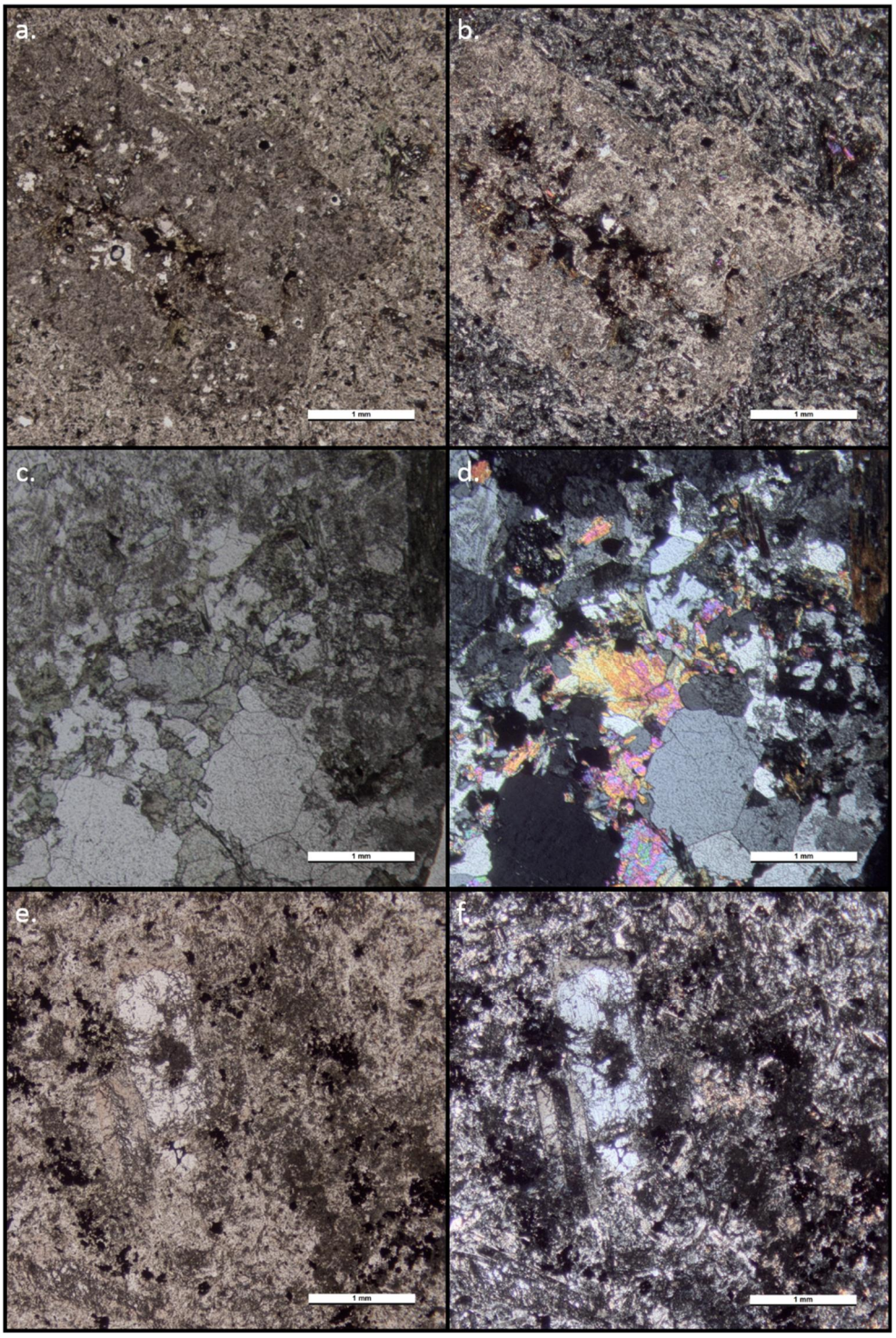

Figure 40: Alteration minerals in microphotographs: **a.)** Thin section PES011251 (ppl). **b.)** Large plagioclase phenocryst pervasively altered to illite. Thin section PES011251 (xpl). **c.)** Thin section PES013146 (ppl). **d.)** Aplitic dike with abundant epidote. Thin section PES013146 (xpl). **e.)** Thin section PES011279 (ppl). **f.)** Porphyritic basaltic andesite groundmass altered to smectite; patchy texture. Thin section PES011279 (xpl).

Table 4: Summary of minerals identified in SWIR spectra by means of the software and extracted spectral data.

	Rock Type	TSA Mineral 1	TSA Mineral 2	TSA Mineral 3	1400 nm λ position	1400 mn depth	1480 nm λ position	1480 mn depth	1550 nm λ position	1550 mn depth	1760 mn depth	1900 mn depth	2160 mn depth	2200 nm λ position	2200 mn depth	2250 nm λ position	2250 mn depth	2340 nm λ position	2390 nm λ position
PES011227	Porphyritic basaltic andesite	NULL	NULL	NULL	1398.5	0.0075	1460.6	0.0002	1540.4	0.0003	0.0010	0.0041	1.0010	2188.1	0.0124	2249.1	0.0030	2324.2	2391.7
PES011228	Magmatic-hydrothermal breccia	Paragonite	Montmorillonite	Pyrophyllite	1395.8	0.2080	1465.3	0.0018	1558.0	0.0001	0.0020	0.0886	1.0310	2193.2	0.2420	2255.6	0.0000	2345.5	2386.5
PES011229	Porphyritic basaltic andesite	NULL	NULL	NULL	1397.9	0.0069	NULL	NULL	1557.6	0.0003	0.0005	0.0088	1.0010	2182.6	0.0111	2252.4	0.0058	2323.0	2396.2
PES011230	Diorite	Aspectral	NULL	NULL	1396.2	0.0025	1471.3	0.0002	1537.4	0.0003	0.0010	0.0026	1.0000	2184.7	0.0131	2259.9	0.0017	2326.8	2387.2
PES011231	Porphyritic diorite	Siderite	Montmorillonite	Kaolinite-PX	1412.6	0.0241	1461.9	0.0003	1559.4	0.0003	0.0006	0.0519	1.0020	2205.0	0.0378	2251.3	0.0065	2331.5	2394.4
PES011232	Porphyritic diorite	Muscovitic lite	Montmorillonite	NULL	1410.7	0.1850	1461.3	0.0023	1561.2	0.0002	0.0015	0.1050	0.9810	2196.0	0.2230	2247.2	0.0051	2346.2	2384.3
PES011233	Porphyritic basaltic andesite	Siderite	Chlorite-FeMg	Muscovite	1398.8	0.0129	1465.5	0.0001	1558.9	0.0003	0.0006	0.0274	1.0000	2196.9	0.0140	2251.5	0.0105	2343.2	2407.0
PES011234	Basaltic andesite	NULL	NULL	NULL	1397.8	0.0123	NULL	NULL	1559.8	0.0002	0.0011	0.0126	1.0000	2194.1	0.0116	2249.9	0.0041	2323.2	2392.3
PES011237	Porphyritic basaltic andesite	Aspectral	NULL	NULL	1397.3	0.0030	1465.4	0.0004	1539.1	0.0002	0.0008	0.0059	1.0000	2188.0	0.0128	2246.8	0.0043	2326.9	2397.4
PES011240	Silicified ridge	Muscovite	NULL	NULL	1409.6	0.1900	1467.1	0.0006	1559.8	0.0003	0.0016	0.0585	0.9760	2194.2	0.2480	2247.2	0.0000	2343.2	2380.5
PES011241	Porphyritic granodiorite	Muscovite	NULL	NULL	1410.0	0.0656	NULL	NULL	1560.4	0.0003	0.0007	0.0091	0.9820	2195.7	0.1210	2263.7	0.0003	2343.9	2382.2
PES011242	Porphyritic granodiorite	Muscovitic lite	Montmorillonite	NULL	1410.8	0.1490	1466.0	0.0021	1560.4	0.0004	0.0011	0.1240	0.9790	2195.7	0.1890	2252.9	0.0007	2345.0	2380.2
PES011243	Porphyritic granodiorite	Montmorillonite	Chlorite-Fe	Ankerite	1410.8	0.0419	1461.1	0.0016	1537.4	0.0005	0.0006	0.0844	0.9930	2201.8	0.0458	2251.8	0.0120	2343.7	2381.6
PES011246	Silicified ridge	Muscovite	Siderite	NULL	1412.6	0.0525	1463.7	0.0014	1560.4	0.0004	0.0011	0.0570	0.9920	2199.3	0.0816	2253.3	0.0012	2344.0	2380.6
PES011247	Porphyritic diorite	Siderite	Chlorite-FeMg	Montmorillonite	1411.0	0.0220	1463.9	0.0001	1559.3	0.0003	0.0007	0.0282	0.9990	2203.9	0.0335	2252.0	0.0178	2341.7	2389.0
PES011248	Porphyritic diorite	Chlorite-FeMg	Siderite	Muscovite	1396.5	0.0263	1476.0	0.0002	1560.8	0.0004	0.0006	0.0427	0.9980	2196.8	0.0056	2249.3	0.0359	2337.2	2395.7

PES011249	Porphyritic diorite	Chlorite-Mg	Tourmaline-Fe	NULL	1393.2	0.0205	NULL	NULL	1561.7	0.0006	0.0006	0.0274	0.9980	2194.8	0.0042	2248.4	0.0357	2330.1	2388.6
PES011250	Porphyritic basaltic andesite	NULL	NULL	NULL	1399.7	0.0066	1461.3	0.0001	1534.1	0.0002	0.0005	0.0084	1.0000	2192.4	0.0097	2251.5	0.0084	2333.8	2393.9
PES011251	Porphyritic diorite	Chlorite-FeMg	MuscoviticIllite	NULL	1411.6	0.0383	1466.3	0.0003	1544.5	0.0006	0.0007	0.0385	0.9940	2200.8	0.0459	2252.2	0.0191	2343.0	2401.6
PES011252	Diorite	Phengitic Illite	Siderite	Montmorillonite	1411.9	0.0461	1462.2	0.0011	1562.1	0.0003	0.0008	0.0574	0.9910	2199.3	0.0645	2250.7	0.0022	2346.7	2400.8
PES011253	Diorite	Muscovite	Chlorite-FeMg	NULL	1411.8	0.1320	1465.1	0.0012	1562.7	0.0004	0.0010	0.0648	0.9790	2199.2	0.1510	2251.8	0.0052	2345.8	2402.7
PES011254	Diorite	Muscovitic Illite	NULL	NULL	1411.2	0.2230	1466.3	0.0005	1563.5	0.0004	0.0012	0.0704	0.9710	2196.4	0.2580	2247.3	0.0001	2344.5	2379.3
PES011255	Basaltic andesite	Aspectral	NULL	NULL	1397.3	0.0030	NULL	NULL	1563.4	0.0004	0.0010	0.0059	1.0000	2186.7	0.0128	2248.9	0.0040	2323.4	2384.8
PES011256	Diorite	Aspectral	NULL	NULL	1402.1	0.0029	NULL	NULL	1560.9	0.0002	0.0005	0.0092	1.0000	2184.4	0.0137	2250.0	0.0043	2327.8	2392.7
PES011257	Magmatic-hydrothermal breccia	Paragonitic Illite	Montmorillonite	NULL	1409.4	0.2120	1465.6	0.0020	1565.0	0.0001	0.0011	0.1370	0.9870	2192.4	0.2500	2250.9	0.0040	2341.9	2386.7
PES011258	Magmatic-hydrothermal breccia	Siderite	Chlorite-Mg	Montmorillonite	1396.6	0.0318	NULL	NULL	1534.0	0.0003	0.0008	0.0522	0.9990	2198.7	0.0128	2248.7	0.0141	2327.0	2388.4
PES011259	Magmatic-hydrothermal breccia	Montmorillonite	Kaolinite-PX	NULL	1412.7	0.0655	1465.1	0.0008	1561.0	0.0003	0.0005	0.0804	1.0030	2205.5	0.1020	2252.8	0.0020	2348.5	2386.1
PES011262	Magmatic-hydrothermal breccia	Phengite	Chlorite-FeMg	Siderite	1411.0	0.0654	NULL	NULL	1563.7	0.0004	0.0004	0.0889	0.9900	2203.3	0.0574	2251.0	0.0302	2344.3	2404.4
PES011263	Porphyritic granodiorite	Muscovitic Illite	Chlorite-FeMg	NULL	1411.5	0.0598	1462.6	0.0004	1563.3	0.0002	0.0007	0.0464	0.9880	2198.9	0.0796	2252.8	0.0113	2344.2	2381.5
PES011264	Porphyritic granodiorite	Muscovite	NULL	NULL	1409.8	0.1860	1470.3	0.0030	1561.8	0.0001	0.0026	0.0557	0.9670	2194.7	0.2320	2251.5	0.0002	2343.4	2387.5
PES011266	Porphyritic granodiorite	Siderite	Montmorillonite	Chlorite-FeMg	1412.7	0.0188	1460.8	0.0004	1547.6	0.0006	0.0006	0.0361	1.0000	2205.6	0.0290	2252.6	0.0143	2342.0	2403.7
PES011267	Porphyritic granodiorite	Muscovitic Illite	Montmorillonite	NULL	1411.5	0.1880	1466.1	0.0027	1552.1	0.0001	0.0016	0.1210	0.9780	2199.1	0.1970	2251.6	0.0002	2345.0	2390.0
PES011272	Porphyritic basaltic andesite	Muscovite	Kaolinite-PX	NULL	1412.5	0.1890	1470.8	0.0021	1545.3	0.0001	0.0021	0.1100	1.0110	2205.0	0.2190	2243.1	0.0016	2348.6	2384.3
PES011273	Porphyritic basaltic andesite	Kaolinite-PX	Tourmaline-Fe	Magnesite	1413.5	0.0586	1467.9	0.0004	1544.6	0.0001	0.0005	0.0803	1.0100	2206.8	0.1050	2242.3	0.0063	2356.2	2385.8

PES011275	Porphyritic basaltic andesite	Kaolinite-PX	Montmorillonite	Chlorite-FeMg	1413.0	0.2120	1467.4	0.0042	1543.1	0.0000	0.0010	0.2020	1.0290	2206.4	0.2280	2245.5	0.0097	2351.2	2384.1
PES011276	Silicified ridge	Muscovite	NULL	NULL	1411.0	0.1770	1466.1	0.0009	1565.2	0.0001	0.0015	0.0690	0.9720	2197.6	0.2190	2259.6	0.0001	2345.1	2386.3
PES011277	Silicified ridge	Muscovite	NULL	NULL	1410.3	0.1730	1468.0	0.0017	1550.4	0.0001	0.0019	0.0778	0.9760	2195.2	0.2090	2260.0	0.0001	2344.4	2393.9
PES011278	Silicified ridge	Tourmaline-Fe	Muscovite	Magnesite	1409.9	0.0234	1468.0	0.0004	1562.0	0.0003	0.0009	0.0277	0.9920	2200.1	0.0590	2245.0	0.0238	2358.0	2393.9
PES011279	Porphyritic basaltic andesite	Siderite	Montmorillonite	Chlorite-FeMg	1408.8	0.0229	1465.2	0.0008	1558.7	0.0003	0.0009	0.0560	0.9990	2201.7	0.0238	2248.4	0.0095	2327.4	2395.6
PES011281	Porphyritic basaltic andesite	Muscovite	NULL	NULL	1410.6	0.1070	1465.6	0.0002	1560.8	0.0004	0.0006	0.0296	0.9740	2196.6	0.1870	2261.2	0.0003	2345.1	2388.3
PES011283	Silicified ridge	Muscovite	NULL	NULL	1410.8	0.1370	1465.0	0.0012	1558.2	0.0001	0.0014	0.0759	0.9770	2197.2	0.1860	2247.0	0.0009	2345.9	2385.2
PES011284	Igneous breccia	NULL	NULL	NULL	1398.4	0.0106	1460.9	0.0002	1561.0	0.0003	0.0007	0.0201	1.0000	2198.5	0.0149	2250.8	0.0064	2326.5	2388.2
PES011285	Porphyritic diorite	Siderite	Montmorillonite	NULL	1412.2	0.0311	1466.8	0.0006	1536.8	0.0002	0.0006	0.0866	1.0000	2204.0	0.0354	2251.5	0.0094	2342.8	2402.5
PES011286	Porphyritic diorite	Kaolinite-PX	Siderite	Montmorillonite	1413.0	0.0686	1467.4	0.0008	1562.1	0.0003	0.0005	0.1100	1.0080	2206.0	0.1100	2251.6	0.0020	2351.6	2385.7
PES011287	Igneous breccia	Siderite	Montmorillonite	NULL	1400.5	0.0126	1463.1	0.0003	1560.4	0.0005	0.0006	0.0340	1.0000	2202.3	0.0241	2251.1	0.0062	2327.0	2392.7
PES011288	Porphyritic diorite	Siderite	Muscovite	Chlorite-FeMg	1412.1	0.0277	1463.5	0.0002	1541.7	0.0009	0.0007	0.0531	1.0020	2204.7	0.0363	2252.2	0.0163	2340.8	2387.5
PES011290	Silicified ridge	Kaolinite-WX	Paragonite	Pyrophyllite	1394.2	0.2440	1462.3	0.0014	1559.9	0.0001	0.0025	0.0658	1.0750	2167.8	0.2390	2259.8	0.0003	2321.1	2385.9
PES011291	Silicified ridge	Muscovite	Magnesite	NULL	1412.6	0.0668	1466.1	0.0012	1560.6	0.0003	0.0011	0.0508	0.9910	2202.7	0.0965	2249.1	0.0021	2345.9	2386.2
PES011292	Ignimbrite	Chlorite-FeMg	Muscovite	NULL	1410.7	0.0835	NULL	NULL	1547.0	0.0006	0.0001	0.0705	0.9860	2202.1	0.1030	2251.2	0.0413	2343.8	2384.4
PES011295	Silicified ridge	Muscovite	NULL	NULL	1410.5	0.1590	1467.0	0.0010	1560.0	0.0003	0.0015	0.0447	0.9710	2196.2	0.2110	2253.3	0.0000	2344.7	2385.5
PES013101	Porphyritic diorite	Muscovite	NULL	NULL	1410.8	0.1780	1468.6	0.0010	1534.7	0.0002	0.0017	0.0709	0.9710	2196.6	0.2260	2266.0	0.0000	2345.2	2383.8
PES013102	Porphyritic diorite	Siderite	Montmorillonite	NULL	1410.8	0.0213	NULL	NULL	1540.2	0.0001	0.0011	0.0518	0.9990	2203.1	0.0286	2249.0	0.0070	2326.1	2392.2
PES013103	Ignimbrite	Chlorite-FeMg	Muscovitic llite	Kaolinite-PX	1411.7	0.0586	1463.0	0.0003	1560.8	0.0003	0.0004	0.1010	0.9930	2203.7	0.0771	2251.3	0.0212	2347.1	2406.4

PES013104	Porphyritic basaltic andesite	Siderite	Montmorillonite	NULL	1395.7	0.0136	NULL	NULL	1546.2	0.0004	0.0006	0.0219	1.0010	2185.0	0.0136	2250.5	0.0053	2317.8	2391.8
PES013105	Magmatic-hydrothermal breccia	Muscovitic lllite	Montmorillonite	Siderite	1411.6	0.2020	1469.0	0.0026	1544.8	0.0000	0.0018	0.1100	0.9770	2198.3	0.2080	2247.0	0.0000	2345.8	2383.3
PES013106	Basaltic andesite	Siderite	Montmorillonite	Chlorite-FeMg	1408.7	0.0167	NULL	NULL	1559.4	0.0002	0.0007	0.0501	0.9990	2201.9	0.0175	2250.9	0.0137	2343.4	2394.5
PES013107	Magmatic-hydrothermal breccia	Tourmaline-Fe	Paragonite	Magnesite	1409.2	0.1090	NULL	NULL	1553.6	0.0002	0.0009	0.0717	0.9810	2201.3	0.1800	2246.4	0.1170	2354.3	2400.6
PES013108	Basaltic andesite	Siderite	Chlorite-Mg	Montmorillonite	1400.6	0.0164	NULL	NULL	1562.9	0.0007	0.0007	0.0121	0.9980	2194.0	0.0153	2251.1	0.0122	2330.7	2392.3
PES013109	Porphyritic basaltic andesite	NULL	NULL	NULL	1398.8	0.0071	1462.9	0.0002	1559.0	0.0003	0.0007	0.0074	1.0000	2184.1	0.0104	2255.3	0.0065	2327.7	2393.5
PES013112	Porphyritic basaltic andesite	Aspectral	NULL	NULL	1395.4	0.0054	NULL	NULL	1560.1	0.0002	0.0006	0.0063	1.0000	2185.3	0.0110	2250.6	0.0058	2329.2	2390.0
PES013114	Silicified ridge	Muscovite	NULL	NULL	1410.3	0.1670	1494.4	0.0003	1562.4	0.0003	0.0015	0.0320	0.9650	2195.3	0.2360	2259.7	0.0001	2343.6	2386.3
PES013116	Silicified ridge	Muscovite	NULL	NULL	1411.1	0.0422	1467.2	0.0030	1562.1	0.0002	0.0012	0.0497	0.9910	2196.2	0.0742	2255.7	0.0004	2343.1	2384.1
PES013117	Silicified ridge	Muscovite	NULL	NULL	1410.0	0.1840	1467.2	0.0017	1563.3	0.0003	0.0012	0.0926	0.9760	2194.4	0.2560	2261.6	0.0001	2343.2	2383.6
PES013118	Magmatic-hydrothermal breccia	Tourmaline-Fe	Muscovite	Magnesite	1408.0	0.0561	1460.3	0.0017	1564.3	0.0003	0.0007	0.0407	0.9790	2203.0	0.1570	2245.5	0.1270	2356.5	2389.0
PES013119	Magmatic-hydrothermal breccia	Muscovite	NULL	NULL	1409.8	0.1310	1469.7	0.0009	1558.1	0.0001	0.0010	0.0456	0.9730	2194.4	0.2170	2253.7	0.0000	2342.3	2384.4
PES013120	Porphyritic basaltic andesite	NULL	NULL	NULL	1397.8	0.0053	NULL	NULL	1563.7	0.0003	0.0009	0.0050	1.0000	2183.3	0.0113	2249.7	0.0058	2327.2	2393.6
PES013121	Porphyritic basaltic andesite	NULL	NULL	NULL	1398.1	0.0056	1474.4	0.0002	1558.6	0.0003	0.0006	0.0087	1.0000	2187.2	0.0121	2253.4	0.0054	2331.3	2392.4
PES013122	Silicified ridge	Muscovite	NULL	NULL	1409.8	0.1300	1474.6	0.0005	1536.5	0.0001	0.0014	0.0312	0.9760	2195.1	0.1810	2245.6	0.0041	2345.4	2385.1
PES013123	Silicified ridge	Muscovite	Magnesite	Tourmaline-Fe	1411.2	0.0515	1467.5	0.0027	1563.0	0.0001	0.0013	0.0555	0.9890	2196.9	0.0881	2245.9	0.0066	2348.1	2385.2
PES013124	Porphyritic diorite	Siderite	Montmorillonite	NULL	1411.9	0.0139	1465.0	0.0002	1563.8	0.0002	0.0005	0.0274	1.0000	2202.2	0.0283	2250.2	0.0040	2324.1	2384.7

PES013125	Porphyritic basaltic andesite	NULL	NULL	NULL	1395.9	0.0096	NULL	NULL	1560.2	0.0006	0.0010	0.0083	1.0000	2190.6	0.0103	2247.1	0.0066	2323.0	2393.0
PES013126	Porphyritic basaltic andesite	Aspectral	NULL	NULL	1394.9	0.0047	1460.9	0.0002	1541.0	0.0005	0.0009	0.0055	1.0010	2187.4	0.0136	2251.1	0.0026	2321.7	2404.6
PES013127	Porphyritic diorite	Siderite	Montmorillonite	Kaolinite-PX	1412.3	0.0318	1467.6	0.0005	1561.3	0.0003	0.0004	0.0794	1.0010	2205.0	0.0407	2252.0	0.0093	2336.7	2390.6
PES013128	Porphyritic diorite	Siderite	Montmorillonite	Kaolinite-PX	1412.7	0.0269	1469.1	0.0003	1538.6	0.0002	0.0005	0.0516	1.0030	2205.5	0.0463	2247.3	0.0042	2325.0	2388.4
PES013129	Ignimbrite	Aspectral	NULL	NULL	1410.2	0.0029	NULL	NULL	1560.0	0.0004	0.0008	0.0082	1.0000	2194.2	0.0143	2253.0	0.0027	2327.7	2394.7
PES013130	Ignimbrite	Muscovitic lllite	Montmorillonite	NULL	1411.5	0.1240	1465.1	0.0009	1560.9	0.0002	0.0009	0.0610	0.9810	2198.3	0.1560	2254.9	0.0002	2344.3	2382.3
PES013131	Silicified ridge	Muscovite	NULL	NULL	1409.7	0.1580	1472.5	0.0005	1560.8	0.0002	0.0010	0.0361	0.9760	2194.2	0.2450	2241.9	0.0002	2342.2	2383.4
PES013132	Silicified ridge	Muscovite	NULL	NULL	1410.0	0.1810	1469.2	0.0015	1559.6	0.0001	0.0022	0.0703	0.9780	2194.7	0.2190	2251.6	0.0001	2344.4	2380.2
PES013133	Silicified ridge	Muscovitic lllite	Siderite	NULL	1411.0	0.0729	1466.6	0.0012	1559.6	0.0002	0.0012	0.0563	0.9870	2196.4	0.1140	2244.9	0.0001	2343.9	2404.1
PES013134	Porphyritic diorite	NULL	NULL	NULL	1397.9	0.0079	NULL	NULL	1560.5	0.0004	0.0006	0.0067	1.0000	2191.2	0.0117	2253.6	0.0048	2323.1	2391.7
PES013135	Silicified ridge	Muscovite	Siderite	NULL	1410.8	0.1000	1467.6	0.0043	1541.3	0.0001	0.0013	0.1120	0.9850	2196.5	0.1460	2253.9	0.0001	2344.8	2382.3
PES013136	Silicified ridge	Muscovitic lllite	Montmorillonite	Siderite	1411.2	0.0862	1464.0	0.0009	1563.5	0.0002	0.0010	0.0560	0.9880	2197.2	0.1180	2244.8	0.0001	2344.4	2404.8
PES013137	Silicified ridge	Muscovitic lllite	Montmorillonite	NULL	1411.4	0.2420	1467.6	0.0013	1561.0	0.0002	0.0013	0.1080	0.9740	2196.2	0.2650	2252.5	0.0003	2344.9	2381.4
PES013138	Ignimbrite	Muscovite	NULL	NULL	1410.4	0.1000	NULL	NULL	1559.8	0.0002	0.0009	0.0320	0.9840	2194.9	0.1460	2253.2	0.0002	2343.8	2380.4
PES013139	Ignimbrite	Muscovitic lllite	Kaolinite-PX	Montmorillonite	1412.3	0.1400	1467.1	0.0024	1561.6	0.0003	0.0008	0.1200	1.0020	2204.7	0.1760	2261.5	0.0001	2347.4	2386.1
PES013140	Silicified ridge	Muscovitic lllite	NULL	NULL	1410.7	0.1840	1466.1	0.0008	1561.5	0.0005	0.0013	0.0710	0.9740	2195.8	0.2220	2249.9	0.0000	2345.0	2385.7
PES013141	Silicified ridge	Muscovitic lllite	NULL	NULL	1410.9	0.1370	1465.1	0.0003	1565.3	0.0001	0.0011	0.0474	0.9780	2195.9	0.1860	2253.7	0.0003	2343.8	2381.3
PES013142	Ignimbrite	Siderite	NULL	NULL	1414.1	0.0038	1474.3	0.0010	1540.2	0.0004	0.0011	0.0147	1.0000	2184.2	0.0133	2251.7	0.0037	2327.0	2406.5
PES013143	Ignimbrite	Aspectral	NULL	NULL	1401.1	0.0022	1471.2	0.0004	1561.8	0.0004	0.0010	0.0068	1.0000	2187.4	0.0124	2247.7	0.0043	2333.3	2404.8
PES013144	Porphyritic basaltic andesite	Siderite	Chlorite-FeMg	Montmorillonite	1397.8	0.0099	NULL	NULL	1544.8	0.0007	0.0007	0.0099	1.0000	2192.0	0.0094	2250.7	0.0102	2334.0	2394.8

PES013145	Porphyritic basaltic andesite	NULL	NULL	NULL	1397.1	0.0075	NULL	NULL	1559.1	0.0002	0.0009	0.0052	1.0000	2189.6	0.0107	2249.3	0.0075	2330.1	2389.3
PES013146	Porphyritic basaltic andesite	NULL	NULL	NULL	1396.9	0.0076	NULL	NULL	1561.3	0.0005	0.0009	0.0111	1.0010	2183.4	0.0124	2251.1	0.0023	2322.2	2391.4
PES013147	Porphyritic basaltic andesite	NULL	NULL	NULL	1397.7	0.0063	1469.4	0.0001	1562.3	0.0004	0.0008	0.0090	1.0000	2189.1	0.0116	2248.1	0.0046	2326.7	2391.3
PES013148	Porphyritic diorite	Siderite	Montmorillonite	Chlorite-FeMg	1400.0	0.0149	1461.3	0.0005	1560.8	0.0005	0.0007	0.0297	1.0000	2197.1	0.0127	2250.3	0.0090	2327.2	2392.6

4.5.2. Short-wave infrared (SWIR) spectroscopy and whole-rock major element gains and losses

In total, 120 samples were analysed for hydrothermal alteration minerals using SWIR spectroscopy. Of these samples, 102 provided spectral data, 91 of which had identifiable hydrothermal minerals, while 11 samples were aspectral (Table 4). Of the 91 samples, 8 contained chlorite, 3 kaolinite, 40 muscovite, 9 muscovite-chlorite, 2 muscovite-kaolinite, 3 pyrophyllite, 23 smectite, and 3 tourmaline. Silicified ridges and intrusive units near hydrothermally active zones showed clear depletion in mobile elements (e.g. Ti, Al, Mg, Ca, Na, P, and Fe). The aspectral samples mostly represent the porphyritic basaltic andesites and ignimbrites above the intrusive bodies. Most of these samples probably represent weak propylitic alteration, as was observed in the field.

Muscovite-bearing samples (Figure 24 a. and Figure 38 c.) were confined to silicified ridges, magmatic-hydrothermal breccias, and the main ENE-WSW-oriented major fault structure. The muscovite-bearing samples, which characterize the sericitic alteration zone, were only confined to narrow or otherwise limited areas and were encompassed by either propylitic, advanced argillic, or intermediate argillic alteration. Samples bearing muscovite-chlorite were confined to the creek and were deducted to represent the deeper sericitic alteration zone (sericite-chlorite alteration zone as defined by (Sillitoe 2010). The observed tourmaline-bearing samples were indeed related to magmatic-hydrothermal breccias and occurred in the same areas where sericitic alteration occurred.

Pyrophyllite is diagnostic of deep, high-temperature parts of lithocaps, or it can be an alteration product of dumortierite, which was observed near the kaolinite and pyrophyllite samples in elevated areas. Pyrophyllite typically forms from low-pH fluids reacting with rocks. It forms at temperatures intermediate between those necessary for kaolinite and andalusite (~200-350°c) and is therefore diagnostic of deep parts of some high-sulfidation epithermal deposits and shallow parts of some porphyry Cu systems. The presence of pyrophyllite most likely indicates early alteration e.g. advanced argillic alteration or surficial acid-leach zones above boiling geothermal systems.

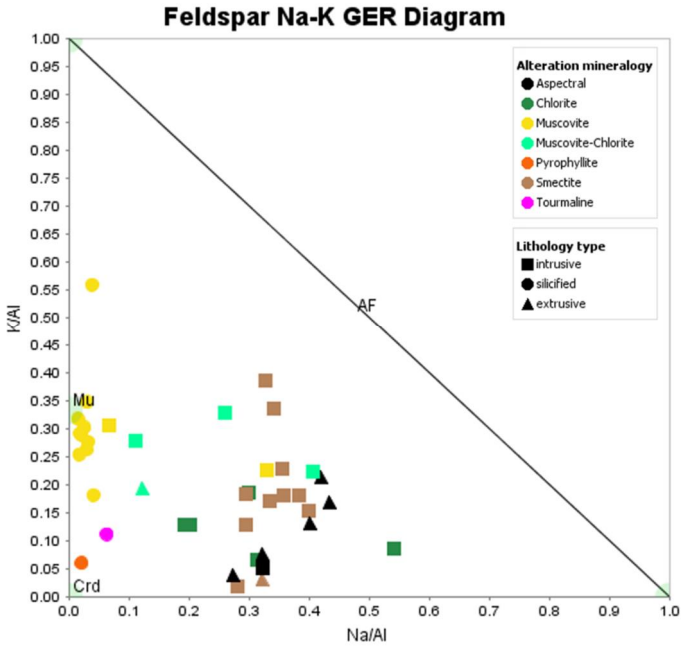

Figure 41: Feldspar Na-K diagram correlating SWIR analysis results with whole-rock geochemical assay results.

A characteristic pyrite halo (Figure 3) was identified at Ronaldo in the form of rather consistent disseminated pyrite in extrusive and intrusive rocks. Other characteristic features for pyrite halos related to lithocaps were elevated concentrations of Zn, Pb, and Mn (Cooke et al. 2017), which were all relatively elevated at Ronaldo. Mn values were especially elevated in the magmatic-hydrothermal breccia containing intermediate-sulfidation epithermal and PCD-style veins.

The integration of SWIR data with whole-rock geochemical data gives some insight into how well the data sets correlate (Figure 41). Combining the data sets works quite well since rocks subjected to different alteration types and intensities should show correlation between gains and losses of mobile trace elements and the mineralogy produced by the alteration. In Figure 41 one can see that the alteration mineralogy correlates quite well with the whole-rock geochemical assay results. Intrusive units represent the majority of smectite altered rocks, and silicified ridges represent the majority of sericite altered rocks, whereas the extrusive rocks are either unaltered or represent propylitic alteration. Thus, one can conclude that both data sets infer similar types of alteration quite well. There were some differences in the data sets, such as two intrusive samples with high K/Al values only displaying smectite alteration. One could

presume these samples to display at least some incipient K-silicate alteration. There was also quite a significant spread in Na/Al values for intrusive samples displaying chlorite and muscovite-chlorite alteration. It is noteworthy that only a few samples seem to display chlorite, although many rocks were observed to host both chlorite and epidote in the field. Also, some of the extrusive aspectral samples displayed compositions closer to weakly altered intrusive samples than to basaltic-andesitic samples.

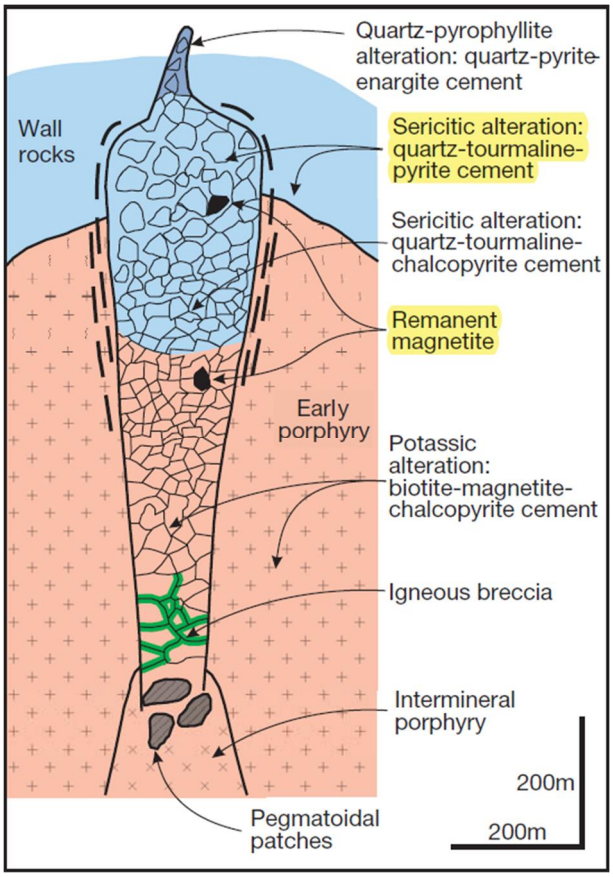

Figure 42: Model of remnant magnetite in magmatic-hydrothermal breccia, after Sillitoe 2010.

Table 5: Summary of sample information, rock type, and alteration zonation as well as qualitative and quantitative analyses performed on each sample.

Observation	Sample*	Easting	Northing	Elevation	Rock Type	Alteration Zonation	Thin Section Lithological Classification	Geochemistry Lithological Classification	Hydrothermal Alteration Mineralogy
RONJG001	PES011227	449512	8533402	4421	Porphyritic basaltic andesite	Unknown	Plagioclase-phyric basaltic andesite	Basaltic andesitic	Other/Null
RONJG002	n.a.	449533	8533341	4434	Porphyritic basaltic andesite	Unknown	n.a.	n.a.	n.a.
RONJG003	PES011228	449596	8533323	4434	Magmatic-hydrothermal breccia	Advanced Argillic	n.a.	n.a.	Pyrophyllite
RONJG004	n.a.	449616	8533229	4423	Magmatic-hydrothermal breccia	Unknown	n.a.	n.a.	n.a.
RONJG005	PES011229	449605	8532747	4399	Porphyritic basaltic andesite	Unknown	n.a.	Basaltic andesitic	Other/Null
RONJG006	PES011230	449340	8532532	4371	Diorite	Least altered	n.a.	Dacitic altered	Aspectral
RONJG007	n.a.	449269	8532421	4352	Diorite	Intermediate Argillic and Sericitic	n.a.	n.a.	n.a.
RONJG008	PES011231 and PES011232	449114	8532369	4325	Porphyritic diorite		Plagioclase-phyric diorite	Dacitic	Smectite and Muscovite

RONJG009	PES011233	445875	8532044	4222	Porphyritic basaltic andesite	Propylitic	Plagioclase-phyric basaltic andesite and aplitic dyke	Basaltic andesitic	Chlorite
RONJG010	PES011234	445850	8531994	4200	Basaltic andesite	Unknown	n.a.	n.a.	Other/Null
RONJG011	PES011235	446006	8531855	4255	Diorite	Unknown	n.a.	n.a.	Other/Null
RONJG012	PES011236	445998	8531796	4245	Basaltic andesite	Unknown	n.a.	n.a.	Other/Null
RONJG013	PES011237	446130	8531555	4193	Porphyritic basaltic andesite	Least altered	Plagioclase-phyric basaltic andesite	Basaltic andesitic	Aspectral
RONJG014	PES011238	446198	8531502	4164	Diorite	Unknown	n.a.	n.a.	Other/Null
RONJG015	PES011239	446254	8531411	4114	Basaltic andesite	Unknown	n.a.	n.a.	Other/Null
RONJG016	PES011240	446440	8531194	4006	Silicified ridge	Sericitic	n.a.	Silicified	Muscovite
RONJG017	PES011241	446420	8531151	3960	Porphyritic granodiorite	Sericitic	Plagioclase-phyric granodiorite	Rhyolitic	Muscovite
RONJG018	n.a.	446532	8531195	3975	Porphyritic granodiorite	Unknown	n.a.	n.a.	n.a.
RONJG019	PES011242	446575	8531211	3988	Porphyritic granodiorite	Sericitic	n.a.	n.a.	Muscovite
RONJG020	PES011243	446648	8531223	3999	Porphyritic granodiorite	Intermediate Argillic	n.a.	Rhyolitic	Smectite
RONJG021	PES011244	446728	8531243	4017	Igneous breccia	Unknown	n.a.	n.a.	Other/Null

RONJG022	PES011245	446758	8531264	4019	Porphyritic diorite	Unknown	n.a.	n.a.	Other/Null
RONJG023	PES011246 and PES011247 (and D21-001)	446787	8531260	4019	Silicified ridge and Porphyritic diorite	Sericitic and Propylitic	n.a.	Silicified and Dacitic	Muscovite and Chlorite
RONJG024	PES011248 and PES011249	448288	8531681	4212	Porphyritic diorite	Propylitic	K-feldspar-phyric granodiorite	Andesitic altered	Chlorite
RONJG025	PES011250	448260	8531656	4211	Porphyritic basaltic andesite	Unknown	n.a.	Basaltic andesitic	Other/Null
RONJG026	PES011251	448147	8531624	4190	Porphyritic diorite	Sericite-chlorite	Plagioclase-phyric diorite	Dacitic altered	Muscovite-Chlorite
RONJG027	PES011252 (and D21-002)	448096	8531635	4190	Diorite	Sericitic	n.a.	Silicified	Muscovite
RONJG028	PES011253 and PES011254 and PES011270	448013	8531627	4169	Diorite	Sericite-chlorite and Sericitic	n.a.	Silicified	Muscovite-Chlorite and Muscovite
RONJG029	PES011255	447945	8531570	4155	Basaltic andesite	Least altered	n.a.	n.a.	Aspectral
RONJG030	n.a.	447882	8531564	4150	Diorite		n.a.	n.a.	n.a.
RONJG031	PES011256	447832	8531566	4145	Diorite	Least altered	n.a.	Dacitic altered	Aspectral
RONJG032	PES011257	447761	8531563	4140	Magmatic-hydrothermal breccia	Sericitic	n.a.	n.a.	Muscovite

RONJG033	PES011258 and PES011259 and PES011260 and PES011261 (and D21-003 D21-006)	447714	8531553	4137	Magmatic-hydrothermal breccia	Propylitic and Intermediate Argillic	n.a.	Dacitic altered and Andesitic altered	Chlorite and Smectite
RONJG034	n.a.	447675	8531553	4138	Magmatic-hydrothermal breccia	Unknown	n.a.	n.a.	n.a.
RONJG035	PES011262	447576	8531507	4116	Magmatic-hydrothermal breccia	Sericite-chlorite	n.a.	n.a.	Muscovite-Chlorite
RONJG036	n.a.	447524	8531482	4110	Porphyritic granodiorite	Unknown	n.a.	n.a.	n.a.
RONJG037	PES011263 (and D21-007)	447413	8531441	4094	Porphyritic granodiorite	Sericite-chlorite	Plagioclase-phyric granodiorite	Rhyolitic	Muscovite-Chlorite
RONJG038	PES011264 and PES011265	447263	8531429	4080	Porphyritic granodiorite	Sericitic	n.a.	n.a.	Muscovite
RONJG039	PES011266	447118	8531394	4070	Porphyritic granodiorite	Intermediate Argillic	Plagioclase-phyric granodiorite	Rhyolitic	Smectite
RONJG040	PES011267	446918	8531308	4042	Porphyritic granodiorite	Sericitic	n.a.	n.a.	Muscovite
RONJG041	PES011268	446882	8531190	4059	Porphyritic granodiorite	Unknown	n.a.	n.a.	Other/Null
RONJG042	PES011269	446917	8531089	4090	Porphyritic granodiorite	Unknown	n.a.	n.a.	Other/Null

RONJG043	PES011271	448425	8533110	4445	Porphyritic basaltic andesite	Unknown	n.a.	n.a.	Other/Null
RONJG044	PES011272 and PES011273	448359	8532976	4450	Porphyritic basaltic andesite	Advanced Argillic	n.a.	n.a.	Muscovite-Kaolinite and Kaolinite
RONJG045	PES011274	448330	8532885	4453	Porphyritic basaltic andesite	Unknown	Plagioclase-phyric basaltic andesite	n.a.	Other/Null
RONJG046	PES011275	448371	8532821	4442	Porphyritic basaltic andesite	Advanced Argillic	n.a.	n.a.	Kaolinite
RONJG047	PES011276	448405	8532711	4425	Silicified ridge	Sericitic	n.a.	n.a.	Muscovite
RONJG048	PES011277	448525	8531513	4283	Silicified ridge	Sericitic	n.a.	n.a.	Muscovite
RONJG049	PES011279	448549	8532515	4378	Porphyritic basaltic andesite	Intermediate Argillic	Plagioclase-phyric basaltic andesite	Basaltic andesitic	Smectite
RONJG050	PES011278 (and D21-008)	448436	8532465	4381	Silicified ridge	Sericitic	n.a.	Silicified	Tourmaline
RONJG051	PES011280	448099	8532950	4423	Porphyritic basaltic andesite	Unknown	n.a.	n.a.	Other/Null
RONJG052	PES011281	447992	8532856	4417	Porphyritic basaltic andesite	Sericitic	n.a.	n.a.	Muscovite
RONJG053	n.a.	447687	8532892	4441	Porphyritic basaltic andesite	Unknown	n.a.	n.a.	n.a.

RONJG054	PES011283	447650	8532922	4448	Silicified ridge	Sericitic	n.a.	n.a.	Muscovite
RONJG055	n.a.	447627	8532933	4451	Porphyritic basaltic andesite	Unknown	n.a.	n.a.	n.a.
RONJG056	PES011282	447605	8532939	4454	Porphyritic basaltic andesite	Unknown	n.a.	n.a.	Other/Null
RONJG057	n.a.	447573	8532939	4458	Porphyritic basaltic andesite	Unknown	n.a.	n.a.	n.a.
RONJG058	n.a.	447584	8532753	4423	Porphyritic basaltic andesite	Unknown	n.a.	n.a.	n.a.
RONJG059	n.a.	447710	8532884	4442	Silicified ridge	Unknown	n.a.	n.a.	n.a.
RONJG060	PES011284	447730	8532862	4438	Igneous breccia	Unknown	n.a.	n.a.	Other/Null
RONJG061	PES011285 and PES011286	447741	8532852	4433	Porphyritic diorite	Intermediate Argillic and Advanced Argillic	n.a.	Dacitic	Smectite and Kaolinite
RONJG062	n.a.	447817	8532788	4420	Basaltic andesite	Unknown	n.a.	n.a.	n.a.
RONJG063	PES011287	447912	8531651	4393	Igneous breccia	Intermediate Argillic	n.a.	n.a.	Smectite
RONJG064	PES011288 and PES011289 (and D21-009)	447927	8532619	4390	Porphyritic diorite	Sericitic	Plagioclase-phyric diorite	Dacitic	Muscovite

RONJG065	PES011290	448214	8532402	4361	Silicified ridge	Advanced Argillic	n.a.	Silicified	Pyrophyllite
RONJG066	PES011291	449406	8531762	4350	Silicified ridge	Sericitic	n.a.	n.a.	Muscovite
RONJG067	n.a.	449501	8531653	4391	Silicified ridge	Unknown	n.a.	n.a.	n.a.
RONJG068	PES011292 and PES011293	449560	8531611	4410	Ignimbrite	Sericite-chlorite	n.a.	Andesitic altered	Muscovite-Chlorite
RONJG069	n.a.	449591	8531548	4425	Basaltic andesite	Unknown	n.a.	n.a.	n.a.
RONJG070	PES011294	449614	8531537	4429	Porphyritic diorite	Unknown	n.a.	n.a.	Other/Null
RONJG071	n.a.	449621	8531487	4439	Basaltic andesite	Unknown	n.a.	n.a.	n.a.
RONJG072	n.a.	449619	8531430	4450	Porphyritic diorite	Unknown	n.a.	n.a.	n.a.
RONJG073	n.a.	449522	8531379	4449	Basaltic andesite	Unknown	n.a.	n.a.	n.a.
RONJG074	PES011295	449446	8531333	4444	Silicified ridge	Sericitic	n.a.	n.a.	Muscovite
RONJG075	PES011296	449309	8531299	4423	Diorite	Unknown	n.a.	n.a.	Other/Null
RONJG076	n.a.	449249	8531304	4015	Ignimbrite	Unknown	n.a.	n.a.	n.a.
RONJG077	n.a.	449189	8531306	4406	Basaltic andesite	Unknown	n.a.	n.a.	n.a.
RONJG078	PES011297	449118	8531322	4397	Diorite	Unknown	n.a.	n.a.	Other/Null
RONJG079	PES011298	449067	8531315	4391	Diorite	Unknown	n.a.	n.a.	Other/Null
RONJG080	PES013101	449072	8532317	4216	Porphyritic diorite	Sericitic	n.a.	n.a.	Muscovite
RONJG081	PES013102 and PES013124	449037	8532218	4307	Porphyritic diorite	Intermediate Argillic	Plagioclase-phyric granodiorite	Dacitic	Smectite

RONJG082	n.a.	449029	8532188	4302	Porphyritic diorite	Unknown	n.a.	n.a.	n.a.
RONJG083	n.a.	448995	8532148	4296	Basaltic andesite	Unknown	n.a.	n.a.	n.a.
RONJG084	PES013103	448971	8532074	4284	Ignimbrite	Sericite-chlorite	n.a.	n.a.	Muscovite-Chlorite
RONJG085	PES013104	448826	8531961	4267	Porphyritic basaltic andesite	Intermediate Argillic	Plagioclase-phyric basaltic andesite	Basaltic andesitic	Smectite
RONJG086	PES013105	448803	8531946	4261	Magmatic-hydrothermal breccia	Sericitic	n.a.	n.a.	Muscovite
RONJG087	n.a.	448774	8531931	4262	Basaltic andesite	Unknown	n.a.	n.a.	n.a.
RONJG088	PES013106	448526	8531772	4234	Basaltic andesite	Intermediate Argillic	Microcrystaline basaltic andesite	Silicified	Smectite
RONJG089	PES013107	448492	8531730	4230	Magmatic-hydrothermal breccia	Sericitic	n.a.	n.a.	Tourmaline
RONJG090	PES013108	448455	8531718	4223	Basaltic andesite	Propylitic	n.a.	n.a.	Chlorite
RONJG091	PES013109	448386	8531707	4218	Porphyritic basaltic andesite	Unknown	Plagioclase-phyric basaltic andesite	Basaltic andesitic	Other/Null
RONJG092	PES013110 and PES013111 and PES013112	448336	8531701	4216	Porphyritic basaltic andesite	Least altered	n.a.	Andesitic altered	Aspectral

	(and D21-010 and D21-011)								
RONJG093	n.a.	448489	8532678	4345	Basaltic andesite	Unknown	n.a.	n.a.	n.a.
RONJG094	PES013113 and PES013122 (and D21-012)	448443	8532648	4377	Silicified ridge	Sericitic	n.a.	Silicified	Muscovite
RONJG095	PES013114	448388	8532708	4411	Silicified ridge	Sericitic	n.a.	n.a.	Muscovite
RONJG096	n.a.	448517	8532537	4386	Silicified ridge	Unknown	n.a.	n.a.	n.a.
RONJG097	PES013115 and PES013116 (and D21-013)	448512	8532509	4380	Silicified ridge	Sericitic	n.a.	Silicified	Muscovite
RONJG098	n.a.	448487	8532485	4385	Silicified ridge	Unknown	n.a.	n.a.	n.a.
RONJG099	PES013117 and PES013123 (and D21-014)	448463	8532472	4380	Silicified ridge	Sericitic	n.a.	Silicified	Muscovite
RONJG100	n.a.	448397	8532442	4381	Silicified ridge	Unknown	n.a.	n.a.	n.a.
RONJG101	PES013118	448315	8532323	4363	Magmatic-hydrothermal breccia	Sericitic	n.a.	n.a.	Tourmaline
RONJG102	n.a.	448400	8532357	4365	Magmatic-hydrothermal breccia	Unknown	n.a.	n.a.	n.a.
RONJG103	n.a.	448425	8532268	4345	Silicified ridge	Unknown	n.a.	n.a.	n.a.
RONJG104	n.a.	448446	8532226	4331	Magmatic-hydrothermal breccia	Unknown	n.a.	n.a.	n.a.

RONJG105	PES013119	448247	8532108	4310	Magmatic-hydrothermal breccia	Sericitic	n.a.	n.a.	Muscovite
RONJG106	n.a.	448427	8532079	4306	Diorite	Unknown	n.a.	n.a.	n.a.
RONJG107	n.a.	448441	8531971	4283	Silicified ridge	Unknown	n.a.	n.a.	n.a.
RONJG108	n.a.	448344	8531855	4264	Basaltic andesite	Unknown	n.a.	n.a.	n.a.
RONJG109	n.a.	448311	8531817	4260	Porphyritic diorite	Unknown	n.a.	n.a.	n.a.
RONJG110	PES013120 and PES013121 (and D21-015)	448381	8531795	4256	Porphyritic basaltic andesite	Unknown	n.a.	Andesitic altered	Other/Null
RONJG111	PES013125 and PES013126	448491	8531901	4249	Porphyritic basaltic andesite	Least altered	Plagioclase-phyric basaltic andesite	Basaltic andesitic	Aspectral
RONJG112	PES013127 and PES013128	449127	8531613	4327	Porphyritic diorite	Intermediate Argillic	Plagioclase-phyric diorite	Dacitic	Smectite
RONJG113	PES013129	449203	8531524	4356	Ignimbrite	Least altered	n.a.	n.a.	Aspectral
RONJG114	PES013130	449206	8531472	4376	Ignimbrite	Sericitic	n.a.	n.a.	Muscovite
RONJG115	n.a.	449243	8531438	4390	Silicified ridge	Unknown	n.a.	n.a.	n.a.
RONJG116	n.a.	449263	8531406	4401	Diorite	Unknown	n.a.	n.a.	n.a.
RONJG117	PES013131	449330	8531410	4410	Silicified ridge	Sericitic	n.a.	Silicified	Muscovite
RONJG118	n.a.	449309	8531357	4417	Diorite	Unknown	n.a.	n.a.	n.a.
RONJG119	n.a.	449138	8531435	4375	Porphyritic diorite	Unknown	n.a.	n.a.	n.a.
RONJG120	PES013132 and PES013133 (and D21-016)	449107	8531470	4358	Silicified ridge	Sericitic	n.a.	Silicified	Muscovite

RONJG121	PES013134	449021	8531446	4356	Porphyritic diorite	Unknown	n.a.	n.a.	Other/Null
RONJG122	PES013135 and PES013136 and PES013137 (and D21-017)	448851	8531472	4329	Silicified ridge	Sericitic	n.a.	Silicified	Muscovite
RONJG123	PES013138 and PES013139	448817	8531510	4312	Ignimbrite	Sericitic and Advanced Argillic	n.a.	n.a.	Muscovite and Muscovite-Kaolinite
RONJG124	PES013140 and PES013141 (and D21-018)	448800	8531430	4321	Silicified ridge	Sericitic	n.a.	Silicified	Muscovite
RONJG125	n.a.	450993	8532812	4363	Basaltic andesite	Unknown	n.a.	n.a.	n.a.
RONJG126	n.a.	451064	8532651	4472	Porphyritic basaltic andesite	Unknown	n.a.	n.a.	n.a.
RONJG127	n.a.	450958	8532373	4488	Ignimbrite	Unknown	n.a.	n.a.	n.a.
RONJG128	n.a.	450899	8532099	4503	Ignimbrite	Unknown	n.a.	n.a.	n.a.
RONJG129	n.a.	450868	8531947	4504	Ignimbrite	Unknown	n.a.	n.a.	n.a.
RONJG130	n.a.	450843	8531894	4505	Ignimbrite	Unknown	n.a.	n.a.	n.a.
RONJG131	n.a.	450771	8531811	4506	Ignimbrite	Unknown	n.a.	n.a.	n.a.
RONJG132	PES013142 and PES013143	450591	8531667	4518	Ignimbrite	Least altered	n.a.	Andesitic altered	Aspectral
RONJG133	n.a.	450371	8531217	4505	Porphyritic basaltic andesite	Unknown	n.a.	n.a.	n.a.

RONJG134	PES013144 and PES013145	450180	8530890	4472	Porphyritic basaltic andesite	Propylitic	Plagioclase-phyric basaltic andesite	Basaltic andesitic	Chlorite
RONJG135	n.a.	450005	8530681	4472	Porphyritic basaltic andesite	Unknown	n.a.	n.a.	n.a.
RONJG136	n.a.	449950	8530600	4475	Porphyritic basaltic andesite	Unknown	n.a.	n.a.	n.a.
RONJG137	n.a.	449860	8530428	4486	Porphyritic basaltic andesite	Unknown	n.a.	n.a.	n.a.
RONJG138	n.a.	449504	8530227	4490	Porphyritic basaltic andesite	Unknown	n.a.	n.a.	n.a.
RONJG139	n.a.	449346	8530304	4474	Porphyritic basaltic andesite	Unknown	n.a.	n.a.	n.a.
RONJG140	PES013146 and PES013147	449061	8530244	4468	Porphyritic basaltic andesite	Unknown	Plagioclase-phyric basaltic andesite and aplitic dyke	Basaltic andesitic	Other/Null
RONJG141	n.a.	448956	8530164	4461	Diorite	Unknown	n.a.	n.a.	n.a.
RONJG142	n.a.	448545	8530212	4419	Ignimbrite	Unknown	n.a.	n.a.	n.a.
RONJG143	PES013148	448238	8530251	4391	Porphyritic diorite	Intermediate Argillic	n.a.	Dacitic	Smectite
RONJG144	n.a.	447779	8530443	4375	Basaltic andesite	Unknown	n.a.	n.a.	n.a.

RONJG145	n.a.	447591	8530559	4331	Silicified ridge	Unknown	n.a.	n.a.	n.a.
RONJG146	n.a.	447541	8530598	4312	Porphyritic basaltic andesite	Unknown	n.a.	n.a.	n.a.
RONJG147	n.a.	447503	8530651	4293	Diorite	Unknown	n.a.	n.a.	n.a.
RONJG148	n.a.	447487	8530746	4268	Diorite	Unknown	n.a.	n.a.	n.a.
RONJG149	n.a.	447334	8530866	4228	Porphyritic basaltic andesite	Unknown	n.a.	n.a.	n.a.
RONJG150	n.a.	447232	8530881	4214	Porphyritic basaltic andesite	Unknown	n.a.	n.a.	n.a.
RONJG151	n.a.	447036	8530960	4165	Basaltic andesite	Unknown	n.a.	n.a.	n.a.
RONJG152	n.a.	446895	8531020	4117	Porphyritic basaltic andesite	Unknown	n.a.	n.a.	n.a.
RONJG153	n.a.	446789	8531105	4077	Diorite	Unknown	n.a.	n.a.	n.a.
RONJG154	n.a.	446574	8531136	4020	Porphyritic diorite	Unknown	n.a.	n.a.	n.a.

Note: n.a. = not analysed, * = includes both lithogeochemical assay and thin section codes

4.6. Metal endowment

In some cases, there was a clear correlation between metal endowment, silica content, and alteration. Silver was clearly concentrated in samples displaying high silica content and sericitic alteration (Figure 43), as was gold (Figure 44) and molybdenum (Figure 45). Such a correlation was not observed for copper since the whole-rock geochemical assay results showed consistently low concentrations of copper regardless of silica content or alteration type (Figure 46).

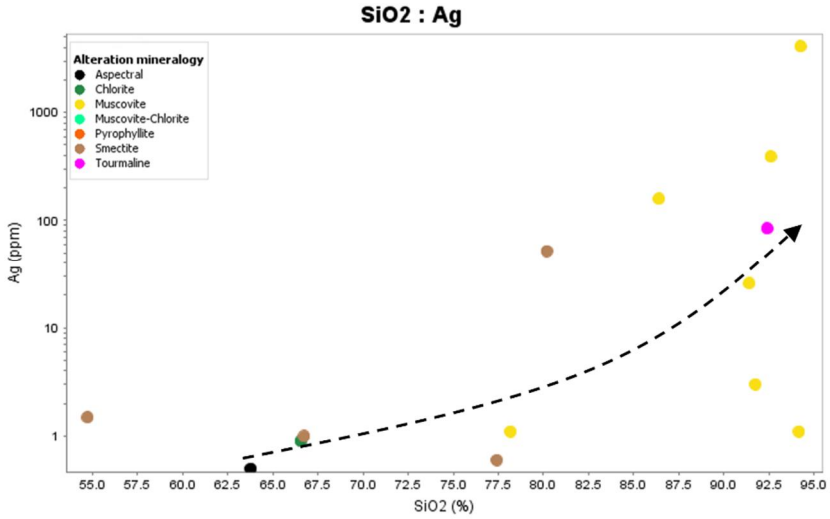

Figure 43: Logarithmic scale displaying Ag correlation with hydrothermal alteration mineralogy. The arrow indicates the general trend of concentration.

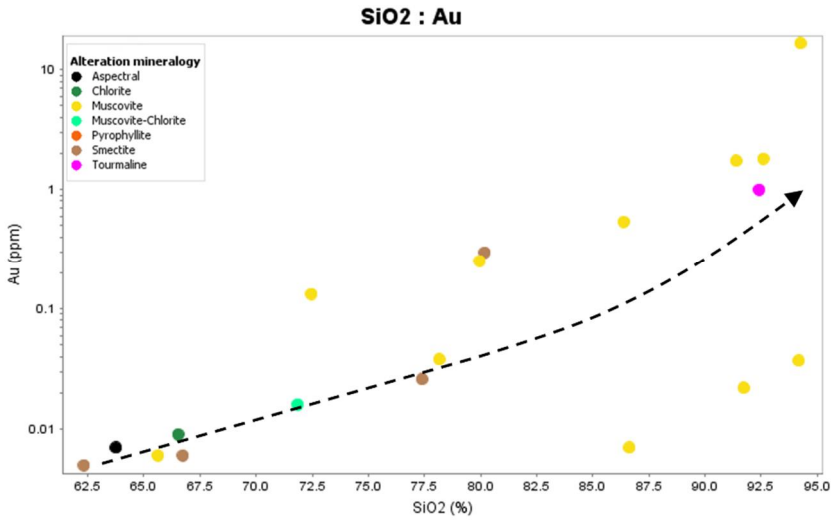

Figure 44: Logarithmic scale displaying Au correlation with hydrothermal alteration mineralogy. The arrow indicates the general trend of concentration.

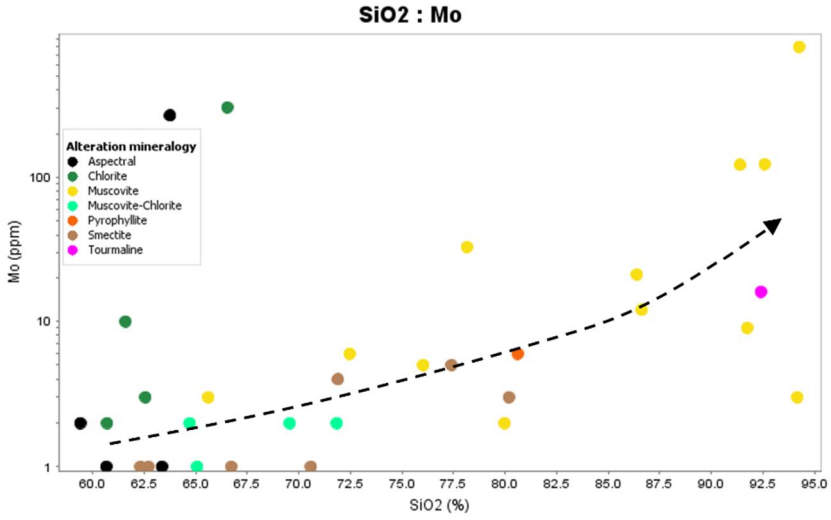

Figure 45: Logarithmic scale displaying Mo correlation with hydrothermal alteration mineralogy. The arrow indicates the general trend of concentration.

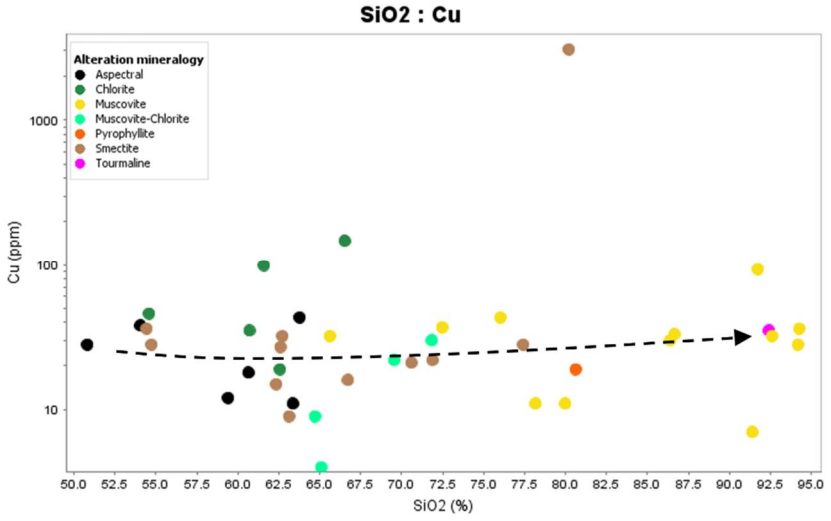

Figure 46: Logarithmic scale displaying Cu correlation with hydrothermal alteration mineralogy. The arrow indicates the general trend of concentration.

4.7. Trace element footprint

Samples with <70 wt. % SiO_2 were selected to capture the background trace element values, while samples were ignored that had abundant vein material capable of contaminating the background value results. Typical pathfinder element ranges related to porphyry Cu systems were obtained from Halley et al. 2015 that are meant to highlight enrichments of at least three times the average background values of continental crust rocks.

Trace elements that displayed elevated values in the study area include Mo, Pb, Ag, Co, Te, Bi, As, Sb, Cs, and, to a lesser extent, Li and Tl. Of these trace elements, Mo, As, Sb, Te, and Bi represent non-leachable chalcophile elements. Before weathering, these elements are trapped as trace impurities in pyrite or minute sulfide grains associated with pyrite (Halley et al. 2015). The aforementioned chalcophile elements are useful magmatic tracers since they are only weakly affected by leaching and weathering (Figure 47). Lithophile elements such as W and Sn did not display elevated values at Ronaldo. Lithophile alkali and alkali earth elements such as Li and Tl displayed only slightly elevated values, while Cs values were anomalously elevated at Ronaldo.

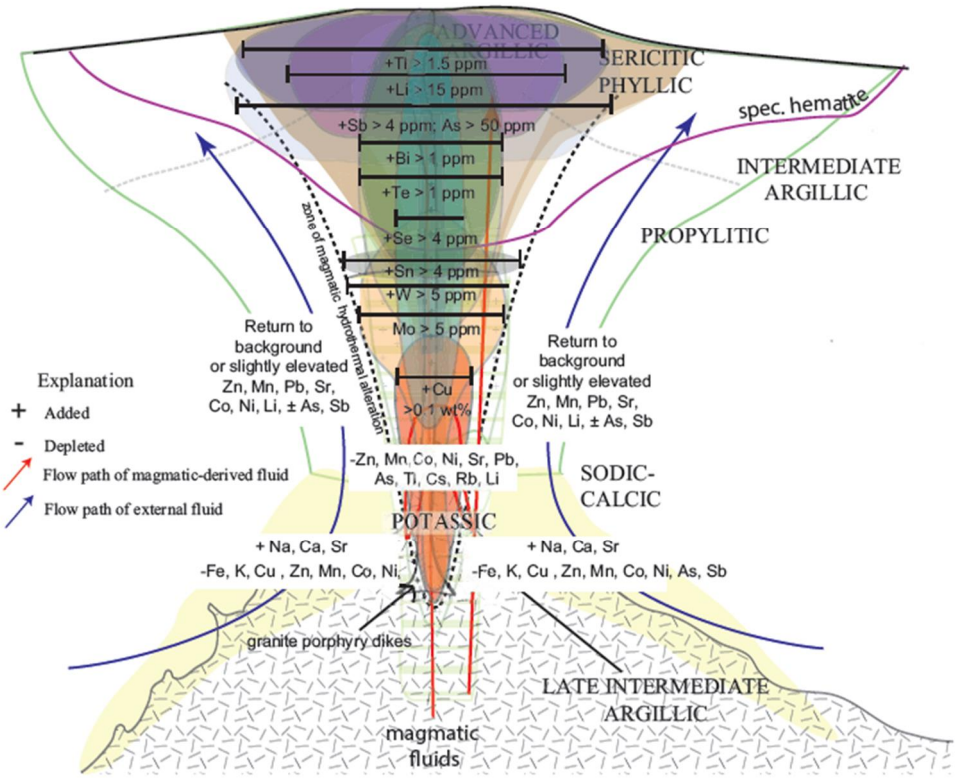

Figure 47: Trace element footprint map, after Halley et al. 2015.

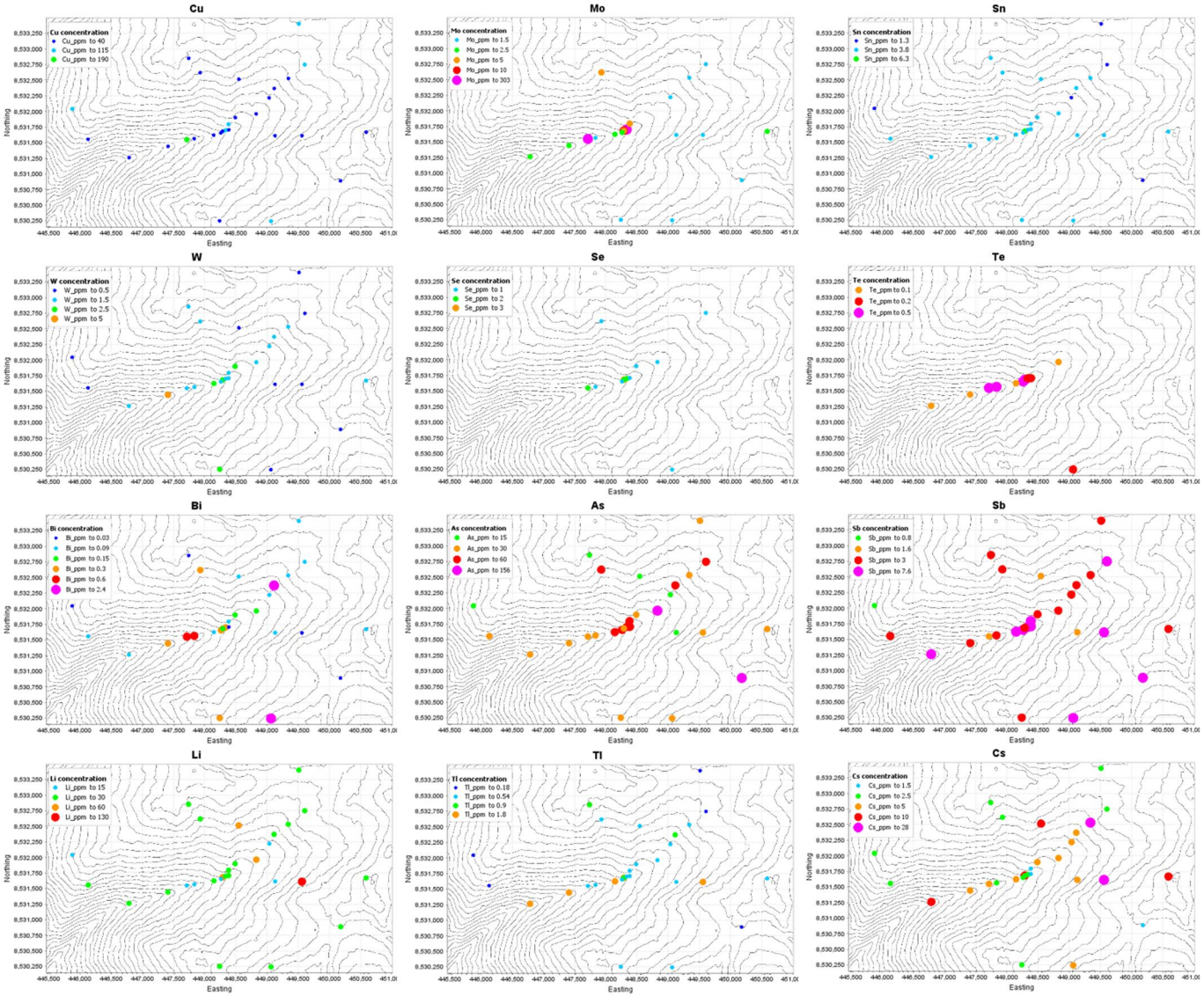

Figure 48: Spatial map of immobile trace element distribution at Ronaldo, based on threshold values obtained from Halley et al. 2015.

Of all trace elements with elevated values, Mo and Te occurred in a rather confined area in the creek, while Pb, Ag, Co, Bi, As, Sb, Li, and Tl displayed the effects of a wider alteration halo (Figure 48).

The concentrations of trace elements such as Cu, Mo, W, Zn, Pb, Te, Bi, and Li pointed toward a shallow sericitic alteration zone, while the concentrations of Ni, Co, As, Sb, Tl, and Hg were more in line with those typical of a deep sericitic alteration zone. The results for trace elements such as Sn, Mn, Ag, Se, and Cs cannot be interpreted to belong to either the shallow or deep sericitic alteration zone (Halley et al. 2015). With evidence pointing towards both the shallow and deep sericitic alteration zones and for an abundance of indifferent trace elements, it seems that Ronaldo displays a transition between the two zones. The trace elements that were most clearly anomalously elevated from background values were the chalcophile elements As, Sb, Te, and Bi, which are, as previously disclosed, divided 1:1 in indicating shallow and deep sericitic alteration zones. Elements such as Te, Bi, As, and Sb are precipitated as sulfide, oxide, and silicate minerals, reflecting the declining temperature of the acidic fluid that rose from the porphyry stock.

At Ronaldo, the sericitic alteration is confined to the silicified ridges that are interpreted to have functioned as fluid conduits for the lithocap. The trace element evidence of sericitic alteration is therefore limited to these feeder zones and does not conform with a widespread background alteration zone as typically developed above PCDs elsewhere. The observed trace element zonation also indicates anomalies typical of transition into an advance argillic alteration zone in the shallow parts of a porphyry Cu system. The trace element concentrations suggest that Ronaldo is spatially situated in a vertical porphyry Cu system in transition between a deep and a shallow sericitic alteration zone (Figure 47). This interpretation is in conformity with the SWIR analysis results that indicate muscovite especially in the silicified ridges.

5. DISCUSSION

5.1. Geologic evolution and alteration history

The age relationships between the different lithological units in the prospect are as follows: Sacsaquero Formation porphyritic basaltic andesites and ignimbrites are the oldest unit in the area and are intruded by lower Miocene porphyritic diorite and porphyritic granodiorite intrusions. Due to extensive erosion that has affected the area, the extrusive units are at times only observed as roof pendants (Figure 21 e.), and the tops of the intrusive units are exposed below them. The occurrence of hornfels also supports this hypothesis since it formed through contact metamorphism of the volcanic wall rock by heat from the intrusive bodies. The porphyritic diorite intrusion (19.95±0.77 Ma U-Pb in zircons) is younger than the porphyritic granodiorite intrusion (21.29±0.52 Ma U-Pb in zircons) (Table 2) and is either contemporaneous with or younger than the diorite dikes that crosscut the porphyritic granodiorite intrusion. The two intrusive units have marked differences in magnetic susceptibility, trace element composition, and petrographic features, such as the presence of amphibole in the porphyritic diorite but not in the porphyritic granodiorite.

Multiple stages of intrusion have occurred at Ronaldo. Some of these events are captured in the igneous breccias (Figure 24 f), which have jigsaw-texture subangular clasts of intrusive and extrusive rocks sitting in an intrusive matrix. The diorite dikes in the porphyritic granodiorite intrusion, as well as the aplitic dikes crosscutting the overlying extrusive units, also support this interpretation.

The Ronaldo prospect has been subjected to a hydrothermally active system that formed – among other features – an advanced argillic-altered lithocap at the very top of the system. Due to erosion, only remnants of the once extensive advanced argillic lithocap remain. The silicified ridges are interpreted in this study to be the steeply dipping fluid conduits of the deep root zone of the lithocap. Waning of the hydrothermal system led to overprinting and possibly even telescoping of the hydrothermal zoning (Figure 49) and to low temperature alteration of the intrusive and adjacent extrusive

units, resulting in intermediate argillic alteration dominated by low-temperature clay minerals such as smectite (Table 4). Sericitic alteration occurs 1) in proximity to the major fault transecting the area, 2) in the silicified ridges, and 3) in the magmatic-hydrothermal breccia. Widespread propylitic alteration surrounds the aforementioned alteration zones and at times overlaps with intermediate argillic alteration (Figure 37).

5.2. Exploration potential

The exploration potential for low-sulfidation epithermal Ag-Au is rather significant since quartz veinlets in silicified ridges throughout the prospect were found to host relatively consistent Ag and Au mineralization and at times even bonanza Ag-Au mineralization in drusy quartz veinlets. The presence of lattice-textured bladed calcite replaced by quartz and the presence of adularia in many samples suggest that boiling occurred, which is a common process operating in conduits at epithermal depths. Boiling is a process that eventually leads to Au and Ag being precipitated from the ore fluid (Henley et al. 1985; Simmons et al. 1994). Illite, an alteration product of adularia, occurs intermittently in the stratified silica veins, suggesting that fluctuations in pH were common during the formation of these veins. Textures typically associated with low-sulfidation epithermal mineralization, such as botryoidal silica, occur in some of the intermediate-sulfidation veins, suggesting that low-sulfidation mineralization was deposited after intermediate-sulfidation mineralization.

Some evidence was found in support of the hypothesis of a concealed at-depth PCD. Such evidence includes 1) widespread (albeit shallow) hydrothermal alteration, 2) local PCD-style veining in the porphyritic diorite intrusion and adjacent magmatic-hydrothermal breccia, 3) biotite and amphibole pseudomorphs hosted in the porphyritic diorite intrusion, which indicate a hydrous parental magma suitable for concentrating porphyry Cu mineralization, 4) basaltic andesite roof pendants, which indicate that the tops of the intrusions are preserved, and 5) locally abundant isolated magnetite aggregates in the magmatic-hydrothermal breccia, which may be indicative of sericitic overprinting of previous potassic alteration (Sillitoe 2010).

Compelling evidence was found that Ronaldo is spatially situated in a typical shallow-depth porphyry-related hydrothermal alteration environment including 1) trace element concentrations (namely Te, Bi, As, and Sb) indicative of a transition from a shallow to a deep sericitic alteration zone, 2) hydrothermal minerals such as pyrophyllite, kaolinite, and dumortierite indicative of the now mostly eroded lithocap, and 3) silicified ridges that are the remnant deep roots of the lithocap. This environment is most likely too shallow to host a concealed PCD.

However, because of evidence that sericitic alteration overprinting potassic alteration occurred at Ronaldo in the magmatic-hydrothermal breccia, it is noteworthy that examples of root zones of advanced argillic lithocaps, such as present at Ronaldo, overprinting the upper parts of PCDs have been identified before (e.g. El Salvador; Gustafson and Hunt 1975). In these upper parts, sericitic alteration is commonly transitional upward to quartz-pyrophyllite, an assemblage widespread in the deep, high temperature parts of many lithocaps (Sillitoe 2010). Deeply eroded lithocaps displaying pyrophyllite ± sericite ± andalusite alteration are the principal target when exploring for PCDs concealed beneath advanced argillic alteration (Sillitoe 2010). Further study of the hydrothermal minerals present in the lithocap at Ronaldo should be implemented since the samples collected for this study may not reveal the true depth and extent of the lithocap.

The alteration that occurs at Ronaldo is not typical of a porphyry Cu environment near to an ore zone and is instead indicative of a shallower epithermal environment. If there were a temporal and spatial connection between the observed epithermal mineralization and a possible concealed at-depth PCD, the epithermal mineralization would need to exhibit high sulfidation, whereas Ronaldo exhibits low-sulfidation epithermal mineralization. This is, as previously explained, because high-sulfidation epithermal mineralization is the only epithermal-style mineralization that has been shown to have temporal and spatial connections with porphyry Cu mineralization (Muntean et al. 2001; Sillitoe et al. 2003). It is unknown whether a mineralized, concealed at-depth PCD exists beneath the root zone of the lithocap at Ronaldo, but this study's observations and analyses suggest that it is unlikely at an economical depth (i.e. less than 1000 m).

The prospect does however show potential for low-sulfidation epithermal mineralization exploration: further studies, especially of the continuity of the silicified ridges, are required to increase understanding of the mineralization at the Ronaldo prospect. To determine the extent of the epithermal mineralization and to gain confidence in the aforementioned hypothesis, a diamond drill campaign should be implemented.

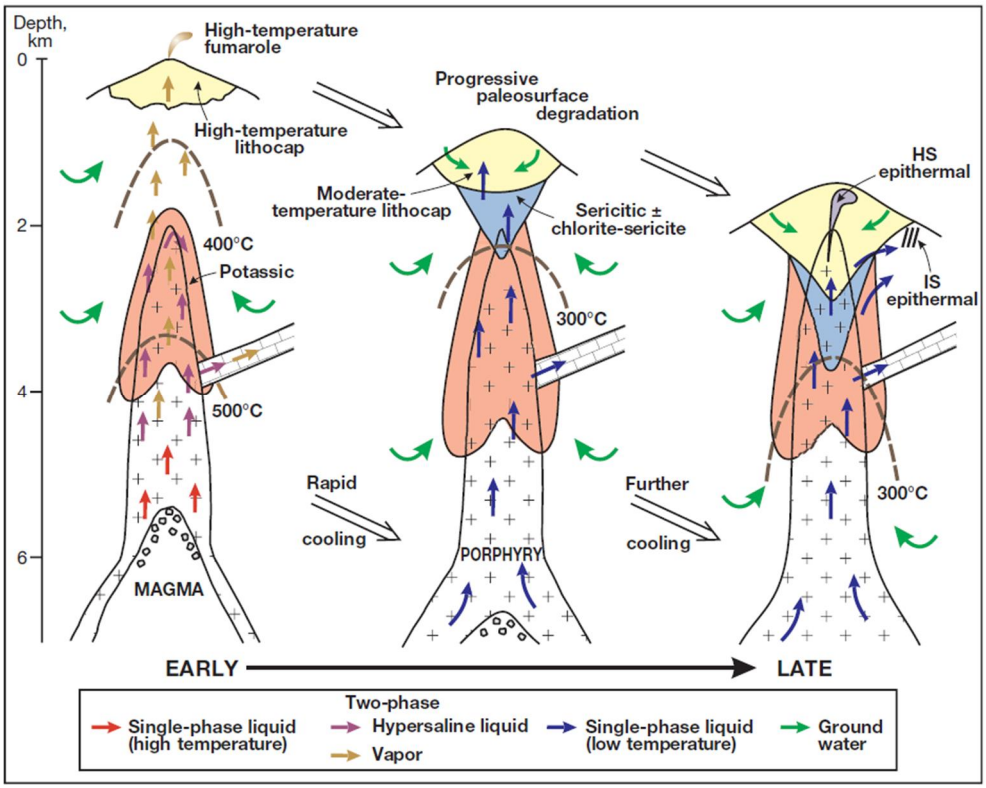

Figure 49: Telescoping model of porphyry Cu systems, after Sillitoe 2010.

6. CONCLUSIONS

The Ronaldo prospect comprises two separate lower Miocene intrusive units – porphyritic diorite and porphyritic granodiorite – intruding overlying late Eocene-Oligocene basaltic andesites and ignimbrites. A unit of magmatic-hydrothermal breccia lies between the two intrusive bodies, which are also crosscut by late silicified ridges. A

creek coinciding with a major sinistral fault transects the tenement, revealing deeper parts of the hydrothermal system. The silicified ridges are interpreted in this study as the roots of a mostly eroded advanced argillic lithocap, for which they functioned as fluid conduits.

The once extensive advanced argillic lithocap has been largely eroded, but deep, high-temperature parts of it remain, exemplified by the presence of pyrophyllite. The colour anomalies observed in satellite imagery at Ronaldo are caused by localized advanced argillic- and widespread intermediate argillic-altered rock. Intrusive rocks and some extrusive rocks have been subjected to widespread intermediate argillic alteration, typified by smectite. Sericitic alteration is focused in the silicified ridges, magmatic-hydrothermal breccia, and in rocks related to the major fault. Trace element concentrations suggest that Ronaldo is mostly situated in a sericitic alteration zone. Extensive distal areas dominated by extrusive units exhibit different degrees of propylitic alteration or are unaltered.

The silicified ridges host epithermal drusy quartz veins, many of which host rather consistent Ag and Au mineralization, some even hosting bonanza Ag-Au mineralization (up to 4100 ppm Ag and 17 ppm Au). The mineralization was determined to be low-sulfidation epithermal due to observations of adularia, a high Ag/Au ratio, and strong textural evidence, including crustiform banding, cavity-filling veins, banded quartz-chalcedony veins, druse-lined cavities, lattice-textured bladed calcite replaced by quartz, and botryoidal silica. Minor occurrences of intermediate-sulfidation epithermal veins and PCD-style veins were observed along the major fault, including a BMQ vein. At Ronaldo, high silica content and sericitic alteration correlate well with elevated concentrations of Ag, Au, and Mo, whereas Cu concentrations do not correlate well with any alteration type or with silica content.

This study concludes that the mineralization and alteration at the Ronaldo prospect has been formed through the following sequence of events: 1) Formation of a porphyry-stock-related high-temperature, advanced argillic lithocap and magmatic-hydrothermal breccia emplacement (Figure 49 (early)), 2) waning of the hydrothermal system resulting in widespread intermediate argillic alteration overprinting in mostly intrusive units, whereas sericitic alteration overprinted the root zone of the lithocap (now visible as

silicified ridges) and the potassic altered magmatic-hydrothermal breccia (Figure 49 (intermediate)), 3) further cooling of the hydrothermal system causing deposition of intermediate-sulfidation epithermal mineralization alongside the lithocap (Figure 49 (late)), 4) laterally flowing meteoric water unrelated to the magmatic-hydrothermal system depositing low-sulfidation epithermal mineralization in the silicified ridges, and 5) continuous erosion causing the silicified ridges, both intrusive bodies, and magmatic-hydrothermal breccia to be exposed at the surface.

It is unlikely that a PCD at economical depth exists at Ronaldo although root zones of advanced argillic lithocaps have been shown to overprint the upper parts of PCDs. The prospect does show potential for further low-sulfidation epithermal mineralization exploration.

7. ACKNOWLEDGEMENTS

I am grateful to Dr Petri Peltonen, my thesis supervisor, for guiding and assisting me in this project. My sincerest gratitude goes out to Dr Federico Cernuschi, without whose excellent guidance and advice this project would not have been possible to complete. Working on this project was a great learning experience and far less arduous due to his patience and perseverance. Teaching the Anaconda mapping method before field work on the project commenced was also a much appreciated contribution provided by Dr Cernuschi. Many thanks to Miguel Ponce for teaching me to map epithermal and porphyry deposit features, without which completion of this project would also have been impossible. I am grateful to the heads of the FQM Lima office, Markku Lappalainen, Sebastian Benavides, and Raymond Rivera for initiating this master's thesis project and for entrusting this work to me. I also want to express my gratitude to everyone who shared their knowledge and their critical comments to help improve this manuscript. The team of geologists and technicians lead by Saúl Galvez and Saturnino Vera at the Huajintay and Cajamarca exploration camps were of great help, attending to our every need and request. Finally, I am grateful to First Quantum Minerals Ltd. for funding this

research and for the excellent guidance that the entire FQM team provided me with during fieldwork and afterwards.

8. REFERENCES

Arribas, A., Hedenquist, J. W., Itaya, T., Okada, T., Concepcion, R. A., and Garcia, J. S. 1995. 'Contemporaneous Formation of Adjacent Porphyry and Epithermal Cu-Au Deposits over 300 Ka in Northern Luzon, Philippines', *Geology*, 23: 337-40.

Awadh, S. M. 2009. 'Iron content variations in sphalerite and their effects on reflectance and internal reflections under reflected light', *Arabian Journal of Geosciences*, 2: 139-42.

Barton, P. B., and Bethke, P. M. 1987. 'Chalcopyrite disease in sphalerite: pathology and epidemiology', *American Mineralogist*, 72: 451-67.

Cooke, D. R., Deyell, C. L., Waters, P. J., Gonzales, R. I., and Zaw, K. 2011. 'Evidence for Magmatic-Hydrothermal Fluids and Ore-Forming Processes in Epithermal and Porphyry Deposits of the Baguio District, Philippines', *Economic Geology*, 106: 1399-424.

Cooke, D. R., Hollings, P., and Walsh, J. L. 2005. 'Giant porphyry deposits: Characteristics, distribution, and tectonic controls', *Economic Geology*, 100: 801-18.

Cooke, D. R., White, N. C., Zhang, L., Chang, Z., and Chen, H. 2017. "Lithocaps–characteristics, origins and significance for porphyry and epithermal exploration." In *14th SGA Biennial Meeting*, 291-94.

Dong, G., Morrison, G., and Jaireth, S. 1995. 'Quartz textures in epithermal veins, Queensland - Classification, origin, and implication', *Economic Geology and the Bulletin of the Society of Economic Geologists*, 90: 1841-56.

Einaudi, M. T. 1997. 'Mapping altered and mineralized rocks; an introduction to the "Anaconda method"', *Unpublished report. Stanford, CA: Stanford University Department of Geological Environmental Sciences*.

Einaudi, M. T., Hedenquist, J. W., and Inan, E. E. 2003. 'Sulfidation state of fluids in active and extinct hydrothermal systems: Transitions from porphyry to epithermal environments', *Society of Economic Geologists, Special Publication*, 10: 285-314.

Floyd, P. A., and Winchester, J. A. 1978. 'Identification and discrimination of altered and metamorphosed volcanic rocks using immobile elements', *Chemical Geology*, 21: 291-306.

Franchini, M., Impiccini, A., Lentz, D., Rios, F. J., O'Leary, S., Pons, J., and Schalamuk, A. I. 2011. 'Porphyry to epithermal transition in the Agua Rica polymetallic deposit, Catamarca, Argentina: An integrated petrologic analysis of ore and alteration parageneses', *Ore Geology Reviews*, 41: 49-74.

Giggenbach, W. F. 1997. 'The origin and evolution of fluids in magmatic-hydrothermal systems', *Geochemistry of hydrothermal ore deposits*.

Goetz, A. F. H. 2009. 'Three decades of hyperspectral remote sensing of the Earth: A personal view', *Remote Sensing of Environment*, 113: S5-S16.

Gustafson, L. B., and Hunt, J. P. 1975. 'The porphyry copper deposit at El Salvador, Chile', *Economic Geology*, 70: 857-912.

Gutscher, M. A., Olivet, J. L., Aslanian, D., Eissen, J. P., and Maury, R. 1999. 'The "lost Inca Plateau": Cause of flat subduction beneath Peru?', *Earth and Planetary Science Letters*, 171: 335-41.

Halley, S., Dilles, J. H., and Tosdal, R. M. 2015. 'Footprints: hydrothermal alteration and geochemical dispersion around porphyry copper deposits', *Society of Economic Geologists Newsletter*, 100: 12-17.

Hedenquist, J. W., Arribas, A., and Gonzalez-Urien, E. 2000. 'Exploration for epithermal gold deposits', *Reviews in Economic Geology*, 13: 45-77.

Hedenquist, J. W., Arribas, A., and Reynolds, T. J. 1998. 'Evolution of an intrusion-centered hydrothermal system: Far Southeast-Lepanto porphyry and epithermal Cu-Au deposits, Philippines', *Economic Geology and the Bulletin of the Society of Economic Geologists*, 93: 373-404.

Heinrich, C. 2005. 'The physical and chemical evolution of low-salinity magmatic fluids at the porphyry to epithermal transition: a thermodynamic study', *Mineralium Deposita*, 39: 864-89.

Henley, R. W., and McNabb, A. 1978. 'Magmatic vapor plumes and ground-water interaction in porphyry copper emplacement', *Economic Geology and the Bulletin of the Society of Economic Geologists*, 73: 1-20.

Henley, R. W., Truesdell, A. H., Barton, P. B., and Whitney, J. A. 1985. *Fluid-mineral equilibria in hydrothermal systems* (Society of Economic Geologists).

Holliday, J. R., and Cooke, D. R. 2007. "Advances in geological models and exploration methods for copper±gold porphyry deposits." In *Proceedings of exploration*, 791-809. Citeseer.

Instituto Geológico Minero y Metalúrgico. 2003. 'Memoria descriptiva de la revisión y actualización del cuadrángulo de Tantará (27-l). Escala 1:50 000', Accessed 2019 Aug 26. https://repositorio.ingemmet.gob.pe/handle/ingemmet/2127.

Jackson, S. E., Pearson, N. J., Griffin, W. L., and Belousova, E. A. 2004. 'The application of laser ablation-inductively coupled plasma-mass spectrometry to in situ U-Pb zircon geochronology', *Chemical Geology*, 211: 47-69.

Marocco, R. 1978. *Un segment EW de la chaîne des Andes péruviennes: la déflexion d'Abancay; Étude géologique de la Cordillère orientale et des hauts plateaux entre Cuzco et San Miguel, sud du Pérou (12030'S à 14000S)* (IRD Editions).

Muntean, J. L., and Einaudi, M. T. 2001. 'Porphyry-epithermal transition: Maricunga belt, northern Chile', *Economic Geology and the Bulletin of the Society of Economic Geologists*, 96: 743-72.

Ossandón, C. G., Fréraut, C. R., Gustafson, L. B., Lindsay, D. D, and Zentilli, M. 2001. 'Geology of the Chuquicamata mine: A progress report', *Economic Geology and the Bulletin of the Society of Economic Geologists*, 96: 249-70.

Peruvian Metals Corp. 2018. 'Panteria', Accessed 2019 Aug 26. https://www.peruvianmetals.com/panteria/.

Proffett, J. M. 2009. 'High Cu grades in porphyry Cu deposits and their relationship to emplacement depth of magmatic sources', *Geology*, 37: 675-78.

Reed, M., and Spycher, N. 1984. 'Calculation of Ph and Mineral Equilibria in Hydrothermal Waters with Application to Geothermometry and Studies of Boiling and Dilution', *Geochimica Et Cosmochimica Acta*, 48: 1479-92.

Salazar Díaz, H., and Landa Tovar, C. 1983. 'Geología de los cuadrángulos de Mala, Lunahuaná, Tupe, Conayca, Chincha, Tantará y Castrovirreyna 26-j, 26-k, 26-l, 26-m, 27-k, 27-l, 27-m-[Boletín A 44]', *INGEMMET. Boletín, Serie A: Carta Geológica Nacional, n° 44*.

Seedorf, E. 2005. 'Porphyry deposits: Characteristics and origin of hypogene features', *Econ. Geol. 100th Anniv. Volume*, 100: 251-98.

Sillitoe, R. H. 1972. 'A plate tectonic model for the origin of porphyry copper deposits', *Economic Geology*, 67: 184-97.

———. 2000. "Styles of high-sulphidation gold, silver and copper mineralisation in porphyry and epithermal environments." In *Proceedings of the Australasian Institute of Mining and Metallurgy*, 19-34. Parkville, Vic.: The Institute,[1990]-c2001.

———. 2005. 'Andean copper province: Tectonomagmatic settings, deposit types, metallogeny, exploration, and discovery', *Econ. Geol. 100th Anniv. Volume*: 845-90.

———. 2010. 'Porphyry Copper Systems', *Economic Geology*, 105: 3-41.

Sillitoe, R. H., and Hedenquist, J. W. 2003. 'Linkages between volcanotectonic settings, ore-fluid compositions, and epithermal precious metal deposits', *Society of Economic Geologists, Special Publication*, 10: 315-43.

Simmons, S. F., and Christenson, B. W. 1994. 'Origins of Calcite in a Boiling Geothermal System', *American Journal of Science*, 294: 361-400.

Simmons, S. F., White, N. C., and John, D. A. 2005. 'Geological characteristics of epithermal precious and base metal deposits', *Economic Geology*, 100: 485-522.

Sláma, J., Košler, J., Condon, D. J., Crowley, J. L., Gerdes, A., Hanchar, J. M., Horstwood, M. S. A., Morris, G. A., Nasdala, L., and Norberg, N. 2008. 'Plešovice zircon—a new natural reference material for U–Pb and Hf isotopic microanalysis', *Chemical Geology*, 249: 1-35.

Stern, C. R. 2004. 'Active Andean volcanism: its geologic and tectonic setting', *Revista geológica de Chile*, 31: 161-206.

Tassara, A. 2005. 'Interaction between the Nazca and South American plates and formation of the Altiplano-Puna plateau: Review of a flexural analysis along the Andean margin (15 degrees-34 degrees S)', *Tectonophysics*, 399: 39-57.

Tebbens, S. F., and Cande, S. C. 1997. 'Southeast Pacific tectonic evolution from early Oligocene to present', *Journal of Geophysical Research-Solid Earth*, 102: 12061-84.

Thompson, A. J. B. 1999. 'Alteration mapping in exploration: Application of short wave infrared (SWIR) spectroscopy', *Economic Geology Newsletter*, 30: 13.

White, N. C., and Hedenquist, J. W. 1995. 'Epithermal gold deposits: styles, characteristics and exploration', *SEG Newsletter*, 23: 9-13.

9. APPENDICES

Detailed description of whole-rock geochemical methods

During the mapping campaign, rock samples were collected from outcrops for detailed study of the different lithological units and their relationships, in addition to samples collected for SWIR analysis of the hydrothermal alteration mineralogy.

A total of 47 samples were analysed for whole-rock geochemistry in addition to tests for precious and base metals. ALS Geochemistry was chosen to perform the whole-rock geochemical analysis. Rock samples were processed by ALS Peru S.A. in Lima, Peru, using their PREP-31 package. Next, a near-total four-acid digestion (ALS Geochemistry method ME-MS61r) and a complete characterization package (ALS Geochemistry package CCP-PKG01) were used to analyse the samples. The CCP-PKG01 package included the following ALS Geochemistry methods: ME-ICP06, ME-IR08, ME-MS81, ME-MS42, and ME-4ACD81. Some of these methods are not included in the final results and will therefore not be described further.

The ALS Geochemistry method ME-MS61r was used to analyse the samples for 48 trace elements and 12 rare earth elements using four-acid digestion followed by ICP-MS. The dissolution liberates nearly 100% of all elements, except for Hf, Zr, minor heavy rare earth elements, and Y trapped in refractory zircon (Halley et al. 2015). Assay values an order of magnitude greater or higher, than average crustal abundances should be considered anomalous (Halley et al. 2015).

The whole-rock geochemistry samples were analysed for major and minor element oxides by means of lithium metaborate fusion and acid digestion, followed by ICP-AES (ME-ICP06).

The ALS Geochemistry method ME-MS42 was used to obtain analytical results for Hg. The method consists of aqua regia digestion followed by ICP-MS.

Base metals were analysed using four-acid digestion followed by ICP-AES (ME-4ACD81). A sample whose values exceeded the detection limit of 10,000 ppm for both Pb and Zn

was treated to a four-acid digestion followed by ICP-AES (Pb-OG62 and Zn-OG62 respectively).

Gold was analysed by fire assay up to a 10 ppm detection limit and, in one case, by gravimetric finish (ALS Geochemistry methods Au-AA23 and Au-GRA21 respectively).

Silver was analysed by means of four-acid digestion followed by ICP-AES (ME-4ACD81) up to a detection limit of 100 ppm. Samples that contained >100 ppm of Ag were subjected to the Ag-OG62 method. One sample exceeded the 1500 ppm detection limit of the Ag-OG62 method and was treated to a fire assay and gravimetric finish (Ag-GRA21).

Anaconda-style maps

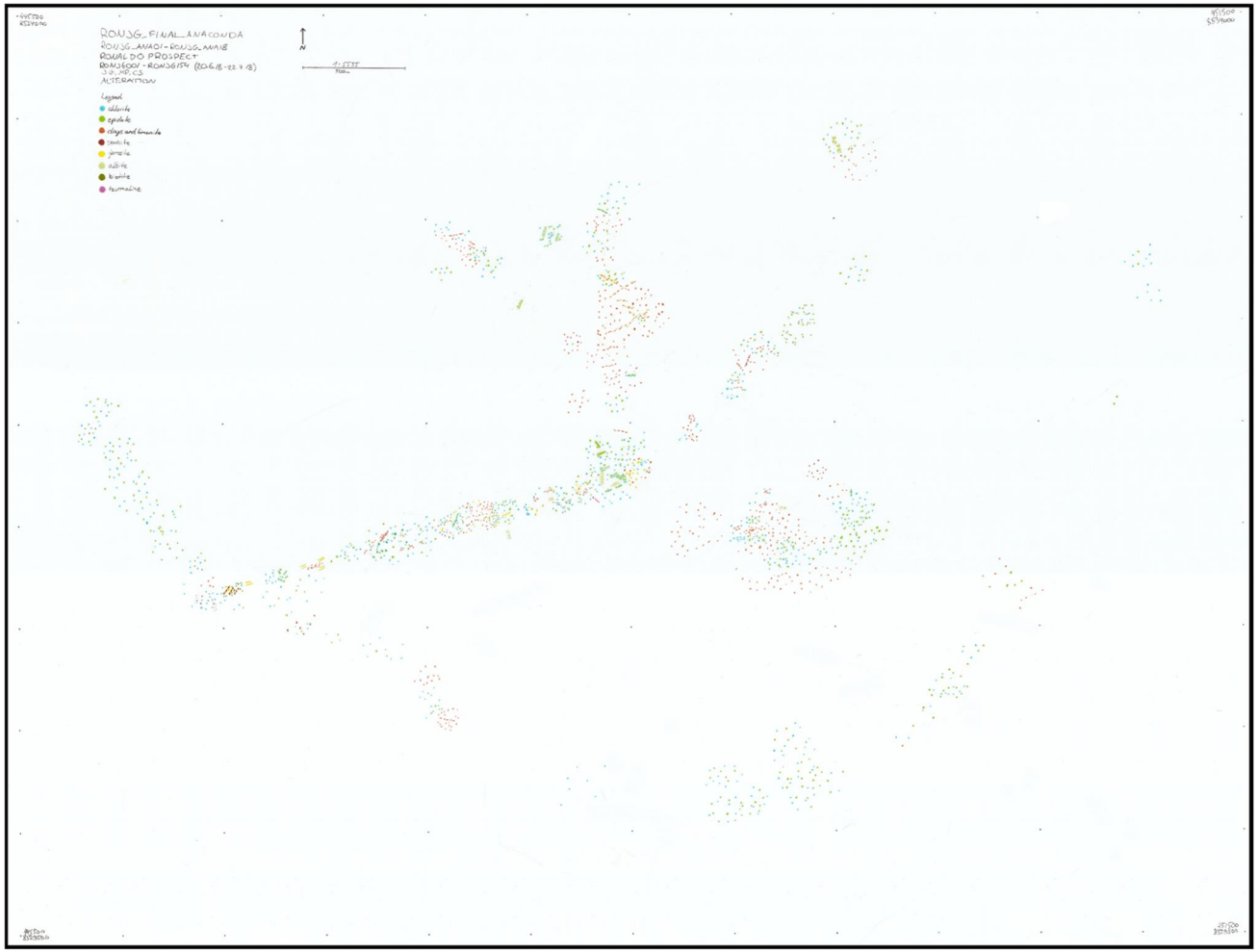

Figure 50: Scanned image of the Anaconda-style map of the alteration layer.

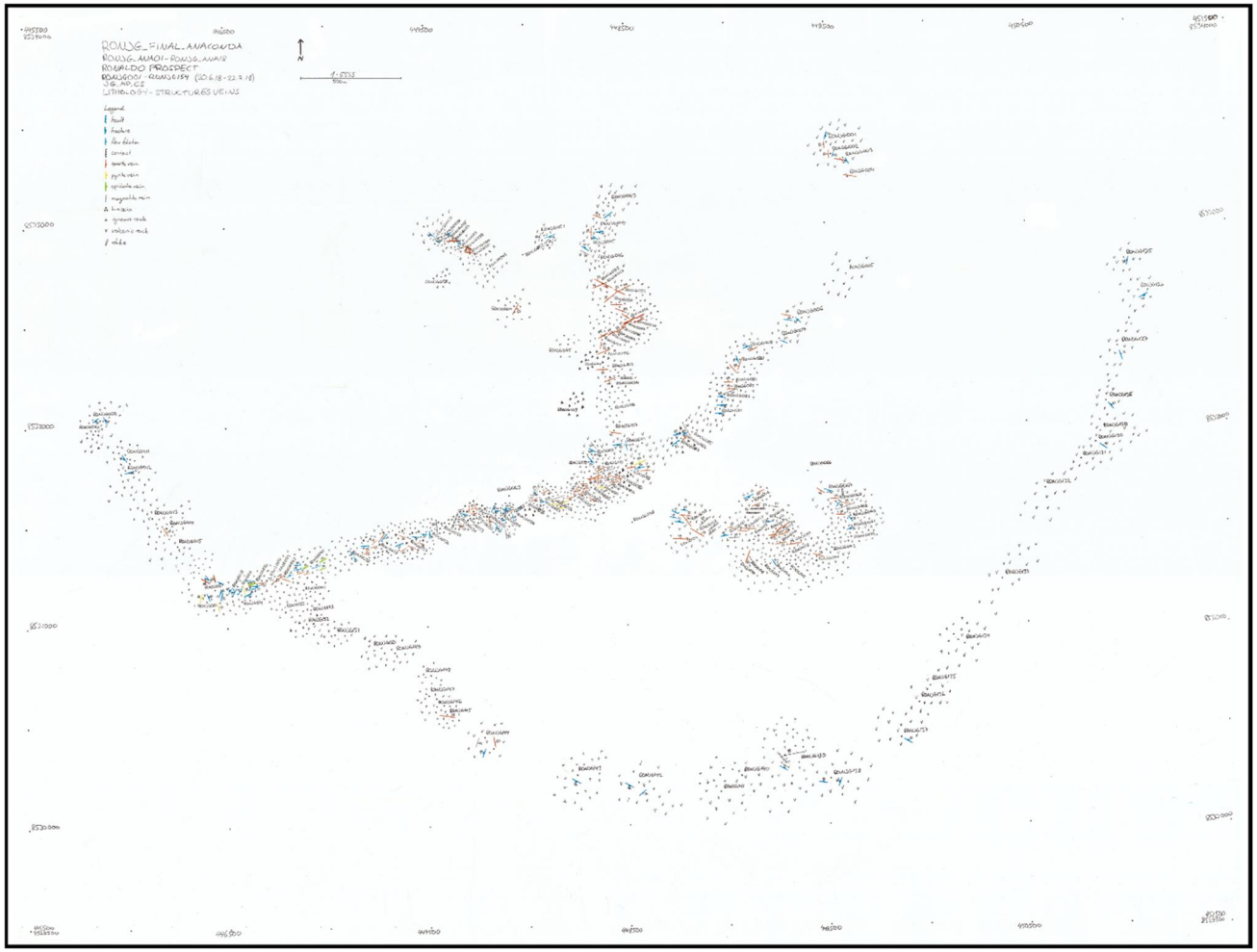

Figure 51: Scanned image of the Anaconda-style map of the lithology, structures and veins layer.

Figure 52: Scanned image of the Anaconda-style map of the mineralization layer.